Resonant-state expansion for periodic open optical systems

Sam Thomas Neale

July 23, 2021

Thesis submitted to Cardiff University for the degree of Doctor of Philosophy

Abstract

The resonant-state expansion is a perturbation theory that allows the accurate calculation of the resonant states of a photonic system by using a complete set of resonant states of a basis system. This thesis pioneers a new research direction of existing rigorous perturbative theory to any periodic photonic system described by Maxwell's wave equations. This method provides new and unique tools for describing the interaction of light in periodic systems which are not available through other methods.

The resonant states are found in frequency space for planar periodic systems which presents a major complication to the resonant-state expansion due to the branch cuts that are present in the frequency plane due to the dispersion relation between the frequency and the wavevector of the modes. We solve this by discretising the cuts into a series of artificial resonant states that lie along the cuts. These are then treated on equal footing with regular resonant states.

Additionally, the resonant-state expansion method allows for a deeper understanding of the formation of the photonic crystal resonant states as it treats these modes as a superposition of all modes of the basis system. Specifically, we look at the bound states in the continuum, unusual modes which remain localised to the system despite existing in a strongly coupled system which contains leaky modes. The resonant-state expansion allows us to formulate mathematical conditions for these modes to form, as well as being able to distinguish between different classes of these modes.

Acknowledgements

I would firstly like to thank my supervisor, Dr. Egor Muljarov for his years of guidance, teaching and patience. Dr. Muljarov has always been willing to discuss problems and has always made sure that he is readily contactable. The notes that Dr. Muljarov provided helped me to understand the topics at hand rather than spending many hours researching literature.

I am thankful for the EPSRC for funding this PhD.

Publications

S. Neale and E. A. Muljarov, *"Photonic crystal structures treated by the resonant state expansion"*, International Conference on Metamaterials, Photonic Crystals and Plasmonics (META) 2019 Lisbon, Portugal (2019), pg.112
https://metaconferences.org/ocs/files/META19_program.pdf

S. Neale and E. A. Muljarov, *"Photonic crystal structures treated by the resonant state expansion"*, Photonic & Electromagnetics Research Symposium (PIERS) 2019 in Rome, Italy (2019), pg. 128
http://piers.org/piers2019Rome/files/FinalProgram.pdf

S. Neale and E. A. Muljarov, *"Resonant-state expansion for planar photonic crystal structures"*, Phys. Rev. B **101**, 155128 (2020)

S. Neale and E. A Muljarov, *"Accidental and symmetry-protected bound states in the continuum in a photonic-crystal slab: A resonant-state expansion study"*, Phys. Rev. B **103** 155112 (2021)

Presentations

S. Neale and E. A. Muljarov *"Resonant states in a photonic crystal slab"* Theory Seminar, Cardiff University (2017)

S. Neale and E. A. Muljarov *"Scattering matrix method for calculating resonant states in photonic crystal structures"* Theory Seminar, Cardiff University (2019)

S. Neale and E. A. Muljarov *"Photonic Crystal Structures Treated by the Resonant State Expansion"* (presented by E. A. Muljarov), Photonic & Electromagnetics Research Symposium (PIERS) 2019 in Rome, Italy (19/06/2019)

S. Neale and E. A. Muljarov *"Resonant state expansion applied to photonic-crystal structures"*, Theory Seminar, Cardiff University (2019)

S. Neale and E. A. Muljarov *"Photonic Crystal Structures Treated by the Resonant State Expansion"* (presented by E. A. Muljarov), International Conference on Metamaterials, Photonic Crystals and Plasmonics (META) 2019 in Lisbon, Portugal (24/07/2019)

S. Neale and E. A. Muljarov *"Accidental and symmetry-protected bound states in the continuum in planar photonic-crystal structures, studied by the resonant-state expansion"* Photon 2020 Virtual Conference (02/09/2020)

Contents

Chapter 1

Introduction

Photonic crystal structures exhibit a number of fundamental optical properties, such as strong confinement and Bragg scattering of light, which can be used, e.g., for light propagation control in grating couplers [1], photonic integrated circuits [2, 3] and beam splitters [4]. The band structure of an idealised photonic crystal (PC), infinitely extended in all directions, is already very complicated [5]. Planar PC systems provide an opportunity for the light trapped within an optical waveguide (WG) to couple to the photonic continuum outside the system [6–9], which makes finding the light eigenmodes of a PC slab an even more challenging task.

The resonant-state expansion (RSE) method allows the calculation of the eigenmodes of photonic systems - also known as resonant states (RSs) - from a set of (preferably analytically known) solutions of another, similar system by treating the system of interest as a perturbation. As of writing this thesis, the RSE has been applied to finite open optical systems of different geometry and dimensionality [10–13], as well as to homogeneous [14, 15] and inhomogeneous planar waveguides [16]. This thesis presents for the first time that an application

of the RSE to a photonic crystal uses a homogeneous slab as a basis which contains up to several thousand modes and crucially, includes of all branch cuts in the complex frequency plane.

Current well-known computational methods include the finite-difference in time-domain, finite-element and Fourier modal method. In this thesis, it is necessary to compare the results of the RSE to one of these known methods to prove its effectiveness and ultimately, its superiority. We will use the scattering matrix method (SMM) [6, 7], also known in the literature as the Fourier modal method [17–20]. One of the main advantages of the RSE over these methods is the guarantee of the completeness of the set of RSs of the target system given a complete set of basis modes.

Other advantages include: the simplicity of the method - requiring only a single diagonalisation of a matrix, the computation time which is orders of magnitude faster than other methods [12], the flexibility of the method - the RSE is able to accurately describe large perturbations and the added insight into the formation of the RSs of complex systems by describing them as a perturbed set of RSs of a simple system.

1.1 Resonant states

Resonant states (RSs) are discrete solutions to Maxwell's wave equation (MWE) with outgoing boundary conditions [21]. RSs were first used by Gamow in 1928 [22] to describe the tunnelling of an alpha particle out of an atomic nucleus during radioactive decay and later by Siegert [23]. The concept of RSs (also known as "quasi-normal modes") is widely used in the literature as a natural tool for understanding the optical properties of micro- and nano-resonators, see e.g. a recent review [24]. These states have, in general, complex frequencies with a negative (or zero) imaginary part. This means that the associated electric field

for these modes have exponentially growing amplitudes as the field leaves the system which, at first, may seem unintuitive or unphysical but this is merely a consequence of the decaying nature of these fields, meaning that portions of the field that left the system at an earlier time will naturally have a larger amplitude than later portions. This is a characteristic property of the RSs, which can cause leakage of energy out of the system over time with the lifetimes of the modes given by the inverse of their imaginary part. Physically, the RSs describe the culmination of all the constructive and destructive interferences of the fields within the system due to the multiple reflections at the surfaces.

1.1.1 A simple illustration: RSs of a homogeneous slab

Consider a slab of dielectric material which is infinite in two dimensions and finite in the third. The slab has constant permittivity and permeability and is suspended in a vacuum. This is the homogeneous dielectric slab which is an important system for this work as it's RSs are used as a basis. This system supports resonant states which can be excited by an incident electric field. The simplest case of the RSs in this system is when the electric field is normal to the surface of the slab in which case the RSs eigenfrequencies will all be complex with the same imaginary part and evenly spaced along the real direction in the complex plane. These modes can be found analytically due to their simplicity. The solutions are split into an odd and even case (note that this is true even for non-normal incidence), for a given parity the mth mode is given by:

$$\frac{-i}{a\sqrt{\mu\varepsilon}}\left(\arctan(\sqrt{\mu\varepsilon}) + im\pi\right) \quad \text{for odd modes} \tag{1.1}$$

$$\frac{-i}{a\sqrt{\mu\varepsilon}}\left(\arctan(\frac{1}{\sqrt{\mu\varepsilon}}) + im\pi\right) \quad \text{for even modes.} \tag{1.2}$$

While the parity of the mode is important and will appear in several equations later, the odd and even modes are shown in the spectrum together with no distinction between them.

Every RS's eigenfrequency has an imaginary part and therefore they all radiate into the far-field i.e they all have travelling solutions outside of the system. This describes these modes as leaky as they radiate energy away from the system over time, this type of mode is also known as Fabry-Perot (FP) modes. The imaginary part of the frequencies of the modes are all negative which indicates that the associated electric fields decay over time which reinforces the picture of RSs described earlier in which portions of the field that left the system at an earlier time have more energy than later portions.

If we now change the incident electric field so that it is encountering the surface of the slab at an angle, different RSs are excited. The incoming electric field wavevector is described by it's z- and x-direction components (perpendicular to and parallel to the slab respectively). The x-direction wavevector is labelled p and is such that $p = 0$ corresponds to normal incidence. The RSs for $p \neq 0$ are no longer evenly distributed in the real direction and no longer have identical imaginary parts. As the angle of incidence futher deviates from normal, the frequencies of the RSs "bend" toward the real axis until there are several modes lying on the real axis itself. These modes, which have zero imaginary part, do not radiate to the far-field and thus do not leak energy out of the system over time and have only exponentially decaying fields outside of the system. These are known as WG modes which cause confinement of energy to the system. It should be noted that these modes are not directly excited by the incident field since they would require an imaginary z-direction wavevector.

Figure 1.1 shows the spectrum of RSs in this case which consists of the real frequencies of the WG modes and the complex frequencies of the FP modes. As

can be seen, the frequency Re(ω)= ± 5 (in this particular case, since the in-plane wavevector is set to 5 which will be discussed further) separates the FP modes from the WG modes. This defines the terms open and closed: the system is said to open at frequencies where FP modes exist and closed at frequencies where only WG modes exist.

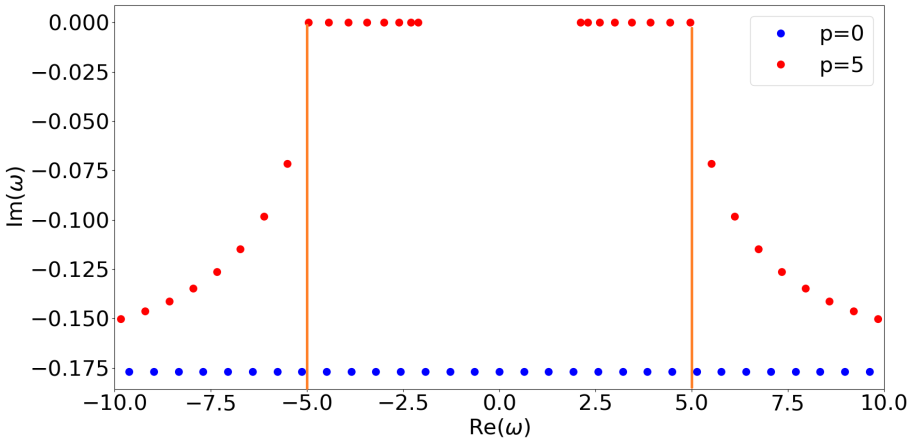

Figure 1.1: Eigenfrequencies of the resonant states of a homogeneous dielectric slab corresponding to normal ($p = 0$) and non-normal incidence ($p = 5$), the orange lines highlight the cuts for the $p = 5$ case. The slab has half-width a and permittivity of $\varepsilon = 6$.

The WG modes are created through total internal reflection and physically cannot be excited from fields outside of the slab as that would violate time-reversal symmetry since energy would enter the system but never be able to leave, creating a one-way interaction.

The positions and linewidths of resonances in optical systems can be modified by, for example modifying the permittivity. This makes RSs of particular importance for sensing applications, ranging from sensing the refractive index and chirality of a medium [25–27] to biosensing of individual molecules and

atoms [28–30]. RSs have found their application also in miniature lasers [31] and low-loss guiding of light in photonic crystal fibers [2], to name a few.

1.1.2 Branch cuts

The separation of the WG modes from the FP modes also has a more significant meaning. In optical systems there exists a dispersion relation between the frequency of the light and it's wavevector. The frequencies and wavevectors of the RSs are generally complex which can lead to branch cuts since the dispersion relation contains a square root:

$$k = \sqrt{\omega^2 - p^2} \tag{1.3}$$

(for more details see Ch. 2). This branch cut is the line that separates WG modes from FP modes although in general there is a large degree of freedom in choosing the path that the cut takes, it is specifically chosen to point vertically downward from the branch points ($\mathrm{Re}(\omega) = \pm 5$ in the example above) to infinity.

These branch cuts present a major challenge for the RSE, which takes advantage of residue theorem which requires Green's function to be holomorphic everywhere except for a finite number of poles. Residue theorem asserts that a contour integral in the complex plane can be evaluated by the summation of the residues of all poles lying within the contour. The discontinuity introduced by the cuts forces the contour to distort and introduces to the sum of residues additional integrals taken along the cuts. These cuts are therefore present in the basis alongside the spectrum of RSs. In order to treat these cuts, they are discretised into a series of artificial cut modes which are placed along the cut and added to the basis [11, 16]. This was done for a photonic crystal perturbation in the frequency plane for the first time in this work [32]. Properly weighted, these modes asymptotically converge to the same result as the integrals as the

number of cut modes reaches infinity and can be treated as though they are regular RSs. Physically, the effect of these modes are present in the photonic crystal transmission spectrum as Rayliegh-Wood anomalies corresponding to the opening of new diffraction channels into free space [33, 34].

In addition to creating a discontinuity which affects the contour integral used in residue theorem, the presence of cuts also creates another problem. The cuts split the complex plane into the two Riemann sheets with the RSs distributed across both sheets. This creates a choice for which sheet should be used as the basis for the RSE. Clearly, the sheet that contains the RSs which produce results that agree with the observable parameters (namely the transmission spectrum) should be used. It should be noted that the modes on the other sheet, although unphysical, can also be used as a basis. This will obviously produce a different set of perturbed modes but the accuracy of the method remains the same. It is however, more natural to use the physical sheet. The modes on the other sheet are then labelled anti-WG and anti-FP modes to distinguish them from WG and FP modes. Anti-FP modes are completely unphysical since their frequencies are complex with a positive imaginary part which would lead to an exponentially increasing temporal part of the electric field suggesting that the system gains energy over time as it leaks energy into the surrounding environment. The spectrum of modes from both sheets are shown together in frequency space in Fig. 1.2.

As mentioned, to determine which sheet is the physical sheet we use the observable transmission spectrum. The transmission spectrum directly correlates to Green's function in an optical system which is central to the derivation of the RSE (derivation in Ch. 2) and is therefore what we use in Appendix C where we show that the Mittag-Leffler form of the GF matches the analytic.

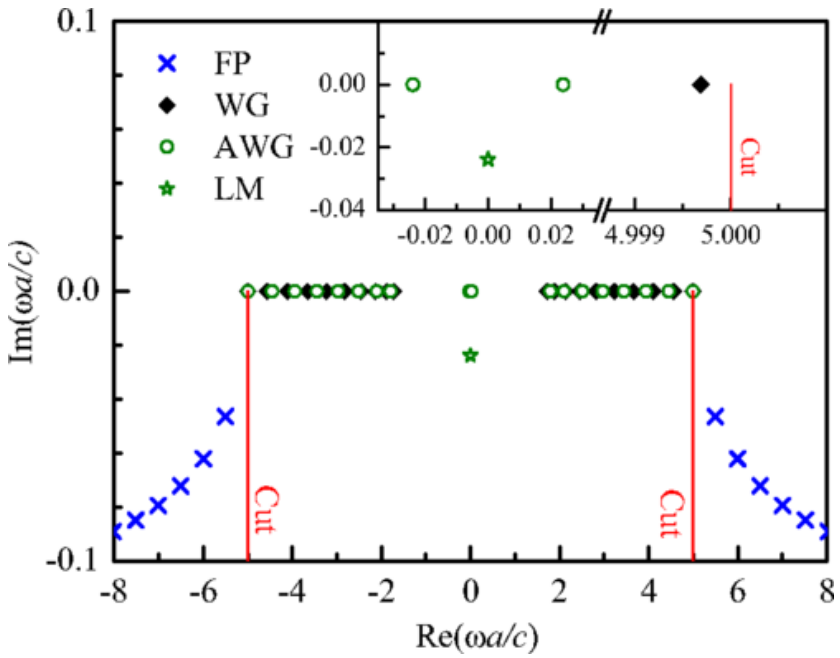

Figure 1.2: Figure from [14] showing the resonant states for a homogeneous dielectric slab in frequency space. Shown are the different classes of RSs: Fabry-Perot mode (blue cross), waveguide mode (black diamond), anti-waveguide mode (green circle) and leaky modes (green star). Green indicates modes which are on the non-physical Riemann sheet. The insert shows the cut which seperates waveguide modes from Fabry-Perot modes.

1.2 Bound states in the continuum

In a photonic crystal, there is a mixing of all possible Bragg harmonics causing coupling between all modes including guided modes coupling to leaky modes allowing them to communicate to the radiation continuum outside the system [6]. Intuitively, this would lead to the conclusion that guided modes are not possible in a photonic crystal since all modes have some pathway to the outside but in reality, modes can remain localised within the system despite their frequencies lying in the continuum. These are known in the literature as bound states in the continuum (BICs), first proposed by von Neumann and Wigner [35] in quantum systems but recently have been observed in optics [36]. The BICs are theoretically not seen in the transmission spectrum since they are entirely real and are therefore only present in the spectrum as infinitely thin delta functions. In practice, we can only satisify the conditions for quasi-BICs - very high Q-factor modes - which can be seen in the spectrum as sharp lines which is useful in applications such as lasers [37,38], sensing [39] and filtering [40]. These peculiar modes have gained a lot of interest in recent years [41–50].

Fundamentally, BICs are formed when a mode is somehow forbidden from communicating with leaky modes which would otherwise allow them to leak energy through their coupling. There are two types of BICs with different formation mechanisms: accidental BICs (A-BICs) and symmetry-protected BICs (S-BICs). S-BICs are formed in systems with one or more symmetries which creates a spectrum of RSs of different parities. Coupling between these different parity modes can be forbidden and if a guided mode is forbidden to couple to leaky modes then it will remain guided and not communicate with the continuum outside the system. S-BICs are robust in that they only require the system to be symmetric and their bound nature is not dependant on other system parameters. Of course in practice, either type of BIC is difficult to realise

since they require ideal conditions (perfectly normal incidence would be hard to produce, for example.)

A-BICs are formed not by a forbidding of communication between modes but instead via an accidental cancellation of outgoing fields at the edges of the system caused by the destructive interference of many scattered waves. A-BICs are very sensitive to material parameters and require careful tuning to be expressed as opposed to the S-BICs, which exist for a large range of material parameters (as long as normal incidence is maintained).

Despite the differences in formation both BICs interact with light in the same way as WG modes: they do not allow the energy they contain to leave the system. These two types of BICs are not easily distinguished from one another in the literature, usually being separated by simply breaking the symmetry of the system thereby destroying any S-BICs. In this work however, we have used the resonant-state expansion to provide mathematical definitions for both cases of BICs.

1.3 Resonant-state expansion

The resonant-state expansion (RSE) is a novel rigorous approach developed in electrodynamics [13] for calculating the RSs of an optical system. Using a complete set of the RSs of a simpler system as a basis, the RSE performs a mapping of Maxwell's wave equation onto a linear eigenvalues problem, which determines the RSs of the complex system of interest. In addition to a higher numerical efficiency compared to other computational methods, such as finite-difference in time-domain, finite-element, and Fourier modal method, as demonstrated in [12, 16], the RSE provides an intuitive physical picture of resonant phenomena, capable of explaining features observed in optical spectra. Also, unlike other approaches, the RSE guarantees the completeness of the set of the RSs

found within the selected spectral range, provided that the basis set used as input for the RSE is also complete. The latter is easy to achieve and to verify when choosing the basis system to be analytically solvable. Other approaches, in turn, are not able to guarantee that all relevant modes are found and that there are no spurious solutions. The effect of other modes, not included in the optical spectrum, is commonly treated as a background contribution adjusted with a number of fit parameters [51, 52].

The RSE not only allows for the calculation of RSs in complex systems but also gives some insight into the formation of such modes. The RSE can easily show how each of the basis modes contributes to each perturbed mode, which can explain some of the behaviour of the modes like for example, why some WG modes become leaky and others can remain localised as BICs. Additionally, the RSE is a computationally lightweight method allowing for it to be run, in some cases, thousands of times in the time it takes for other methods to run once. This allows us to trace out mode positions as system parameters are changed, while technically possible to do with any method, the RSE allows for this to be done in a reasonable time frame.

The RSE treats the modes of complex systems as having a contribution from all modes of the basis system. We can also calculate the electric field for perturbed modes in much the same way as the modes themselves: as a weighted summation over all the basis electric fields. The electric fields of photonic crystal modes can be quite complex due to the mixing of all modes. With the RSE, we have access to the weights of the basis fields which allows us to break down these complicated fields into a series of simple, analytical and easier to understand fields.

The RSE is an asymptotically exact method where the error decreases as the size of the basis increases; including more modes in the basis increases the

accuracy of the perturbation. The basis is defined by a circle in the frequency plane within which all basis modes and cuts are taken into account. As mentioned before the influence of each basis mode behaves like a Lorentzian so the addition of far away basis modes has a diminishing effect with the perturbed modes at the centre of the basis having the lowest error and modes at the edge of the basis being very poorly perturbed.

1.4 Established Methods

There are several established methods used to simulate photonic crystals which will be briefly described here for comparison to the RSE. The methods to be described in more detail are the finite difference in the time domain (FDTD) method and the guided mode expansion (GME). The scattering matrix method is also a popular choice, but this is described in detail in Appendix F.

1.4.1 Finite Difference in Time Domain

The FDTD method was first described by Yee in 1966 [53]. It functions rather differently to the RSE method but is nevertheless a popular choice to describe light in photonic crystals.

In the FDTD method, Maxwell's equations are solved iteratively through finite steps in space and time. A grid is defined over the system with the grid spacing given by $(\Delta x, \Delta y, \Delta z)$ and temporal spacing of Δt. Maxwell's equations describe the magnetic ($\mathbf{H}$) and electric ($\mathbf{E}$) fields in terms of derivatives of one another:

$$\begin{aligned} \frac{\partial(\mu\mathbf{H})}{\partial t} + \nabla \times \mathbf{E} &= 0 \\ \frac{\partial(\varepsilon\mathbf{E})}{\partial t} - \nabla \times \mathbf{H} &= \mathbf{j} \end{aligned} \tag{1.4}$$

where $\mathbf{j}$ is the source current.

It is therefore possible to solve for the electric field using the magnetic field and using that result to calculate the magnetic field in the next instant and so on until the fields are described in the full spatial and temporal extent.

The derivatives are solved using the finite difference method:

$$\frac{df}{dx} \approx \frac{f(x + \Delta x) - f(x)}{\Delta x} \tag{1.5}$$

where the grid spacing defined earlier is used as the difference, Δx.

The approximation in Eq. (1.5) converges to the true derivative as $\Delta x \to 0$. Thus, the grid spacing would need to be chosen to be as fine as possible at the cost of computation time. The FDTD method can clearly only provide a simulation over a finite space and so boundary conditions need to be chosen accordingly. For infinite systems, a perfectly matched layer (PML) can be used to completely cancel reflected solutions as the simulation boundary thus providing a good approximation for a boundless system.

The FDTD method is very different to the RSE method, which uses the concept of resonant states instead of directly calculating the fields in the system. The FDTD method is limited by the spatial and temporal truncation in the calculation whereas the RSE method in limited in the inverse space: wavevector and frequency. The main drawback of the FDTD method is the computation time which can become excessively long for large computational domains. One of the main advantages of the RSE is it's computational simplicity, leading to short computation times.

1.4.2 Guided Mode Expansion

The guided mode expansion (GME) is the most similar existing method to the RSE [54]. The basic description of the method is fundamentally the same as the

RSE: given a set of basis modes and a perturbation to the system, the GME can calculate the optical modes for the perturbed system. Many of the equations are also similar; the perturbed modes are found via an eigenvalue equation. The crucial difference between the two methods is that the GME relies solely on the guided modes of the system, not taking into account any leaky modes unlike the RSE which takes into account all modes of the system.

The GME is still able to calculate scattering modes in the perturbed system by investigating the coupling between guided modes and scattering modes. This allows for an approximation of the Q-factor, and thus the imaginary part of the mode eigenfrequency. The GME is a perhaps more natural method since it only considers real modes without the added abstraction of complex resonant states and cut modes, however this added complexity allows the RSE to perform well with a wider variety of perturbations since it allows for the treatment of lossy systems.

The calculation of the Q-factor in the GME assumes that the coupling between scattering modes is negligible compared to the coupling between guided modes and scattering modes. This assumption works well for low loss systems (which are typically the systems of interest) but becomes inaccurate for lossy systems. The RSE can calculate the modes of lossy systems more accurately since the basis set of modes already includes the leaky information through the Fabry-Perot modes without the need for an additional approximation.

Overall, the GME represents a special case of the RSE where only guided modes are included in the basis under the assumption that the system losses are low.

1.5 Green's Function of a linear operator

The RSE perturbs RSs of a simple system to the RSs of a complex system. The RSE ultimately gains this property from Green's function which can be used to find a function $g(x)$, using only the knowledge of Green's function $G(x, x')$ and a source term $f(x')$. For a linear operator $L(x)$ where $L(x)f(x) = g(x)$, Green's function is defined as: $L(x)G(x, x') = \delta(x - x')$. Green's function can be used in the following way:

$$g(x) = \int G(x, x')f(x')dx' \tag{1.6}$$

The resonances of a photonic system are the equivalent to the resonances of an oscillator e.g a bell. When a bell is struck, the intensity of the produced sound decays exponentially over time. Likewise, we can excite a photonic system with some incident electric field and we can produce outgoing electric fields which decay exponentially over time. This is represented mathematically by the intensity, $I(t) = I_0 \exp(-\Gamma t)$ where I_0 is the initial intensity and Γ is the decay rate. The amplitude of this decaying intensity at the frequency Ω is given by $I = |A|^2$ and can be represented by $A(\Omega) = A_0 \exp(-i\Omega t - \frac{\Gamma}{2t})$.

To find the resonances of such a system, we Fourier transform this amplitude which is given in the form: $A(\omega) = B(\omega)/(\omega - \omega_n)$ where $\omega_n = \Omega_n - i\Gamma_n/2$ are poles of the amplitude in frequency space, these are the RSs of the photonic system, the frequencies and electric fields of which are in general complex with real part Ω and imaginary part $\Gamma/2$.

1.6 Green's dyadic of an optical system

We now need to translate this general description of the resonances into something specific to a photonic system which we achieve by using Green's function

(GF) of Maxwell's wave equation (MWE).

Maxwell's wave equation can be described in matrix form [55]:

$$\begin{pmatrix} \frac{\omega}{c}\epsilon & -\nabla\times \\ -\nabla\times & \frac{\omega}{c}\mu \end{pmatrix} \begin{pmatrix} \mathbf{E} \\ i\mathbf{H} \end{pmatrix} = \vec{J} \tag{1.7}$$

where $\nabla\times$ is the three dimensional curl operator, $\mathbf{E}$ and $\mathbf{H}$ are the electric and magnetic field vectors and $\vec{J}$ is the source current which is made up of an electric part $\vec{J}_e$ and magnetic part $\vec{J}_m$. This can be written in a compact form:

$$\hat{M}\vec{F} = \vec{J}. \tag{1.8}$$

The definition of GF is given by:

$$\hat{M}(\mathbf{r};\omega)\hat{G}(\mathbf{r},\mathbf{r}';\omega) = \hat{I}\delta(\mathbf{r}-\mathbf{r}'), \tag{1.9}$$

which we can then use to define the field vector $\vec{F}$:

$$\vec{F}(\mathbf{r};\omega) = \int d\mathbf{r}'\hat{G}(\mathbf{r},\mathbf{r}';\omega)\vec{J}(\mathbf{r}';\omega). \tag{1.10}$$

We know that $\vec{F}$ has poles which are the eigenfrequencies of the RSs. The source term $\vec{J}$ has no poles so therefore the RSs must be poles of the GF. This allows the GF to be represented as a sum over the RSs using Mittag-Leffler's theorem (see Appendix B where we derive the ML form of the GF) which is a crucial property of the GF and provides the foundation for the resonant-state expansion.

1.7 Complex Analysis

The fundamental mathematical basis for this thesis is the understanding of complex numbers and the complex plane. Namely, the RSE is heavily dependant on Cauchy's integral theorem and Mittag-Leffler's theorem. These concepts are crucial to the understanding of the derivation of the RSE.

1.7.1 Cauchy's Integral Theorem

In this section we will prove Cauchy's integral theorem which shows that for an analytic function - any that can be written as a convergent power series - $f(z)$ and a contour C which forms a closed loop, the contour integral vanishes:

$$\oint_C f(z)dz = 0 \tag{1.11}$$

Firstly, we use an intermediate step showing that $\oint_C z^n dz = 0$ for integer $n \neq -1$ which we will need for the proof.

Consider the complex function $f(z) = z^n$ where $n \neq -1$. Also consider the contour integral of $f(z)$ along a contour C which is a circle of radius $r > 0$ about $z = 0$ taken in the positive (anti-clockwise) direction: $\oint_C f(z)dz$. Since the integration is taken along a circle it is convenient to parameterise the function as $z = re^{i\theta}$ and $dz = ire^{i\theta}d\theta$, the integral then becomes:

$$\begin{aligned} \oint_C z^n dz &= ir^{n+1} \int_0^{2\pi} e^{i(n+1)\theta} d\theta \\ &= ir^{n+1}[i(n+1)]^{-1} \left[e^{i(n+1)\theta}\right]_0^{2\pi} \\ &= 0 \quad \text{for} \quad n \neq -1 \end{aligned} \tag{1.12}$$

which is a result that is independent of r.

Now we can prove Cauchy's integral theorem (Eq. (1.11))using the Cauchy-Goursat proof [57]. We subdivide an arbitrary closed contour C into a series of squares as in Fig. 1.3

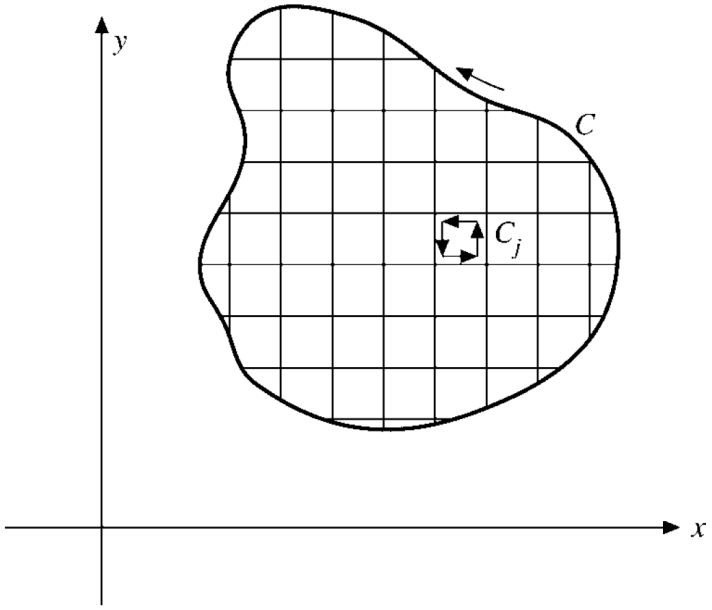

Figure 1.3: Schematic showing the subdivision of a contour C into a series of squares describing subcontours C_j. Image is from [57].

The integral along C is then given as a sum over each of the squares, C_j:

$$\oint_C f(z)dz = \sum_j \oint_{C_j} f(z)dz \tag{1.13}$$

where the integrals along interior lines cancel since each line has two integrals coming from neighbouring C_j, but in opposite directions.

We define $\delta_j(z, z_j)$ as the difference between the derivative at an interior point within the contour C_j, z_j, using the grid spacing and the true derivative using dz:

$$\delta_j(z, z_j) = \frac{f(z) - f(z_j)}{z - z_j} - \left.\frac{df(z)}{dz}\right|_{z=z_j} \tag{1.14}$$

so that $\delta_j(z, z_j) \to 0$ as the grid spacing becomes finer. We solve Eq. (1.14) for $f(z)$ and then integrate along C_j:

$$\oint_C f(z)dz = \oint_C (z - z_j)\delta_j(z, z_j)dz + \left.\frac{df}{dz}\right|_{z=z_j} \oint_C (z - z_j)dz + f(z_j) \oint_C dz \tag{1.15}$$

Using Eq. (1.12), we know that $\oint_C dz = 0$ and $\oint_C z dz = 0$ which leaves:

$$\oint_{C_j} f(z)dz = \oint_{C_j} (z - z_j)\delta_j(z, z_j)dz. \tag{1.16}$$

Introducing the condition:

$$|\delta_j(z, z_j)| < \epsilon, \tag{1.17}$$

where ϵ is an arbitrary small quantity which implies the condition:

$$\left| \sum_j \oint_{C_j} f(z)dz \right| < A\epsilon \tag{1.18}$$

where A is a term of the order of the area enclosed by C_j. We are now free to let $\epsilon \to 0$ which leads to Cauchy's integral theorem:

$$\oint_C f(z)dz = 0. \tag{1.19}$$

This has the consequence that the integral of an analytic function is independent of the path taken, depending only on the end points.

1.7.2 Residue Theorem

In extension to this is the meromorphic function which is a holomorphic function (satisfies Cauchy-Riemann conditions) except for a countable number of poles.

A contour integral around a pole z_0 does not obey Eq. (1.19) which only holds for analytic functions. Instead let us consider the Laurent expansion of the meromorphic function $f(z)$:

$$f(z) = \sum_{n=-\infty}^{\infty} a_n (z - z_0)^n. \tag{1.20}$$

We apply a contour integral about the point z_0 to each of these terms:

$$a_n \oint (z - z_0)^n dz = a_n \left. \frac{(z - z_0)^{n+1}}{n+1} \right|_{z_1}^{z_1} = 0 \quad \text{for} \quad n \neq -1 \tag{1.21}$$

where due to Eq. (1.19) we can replace the contour integral with just the end-points, which are obviously the same point for a closed contour (this is actually only possible if the function is holomorphic and it can be shown that this is satisfied for all $n \neq -1$). Such an integral clearly evaluates to zero. However, the denominator presents a problem in the case of $n = -1$ where we instead parameterise the problem as $z = re^{i\theta}$:

$$a_{-1} \oint (z - z_0)^{-1} dz = a_{-1} \oint \frac{ire^{i\theta}}{re^{i\theta}} d\theta = 2\pi i a_{-1} \tag{1.22}$$

In summary:

$$\frac{1}{2\pi i} \oint f(z) dz = a_{-1} \tag{1.23}$$

So for a function $f(z)$ containing a pole z_0, a contour integral which contains that pole is simply equal to the $n = -1$ coefficient of the Laurent expansion of the function, a_{-1} which is known as the residue of $f(z)$ at $z = z_0$.

In fact, for a simple pole (a function is said to have a simple pole if the coefficients of the Laurent series, a_n are zero for $n < -1$, that is it is a pole of order 1) the definition of the residue for the pole z_0 can be given by:

$$\mathrm{Res}(f, z_0) = \lim_{z \to z_0} (z - z_0) f(z) \tag{1.24}$$

Eq. (1.23) is easily extended to a contour integral containing several poles, z_n with residues $\mathrm{Res}(f, z_n)$:

$$\oint f(z) = 2\pi i \sum_n \mathrm{Res}(f, z_n) \tag{1.25}$$

1.7.3 Mittag-Leffler Theorem

Residue theorem states that the contour integral about a pole of a function is equal to the residue of the pole. Mittag-Leffler theorem asserts that the function itself can be described by a sum over all its poles, z_n:

$$f(z) = \sum_n \frac{\mathrm{Res}(f, z_n)}{z - z_n}. \tag{1.26}$$

This is the form of the Mittag-Leffler theorem for $f(z \to \infty) = 0$.

The function $f(z)$ has a number of fixed poles which cannot be altered except by altering $f(z)$. Instead we create a new pole at ζ which can be modified freely allowing us to explore the pole structure of the function. We therefore construct the function $f(z)/(z - \zeta)$ where $z = \zeta$ is not a pole of $f(z)$ [58]. So the whole function $f(z)/(z - \zeta)$ has poles at $z = z_n$ and at $z = \zeta$.

The poles are ordered such that $|z_0| < |z_1| < |z_2| \cdots < |z_N|$ so there exists a circle C_N that contains all the poles up to z_N and no others. The radius of the circle C_N is given by R_N where $R_N \to \infty$ as $N \to \infty$

By taking a contour integral of $f(z)/(z - \zeta)$ along C_N and using Eqs. (1.24) and (1.25):

$$\begin{aligned}
\frac{1}{2\pi i}\oint_{C_N}\frac{f(z)}{z-\zeta}dz &= \mathrm{Res}\left(\frac{f(z)}{z-\zeta},\zeta\right)+\sum_n^N \mathrm{Res}\left(\frac{f(z)}{z-\zeta},z_n\right)\\
&= \lim_{z\to\zeta}\left(\frac{(z-\zeta)f(z)}{z-\zeta}\right)+\sum_n^N\lim_{z\to z_n}\left(\frac{(z-z_n)f(z)}{z-\zeta}\right)\\
&= \lim_{z\to\zeta}f(z)+\sum_n^N\left(\lim_{z\to z_n}\left[(z-z_n)f(z)\right]\lim_{z\to z_n}\frac{1}{z-\zeta}\right)\\
&= f(\zeta)+\sum_n^N\frac{\mathrm{Res}(f,z_n)}{z_n-\zeta}. \qquad (1.27)
\end{aligned}$$

We ultimately want an expression for $f(\zeta)$ which will become the left hand side of Eq. (1.26). To do this we want to remove the contour integral in Eq. (1.27), this is possible if the integrand is in a specific form which we achieve by setting $\zeta = 0$:

$$\frac{1}{2\pi i}\oint_{C_N}\frac{f(z)}{z}dz = f(0)+\sum_n^N\frac{\mathrm{Res}(f,z_n)}{z_n} \qquad (1.28)$$

and taking the difference between Eqs. (1.27) and (1.28):

$$\frac{1}{2\pi i}\oint_{C_N} f(z)\left(\frac{1}{z-\zeta}-\frac{1}{z}\right)dz =$$
$$f(\zeta)+\sum_n^N\mathrm{Res}(f,z_n)\left(\frac{1}{z_n-\zeta}-\frac{1}{z_n}\right)-f(0). \qquad (1.29)$$

Now it can be shown that the integral on the right hand side of the above equation is equal to zero as $N\to\infty$. We define the maximum value of $|f(z)|$ which is when z is taken on the contour C_N which has a radius R_N where $|f(R_N)| = M$.

Therefore:

$$\begin{aligned}\left|\frac{1}{2\pi i}\oint_{C_N} f(z)\left(\frac{1}{z-\zeta}-\frac{1}{z}\right)dz\right| &= \left|\frac{\zeta}{2\pi i}\oint_{C_N}\frac{f(z)}{z(z-\zeta)}dz\right| \\ &\leq \frac{|\zeta|}{2\pi}\frac{M}{R_N(R_N-|\zeta|)}2\pi R_N \\ &\propto \frac{1}{R_N} \\ &\to 0 \quad \text{for} \quad N\to\infty \end{aligned} \tag{1.30}$$

where we have used the triangle inequality for contour integrals: $|\int_C f(z)dz| \leq ML$ where L is the length of the contour C, which in this case is given by $2\pi R_N$. Again, the above is only true is $f(z\to\infty)=0$.

Now we can rearrange Eq. (1.29) using $N\to\infty$ and substituting $\zeta\to z$:

$$f(z) = f(0) + \sum_n \text{Res}(f,z_n)\left(\frac{1}{z-z_n}+\frac{1}{z_n}\right). \tag{1.31}$$

This is the general form of Mittag-Leffler expansion, however in this thesis we will be expanding a function $f(z)\to 0$ as $z\to\infty$, which will lead us to Eq. (1.26). If we investigate this in the above equation:

$$\begin{aligned} f(\infty)=0 &= f(0)+\sum_n \text{Res}(f,z_n)\left(\frac{1}{\infty-z_n}+\frac{1}{z_n}\right) \\ 0 &= f(0)+\sum_n \frac{\text{Res}(f,z_n)}{z_n}. \end{aligned} \tag{1.32}$$

Thus, Eq. (1.31) modifies to Eq. (1.26). This is an exact form which converges to the analytic form of $f(z)$ as the number of poles in the summation increases.

Shown for illustration in Fig. 1.4 is the analytic [Eq. (C.3)] and Mittag-Leffler form of Green's function of Maxwell's wave equation for the homogeneous dielectric slab at normal incidence. The poles of this GF are the RSs shown in

Fig. 1.1. It can be seen that the Mittag-Leffler form of the GF converges to the analytic form as the number of poles in the summation, N is increased. The Mittag-Leffler form of the GF is discussed further in Appendix B.

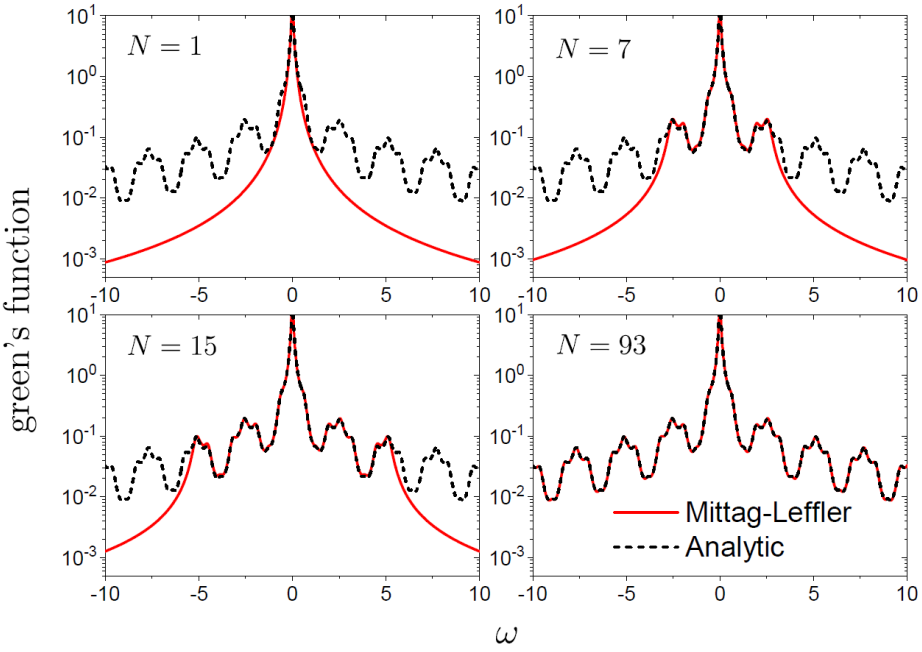

Figure 1.4: The Mittag-Leffler form of the GF for the homogenous dielectric slab against the real frequency, ω shown with 1 pole, 7 poles, 15 poles and 93 poles in the summation with $\varepsilon = 6$ and $a = 1$. Also plotted is the analytic form of the GF with $z = -z' = 0.5$, given in Appendix B.

1.8 Normal incidence RSE for homogeneous perturbations

To demonstrate the underlying simplicity of the RSE method, we can derive a simple form of the RSE for normal incidence and homogeneous perturbations to the permittivity or permeability as discussed in [55]. This form is much simpler

than the photonic crystal RSE (PC-RSE) derived in the next chapter since the normal incidence does not include any cuts and the homogeneous perturbation does not cause coupling between Bragg harmonics.

This simple example will use a homogeneous dielectric slab as a basis system to which we apply a homogeneous perturbation to the permittivity. The slab is infinite in the x- and y-directions and has width $2a$ in the z-direction. The slab is suspended in a vacuum ($\varepsilon = 0$) and light is incident from the z-direction.

We start with the wave equation for the electric field:

$$(\varepsilon\omega^2 + \partial_z^2)E(z) = 0 \tag{1.33}$$

where ε is the permittivty of the slab, ω is the frequency of the field and $E(z)$ is the y-direction electric field.

We add a perturbation to the permittivity, $\Delta\varepsilon(z)$ so the wave equation becomes:

$$(\varepsilon\omega^2 + \partial_z^2)E(z) = -\omega\Delta\varepsilon(z)E(z). \tag{1.34}$$

Using the GF, we can solve for the electric field:

$$E(z,\omega) = -\omega \int G(z,z',\omega)\Delta\varepsilon(z)E(z',\omega)dz'. \tag{1.35}$$

We can then use the Mittag-Leffler theorem to write the GF in a spectral form:

$$G(z,z',\omega) = \sum_n \frac{\mathrm{Res}(G,\omega_n)}{\omega - \omega_n} \tag{1.36}$$

It is shown in Appendix B that $\mathrm{Res}(G,\omega_n) = E_n(z)E_n(z')/\omega_n$ where E_n are the electric fields for the unperturbed system which are properly normalised as:

$$2\varepsilon_s \int_{-a}^{a} E_n^2(z)dz - \frac{E_n^2(a) + E_n^2(-a)}{ik_n} = 1, \tag{1.37}$$

which is required by the ML theorem. By also using the expansion $E(z) = \sum_n c_n E_n(z)$, Eq. (1.35) becomes:

$$\sum_n c_n E_n(z) = -\omega \sum_n \frac{E_n(z)}{\omega - \omega_n} \sum_m V_{nm} c_m \tag{1.38}$$

where $V_n m$ is a perturbation matrix given by:

$$V_{nm} = \int E_n(z) \Delta\varepsilon(z) E_m(z) dz \tag{1.39}$$

By equating coefficients at $E_n(z)$ we arrive at the homogeneous, normal incidence RSE:

$$(\omega - \omega_n) c_n = -\omega \sum_m V_{nm} c_m \tag{1.40}$$

where the eigenvalues ω are the frequencies of the perturbed system.

Using Eq. (1.40), we can apply a perturbation to the permittivity of a homogeneous dielectric slab. We apply the perturbation to the system described in Fig. 1.1 by increasing the permittivity from $\varepsilon = 6$ to $\varepsilon = 7$ i.e $\Delta\varepsilon = 1$ and $\Delta\mu = 0$. We can see in Fig. 1.5 that the positive perturbation to the permittivity causes a simple change to the modes. This is a simple evolution due to the simplicity of the system, in later chapters this evolution of modes will become much more complex.

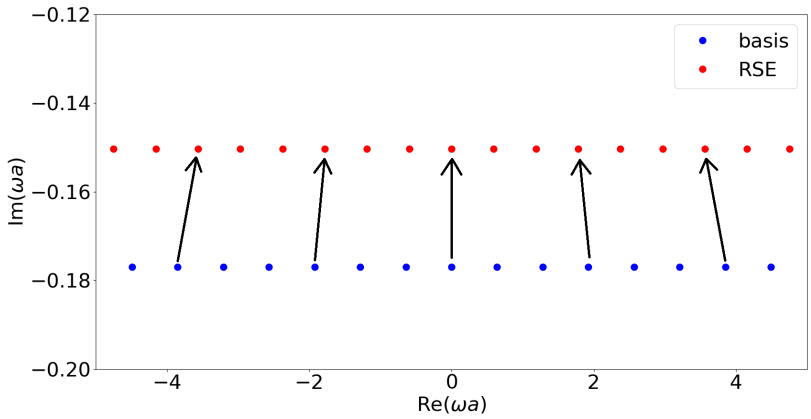

Figure 1.5: RSs of a homogeneous dielectric slab with the permittivity of the basis system $\varepsilon = 6$ (blue) and permittivity of the perturbed system $\varepsilon = 7$ calculated via the RSE Eq. (1.40) (red).

1.9 Layout of this thesis

We will first show the derivation of the RSE specifically for photonic crystals, called the PC-RSE. This will be for a general system with a periodic perturbation naturally described by a Fourier series.

We will then focus on a specific photonic crystal modelled as a homogeneous dielectric slab with a cosine perturbation to its permittivity. We will find the RSs of the photonic crystal in frequency space by using a homogenous slab as a basis. The results of the RSE will be compared to the SMM which is considered as an exact result.

We can then investigate the origin of these modes by slowly varying system parameters and tracking the mode positions and by investigating the weights of each of the basis mode contributions to a selection of perturbed modes.

We will then expand on those results by investigating the BICs of the system

and using the RSE as a tool to explain the origin of these modes and also how the morphology of the electric field changes as a mode "passes through" a BIC with system parameter changes.

Chapter 2

Formalism of the PC-RSE

In this chapter we will present the formalism of the resonant-state expansion method for a photonic crystal using a homogeneous dielectric slab as a basis. In the previous chapter, the RSE method was derived for a homogeneous perturbation which was fairly straightforward as a homogeneous system does not scatter light. Here, we will be introducing a periodic perturbation which will scatter light and greatly increase the complexity of the problem since we now have to introduce the concept of coupled Bragg channels. Additionally, we must deal with the branch cuts which would prevent the resultant RSs from converging to the correct solutions if not properly treated.

2.1 Formulation of problem

Consider a PC slab occupying the region $|z| \leqslant a$, where z is the coordinate in the growth direction. Assuming the permittivity and the permeability are isotropic everywhere, the electric field $\mathbf{E}$, magnetic field $\mathbf{H}$, and the frequency ω of a given RS of the PC slab satisfy the following Maxwell equations (using

the speed of light as $c = 1$)

$$\nabla \times \mathbf{E} = \omega(\mu + \Delta\mu) i\mathbf{H}\,, \tag{2.1}$$

$$\nabla \times i\mathbf{H} = \omega(\varepsilon + \Delta\varepsilon)\mathbf{E}\,, \tag{2.2}$$

which have to be solved together with outgoing wave BCs outside the PC slab. Here, we have explicitly separated the total permittivity (permeability), periodic in x-direction with the period d, into a homogeneous part $\varepsilon(z)$ ($\mu(z)$) and a periodic part $\Delta\varepsilon(x,z)$ ($\Delta\mu(x,z)$), obeying

$$\Delta\varepsilon(x+d,z) = \Delta\varepsilon(x,z)\,, \quad \Delta\mu(x+d,z) = \Delta\mu(x,z)\,. \tag{2.3}$$

For the purpose of a clearer illustration of our approach, we consider the case of the transverse electric (TE) and transverse magnetic (TM) polarisations not coupled to each other, which is achieved by assuming that the y-component of the in-plane momentum is zero. We note, however, that generalisation to the case of a non-zero y-component of the momentum and to 2D periodicity of the PC slab is straightforward, and the whole formalism remains essentially the same as presented here.

Since the TE and TM polarisations are not coupled, each polarisation can be treated separately. However, due to the symmetry of Maxwell's equations (2.1) and (2.2) with respect to a simultaneous exchange of $\mathbf{E} \leftrightarrow i\mathbf{H}$, $\varepsilon \leftrightarrow \mu$, and $\Delta\varepsilon \leftrightarrow \Delta\mu$, it is sufficient to treat only one of the two polarisations, for example, the TE polarisation, while retaining the permeability in all results, even if all the constituent materials are non-magnetic.

For the TE polarisation, Maxwell's equations (2.1) and (2.2) reduce to

$$(\hat{M} + \Delta\hat{M})\mathbf{F} = 0\,, \tag{2.4}$$

where the vector field $\mathbf{F}$ is formed from three nonvanishing components of the electric and magnetic fields,

$$\mathbf{F} = \begin{pmatrix} E_y \\ iH_x \\ iH_z \end{pmatrix}, \tag{2.5}$$

and

$$\hat{M}(x,z;\omega) = \omega\hat{P}(z) - \hat{D}(x,z)\,, \tag{2.6}$$

$$\Delta\hat{M}(x,z;\omega) = \omega\Delta\hat{P}(x,z) \tag{2.7}$$

are linear operators, consisting of the generalized permittivity [55]

$$\hat{P}(z) = \begin{pmatrix} \varepsilon(z) & 0 & 0 \\ 0 & \mu(z) & 0 \\ 0 & 0 & \mu(z) \end{pmatrix}, \tag{2.8}$$

the curl operator

$$\hat{D}(x,z) = \begin{pmatrix} 0 & \partial_z & -\partial_x \\ -\partial_z & 0 & 0 \\ \partial_x & 0 & 0 \end{pmatrix}, \tag{2.9}$$

and the perturbation

$$\Delta\hat{P}(x,z) = \begin{pmatrix} \Delta\varepsilon(x,z) & 0 & 0 \\ 0 & \Delta\mu(x,z) & 0 \\ 0 & 0 & \Delta\mu(x,z) \end{pmatrix}. \tag{2.10}$$

Note that the polarisation matrices, $\hat{P}$ and $\Delta\hat{P}$ are non-dispersive. Frequency dispersion can be included but would require a reformulation of the PC-RSE in

accordance with [56].

2.2 Derivation of central PC-RSE equation

Owing to the periodicity in the x-direction, the wave function $\mathbf{F}$ obeys Bloch's theorem,

$$\mathbf{F}(x+d,z) = \mathbf{F}(x,z)e^{ipd}\,, \tag{2.11}$$

determining the quasimomentum p in the x-direction. We therefore solve the Maxwell equations (2.4) for the given p, using a *periodic* dyadic Green's function (GF) $\hat{G}_p(x;z,z')$ of the homogeneous slab:

$$\mathbf{F}(x,z) = -\frac{\omega}{d}\int_d dx' \int dz' \hat{G}_p(x-x';z,z')\Delta\hat{P}(x',z')\mathbf{F}(x',z'), \tag{2.12}$$

where $\int_d dx$ implies integration over any period interval. This GF has the same value of p and satisfies Maxwell's equations with a periodic array of sources:

$$\hat{L}(x,z;\omega)\hat{G}_p = \hat{\mathbf{1}}\delta(z-z')d\sum_m e^{ipmd}\delta(x-x'-md)\,, \tag{2.13}$$

where m is an integer and $\hat{\mathbf{1}}$ is the 3×3 unit matrix. Using Bloch's theorem again, the periodic GF can be written as

$$\hat{G}_p(x;z,z') = \sum_g \hat{\mathcal{G}}_{p+g}(z,z')e^{i(p+g)x}\,, \tag{2.14}$$

where

$$g = \frac{2\pi m}{d} \quad \text{where} \quad m = 0, \pm 1, \pm 2..., \tag{2.15}$$

and $\hat{\mathcal{G}}_p(z,z')$ is another, x-independent GF of the homogeneous slab satisfying an equation

$$\hat{\mathcal{L}}_p(z;\omega)\hat{\mathcal{G}}_p(z,z') = \hat{\mathbf{1}}\delta(z-z')\,, \tag{2.16}$$

with a modified operator

$$\hat{\mathcal{L}}_p(z;\omega) = \omega\hat{P}(z) - \hat{\mathcal{D}}_p(z)\,, \tag{2.17}$$

which consists of the homogeneous generalized permittivity $\hat{P}(z)$ given by Eq. (2.8) and the curl operator $\hat{\mathcal{D}}_p(z)$ given by Eq. (2.9) with ∂_x replaced by ip: $\hat{\mathcal{D}}_p(z) = \hat{D}_{\partial_x \to ip}$.

The homogeneous GF $\hat{\mathcal{G}}_p$ can be written, using the Mittag-Leffler (ML) theorem [57], in terms of the RSs of the homogeneous slab,

$$\hat{\mathcal{G}}_p(z,z') = \sum\!\!\!\!\!\!\int_n \frac{\boldsymbol{\mathcal{F}}_n(z;p) \otimes \boldsymbol{\mathcal{F}}_n(z';-p)}{\omega - \omega_n} \tag{2.18}$$

where $\sum\!\!\!\!\!\!\int$ represents the sum over the RSs of the homogeneous slab, supplemented with an integral over the branch cuts that are caused by the square root in the wave vector when using ω-representation (see Appendix B). $\boldsymbol{\mathcal{F}}_n(z;p)$ is the vectorial wave function of the RS n of the homogeneous slab, satisfying Maxwell's equation

$$\hat{\mathcal{L}}_p(z;\omega_n)\boldsymbol{\mathcal{F}}_n(z;p) = 0 \tag{2.19}$$

and outgoing BCs, and ω_n is the RS eigenfrequency. Equation (2.18) is valid if the RSs are normalised according to a general normalisation condition [55, 59] applied to the homogeneous planar system,

$$1 = \int_{z_1}^{z_2} \boldsymbol{\mathcal{F}}_n^\dagger \cdot \hat{P}\boldsymbol{\mathcal{F}}_n dz + \left(\boldsymbol{\mathcal{E}}_n^\dagger \times i\boldsymbol{\mathcal{H}}_n' - \boldsymbol{\mathcal{E}}_n' \times i\boldsymbol{\mathcal{H}}_n^\dagger\right) \cdot \mathbf{e}_z \Big|_{z_1}^{z_2}\,, \tag{2.20}$$

where $\mathbf{e}_z$ is the unit vector in the z-direction, z_1 and z_2 are two arbitrary coordinates outside of the system, such that $z_1 \leqslant -a$ and $z_2 \geqslant a$, and $\boldsymbol{\mathcal{F}}_n^\dagger(z;p) = \boldsymbol{\mathcal{F}}_n(z;-p)$ is the adjoint field. $\boldsymbol{\mathcal{E}}_n$ and $\boldsymbol{\mathcal{H}}_n$ in Eq. (2.20) are, respectively, the electric and magnetic fields of the RS n, combined together into the vector

$\boldsymbol{\mathcal{F}}_n = \{\boldsymbol{\mathcal{E}}_n, i\boldsymbol{\mathcal{H}}_n\}$ having in general six components which are reduced to only three for TE or TM polarisation, in accordance with Eq. (2.5); $\boldsymbol{\mathcal{E}}'_n$ and $\boldsymbol{\mathcal{H}}'_n$ are the frequency derivatives of the analytic continuation of the fields $\boldsymbol{\mathcal{E}}_n$ and $\boldsymbol{\mathcal{H}}_n$ into the complex frequency plane (for more details see [12, 55]). Note that in addition to all the RSs lying on the "physical" Riemann sheet of complex frequency, the ML series Eq. (2.18) includes also *cut modes*, not obeying Eqs. (2.19) and (2.20) which is explained further below in Ch. 2.3.

Substituting Eq. (2.14) into Eq. (2.12) and using the ML expansion Eq. (2.18), we obtain, owing to the completeness of the basis and in agreement with Bloch's theorem, an expansion of the wave function $\mathbf{F}$ of the RS of the PC slab into the RSs of the homogeneous slab,

$$\mathbf{F}(x,z) = \sum_g \sum\!\!\!\!\!\!\int_n c_n^g \boldsymbol{\mathcal{F}}_n(z; p+g) e^{i(p+g)x}\,, \tag{2.21}$$

where the expansion coefficients are given by

$$\begin{aligned} c_n^g &= -\frac{\omega}{\omega-\omega_n^g}\frac{1}{d}\int_d dx e^{-i(p+g)x} \\ &\quad \times \int dz \boldsymbol{\mathcal{F}}_n(z; -p-g)\cdot \Delta\hat{P}(x,z)\mathbf{F}(x,z)\,. \end{aligned} \tag{2.22}$$

Then, substituting the expansion Eq. (2.21) into Eq. (2.22), we arrive at the the key equation of the PC-RSE:

$$\omega \sum_{g'} \sum\!\!\!\!\!\!\int_{n'} \left(\delta_{nn'}\delta_{gg'} + V_{nn'}^{gg'}\right) c_{n'}^{g'} = \omega_n^g c_n^g\,, \tag{2.23}$$

in which δ_{ij} is the Kronecker delta, and the matrix elements of the perturbation are defined as

$$V_{nn'}^{gg'} = \int \boldsymbol{\mathcal{F}}_n(z; -p-g)\cdot \Delta\hat{P}_{g-g'}(z)\boldsymbol{\mathcal{F}}_{n'}(z; p+g')dz \tag{2.24}$$

with $\Delta\hat{P}_g(z)$ being the Fourier coefficients of the generalized permittivity perturbation,

$$\Delta\hat{P}_g(z) = \frac{1}{d}\int_d \Delta\hat{P}(x,z)e^{-igx}dx\,. \tag{2.25}$$

Note that in Eqs. (2.22) and (2.23), we have added index g to ω_n in order emphasize the dependence of the basis RS frequencies on the Bragg channel number g.

Equation (2.23) presents a matrix eigenvalue problem, linear in ω (the eigenfrequency of a perturbed RS of the PC slab) and can be solved simply by diagonalizing a complex symmetric matrix. This equation is very similar to the RSE equation for a finite open optical system [13]. However, the main difference between the two is that Eq. (2.23) contains a summation over all Bragg channels, labeled by the index g. Also, the contribution of the cuts, denoted by the integral, is included in Eq. (2.23), in the same way as it was done in the RSE applied to 2D open optical systems [11] or to inhomogeneous waveguides [16].

Note that the RSE has been recently formulated for PC systems [59, 60], in a form of a perturbation theory treating some modifications of the already existing periodic structure, i.e. using a PC slab as a basis system. It has been applied so far to either weak perturbations, limiting the RSE basis to a single mode [60], or to moderate perturbations of quasi-degenerate modes, limiting the basis to such a pair of modes [59]. In the present work we consider instead a homogeneous basis containing up to several thousands of modes of the homogeneous basis. This choice of the basis presents a significant advantage in implementation of the RSE. For example, all different Bragg channels are fully isolated in the homogeneous basis, whereas a PC basis has all these channels already coupled together. This has, in particular, a dramatic consequence on inclusion of the branch cuts in the basis, which is impossible to do in practice with Bragg channels mixed up as in the PC basis. Furthermore, owing to the

simplicity of the basis system used in the present approach, all the basis RSs and cut modes are found analytically.

2.3 Branch cuts in frequency

As mentioned above, the dispersion relation between the wavevector k and the frequency ω causes branch cuts in the complex plane. The dispersion is given by

$$k = \sqrt{\omega^2 - p^2} \tag{2.26}$$

which produces cuts at $\pm p$. These cuts have a real effect on the transmission spectrum of a photonic crystal which are visible as Rayliegh-Wood anomalies corresponding to the opening of a diffractive order [33, 34]. The Mittag-Leffler theorem used to generate the spectral form of the GF in (2.18), requires that the GF be holomorphic everywhere except for a countable number of poles. The presence of cuts introduces a discontinuity which violates this requirement but this can be accounted for with a contour integral taken around the cut which is shown in Appendix B. For the RSE however, we need to discretise the cuts in order to generate artificial RS-like cut poles which can be added to the basis.

The discretisation of the cuts is done following the procedure described in [11,16]. For each parity s, the cut with the branch point at $\omega = p$ is divided into N_c intervals bounded by $[\tilde{\omega}_\nu, \tilde{\omega}_{\nu+2}]$, where ν is even (odd) for $s = +$ ($s = -$), with a weight given by

$$W_s = \int_{\tilde{\omega}_\nu}^{\tilde{\omega}_{\nu+2}} \sqrt{|\sigma_s(\omega)|} d\omega \,, \tag{2.27}$$

where σ_s is the cut weight function. The integral is taken along the cut starting at the branch point: $\tilde{\omega}_1 = \tilde{\omega}_2 = p$. The cut is split into intervals in such a way that W_s is the same for each interval (for the given parity s). Within each

interval, an artificial cut mode is defined at the frequency ω_ν, given by

$$\omega_\nu = \frac{1}{C_\nu} \int_{\tilde{\omega}_\nu}^{\tilde{\omega}_{\nu+2}} \sigma_s(\omega) \omega d\omega \tag{2.28}$$

with $\nu = 1, 2, \ldots, 2N_c$, where $s = (-1)^\nu$ and

$$C_\nu = \int_{\tilde{\omega}_\nu}^{\tilde{\omega}_{\nu+2}} \sigma_s(\omega) d\omega \,. \tag{2.29}$$

Applying the same discretisation to the other cut with the branch point at $\omega = -p$ and extending the ν numbers to negative integers, we have now defined a series of artificial cut modes which lie along the cut and will compensate for the discontinuity introduced by the dispersion relation.

These cuts are then added to the basis which modifies Eq. (2.23) to:

$$\omega \sum_{\bar{n}g'} \left(\delta_{\bar{n}\bar{n}'} \delta_{gg'} + V^{gg'}_{\bar{n}\bar{n}'} \right) c^{g'}_{\bar{n}'} = \omega^g_{\bar{n}} c^g_{\bar{n}} \tag{2.30}$$

where the sum-integral $\sum\!\!\!\!\!\!\int$ has been replaced by a regular sum with index $\bar{n}$ labeling both the RS and the cut modes.

2.4 Conclusion

In this chapter, we derived the central RSE equation for a photonic crystal system described by a periodic perturbation to either the permittivity or permeability of another photonic system. We used the Green's function of Maxwell's wave equation to equate the fields of the perturbed system with those of the basis system. Mittag-Leffler theorem then allowed us to represent the Green's function as a summation of its poles in frequency space which are defined as the resonant states of the system.

Additionally, we have shown that the branch cuts in the complex plane due to a square root in the dispersion relation between frequency and wavevector cause complications to the RSE by splitting the resonant states across two Riemann sheets. We solve this by discretising the cuts themselves into a series of artifical cut poles which lie along the cuts. These artificial poles are then added to the basis resonant states.

Chapter 3

PC-RSE applied to a photonic crystal slab

Now that we have derived the PC-RSE, we will be applying it to a specific system. We apply the RSE to a photonic crystal characterised by a permittivity described by a cosine wave. A homogeneous dielectric slab with constant permittivity will be used as a basis system, this is the system described in Ch. 1.1.1. To this, the cosine permittivity is treated as a perturbation on top of the homogeneous slab.

We will then compare the results of the RSE to a well-known method: the scattering matrix method, described in detail in Appendix F, in order to verify the accuracy of the PC-RSE.

3.1 PC-RSE applied to a 1D-periodic photonic-crystal slab for TE polarisation

We now use the PC-RSE derived in Ch.2 for finding the RSs of a nonmagnetic, non-dispersive PC slab with a periodic modulation of the permittivity. In this case, the perturbation matrix in the TE polarisation simplifies to

$$V_{nn'}^{gg'} = \int E_n^g(z)\Delta\varepsilon_{g-g'}(z)E_{n'}^{g'}(z)dz \tag{3.1}$$

where

$$\Delta\varepsilon_g(z) = \frac{1}{d}\int_d \Delta\varepsilon(x,z)e^{-igx}dx \tag{3.2}$$

and $E_n^g(z)$ is the electric field (directed along y) of the homogeneous-slab RS with index n and momentum $p+g$ along x where p is the in-plane wavevector where $p=0$ corresponds to normal incidence. In general, this RS is a solution of the Maxwell wave equation (B.7) with the outgoing boundary condition Eq. (B.15) and the normalisation given by Eq. (B.16), see Appendix B. Here, we have added index g to the electric field E_n^g and the eigenfrequency ω_n^g, in order to distinguish different Bragg channels contributing to the PC-RSE.

Note that in order to treat a permittivity perturbation in the TM polarization, one should instead set $\Delta\varepsilon = 0$ in Eq. (2.24) and use $\Delta\mu$ for the modulation of the permittivity, along with replacements $iH_x \to E_x$ and $iH_z \to E_z$ in the unperturbed wave function $\boldsymbol{\mathcal{F}}_n(z;p)$.

As a basis system, we choose a homogeneous dielectric slab in vacuum, of thickness $2a$, permittivity $\epsilon > 1$, and permeability $\mu = 1$. The full permittivity profile of the slab system is given by Eq. (C.1), and the basis RSs and cut densities are provided in Appendix C. Within the slab, $|z| \leqslant a$, the electric

fields of the RSs and cut modes are described by the same functions

$$E_n^g(z) = B_n^g(e^{iq_n^g z} + (-1)^n e^{-iq_n^g z}) \tag{3.3}$$

where the field must be normalised as a consequence of the Mittag-Leffler form of Green's function:

$$2\int_{-a}^{a} \left(E_n^g(z)\right)^2 \varepsilon(z)dz - \frac{\left(E_n^g(a)\right)^2 + \left(E_n^g(-a)\right)^2}{ik_n^g} = 1\,, \tag{3.4}$$

which is derived in Appendix B.

This results in the normalisation constant, B_n which is given by:

$$\left(B_n^g\right)^{-2} = 8(-1)^n \left[\epsilon a + \frac{ip^2(\epsilon\mu - 1)}{k_n^g\left(\left(q_n^g\right)^2 - \mu^2\left(k_n^g\right)^2\right)}\right]. \tag{3.5}$$

The mode parity is determined by the parity of n via the coefficient $(-1)^n$ taking the values of $+1$ or -1. The eigenfrequencies ω_n^g are determined by the secular equation (C.7) for the RSs and by Eq. (2.28) for the cut modes. Furthermore, the link between the mode frequency ω_n^g and the wave number k_n^g in vacuum and q_n^g in the medium is provided by the following light dispersion relations:

$$(\omega_n^g)^2 = (k_n^g)^2 + (p+g)^2\,, \tag{3.6}$$

$$\epsilon(\omega_n^g)^2 = (q_n^g)^2 + (p+g)^2 \tag{3.7}$$

where it is now clear to see that there are branch cuts at $\omega = \pm(p+g)$.

Now that we defined the system parameters, we can apply the cut discretisation described in Ch. 2.3. The cut weight function is given by Eq. C.11. The artificial cut modes ω_ν are designed to be used alongside the RSs ω_n, therefore

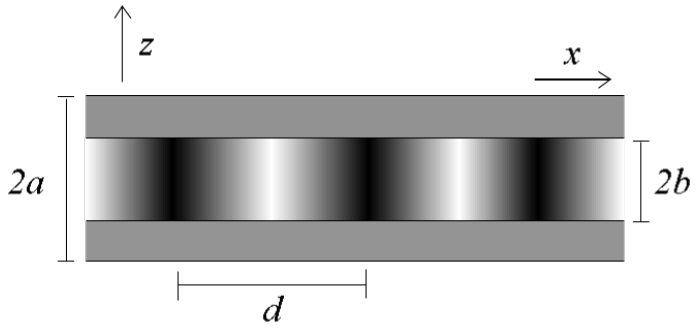

Figure 3.1: Schematic of the perturbed system – photonic crystal slab of the total thickness $2a$, periodically modulated in x direction, with period d, within the layer of thickness $2b$ at the center of the slab.

the electric fields for the cut modes have the same form as in Eq. 3.3 which can be combined using a new index $\bar{n}$:

$$E_{\bar{n}}(z) = B_{\bar{n}}(e^{iq_{\bar{n}}z} + (-1)^{\bar{n}}e^{-iq_{\bar{n}}z}), \qquad |z| \leqslant a \tag{3.8}$$

where

$$\bar{n} = \begin{cases} n & \text{for RSs} \\ \nu & \text{for cut modes} \end{cases} \tag{3.9}$$

but with a different normalisation constant:

$$B_{\bar{n}} = \begin{cases} B_n & \text{for RSs} \\ B_\nu = \sqrt{\omega_\nu C_\nu} & \text{for cut modes} \end{cases} \tag{3.10}$$

where C_ν is defined in Eq. (2.29).

Using Eq. (2.29), we can graphically show in Fig. 3.2 how these artificial cut modes compensate for the cut, comparing $\sigma_\nu(\omega)$ with $C_\nu/\Delta\omega_\nu$, where $\Delta\omega_\nu$ is roughly the distance between neighboring cut poles. We compare the cut poles

to the equation for the cut weights given by (see Appendix B):

$$\sigma_{\pm}(\omega) = \frac{1}{4\pi} \frac{\mu^2 k}{(\mu^2 k^2 - q^2)\cos(2qa) \pm (\mu^2 k^2 + q^2)} \,. \tag{3.11}$$

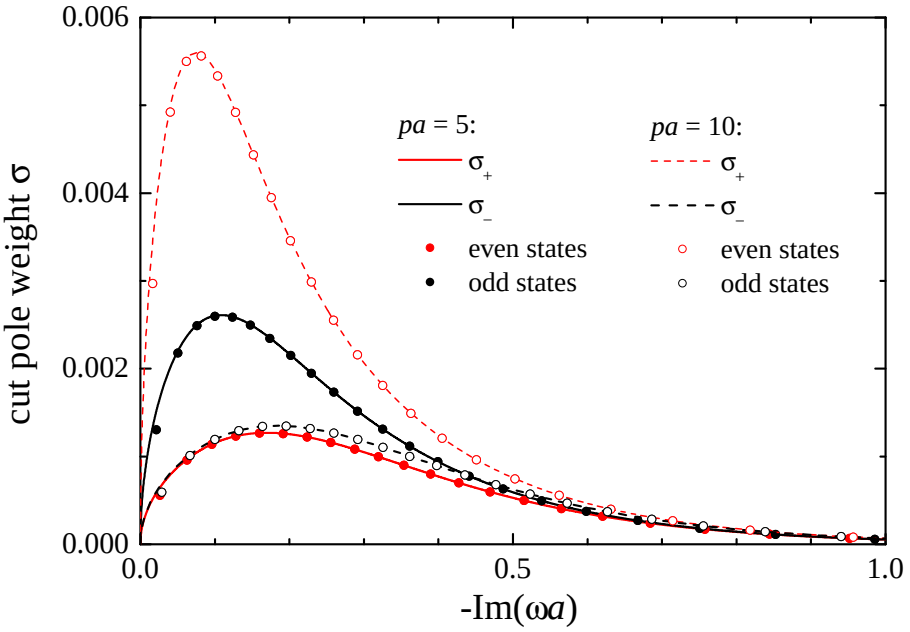

Figure 3.2: Cut weights $\sigma_{\pm}$ (solid and dashed lines) as functions of the imaginary part of the frequency along the cut, for different values of p as given, along with the discretized cut pole values $C_\nu/\Delta\omega_\nu$ (circles). Each cut parity contains 22 poles. $\varepsilon = 6$ and $d = 2\pi/5$.

3.2 Basis for the PC-RSE

The full basis for the PC-RSE consists of an infinite number of RSs and cut modes, taken for all Bragg channels $g = 2\pi m/d$, where $m = 0, \pm 1, \pm 2....$ Any periodic perturbation $\Delta\varepsilon(x, z) = \Delta\varepsilon(x + d, z)$, introduces coupling between the basis states belonging to different Bragg channels, so that in order to obtain

the exact result one needs to take all of them into account simultaneously. In practice, we introduce a truncation, limiting the number of RSs and cut modes for each Bragg channel as well the number of Bragg channels themselves. We do both truncations by introducing a single real parameter $\omega_{\max}$ which defines a circle $|\omega| < \omega_{\max}$ in the complex frequency plane containing the basis RSs and cut modes included in the PC-RSE. For a fixed ratio of the number of RSs and cut modes in the basis, the total number of modes scales as $\omega_{\max}^2$ due to the linearly increasing number of channels and the linearly increasing number of modes per channel as $\omega_{\max}$ increases which combine to create a quadratic dependence on $\omega_{\max}$. The set of included RSs, defined in this way, typically contains a large number of WG modes. In fact, only the $m = 0$ channel consists of equidistant FP modes which we call in the following *leaky modes*. All other channels contain WG modes having real frequencies ω_n^g within the intervals $(p+g)/\sqrt{\epsilon} < |\omega_n^g| < (p+g)$. The number of WG modes within each channel grows linearly with g, with the total number increasing quadratically with g. The WG modes are separated from FP modes by series of cut poles of the GF which are positioned vertically down below the branch points at $\omega = \pm(p+g)$. For $\mathrm{Re}(\omega) > p+g$ and $\mathrm{Re}(\omega) < -(p+g)$, there are two infinite series of FP modes for each Bragg channel. All this means, in particular, that for a given radius $\omega_{\max}$, the basis includes $2M+1 \approx \omega_{\max}\sqrt{\epsilon}d/\pi$ channels, most of which consist of only WG modes.

For the purpose of verification of the PC-RSE by comparing it with the scattering matrix method (SMM), which is presented in Ch. 3.5 below, we use however a different criterion: we limit the number of Bragg channels to $|m| \leqslant M$, where M is a fixed number, and truncate the RSs and cut modes independent of M, i.e. using the same number of cut modes for each selected channel. This is done in order to avoid a computationally expensive root searching within the

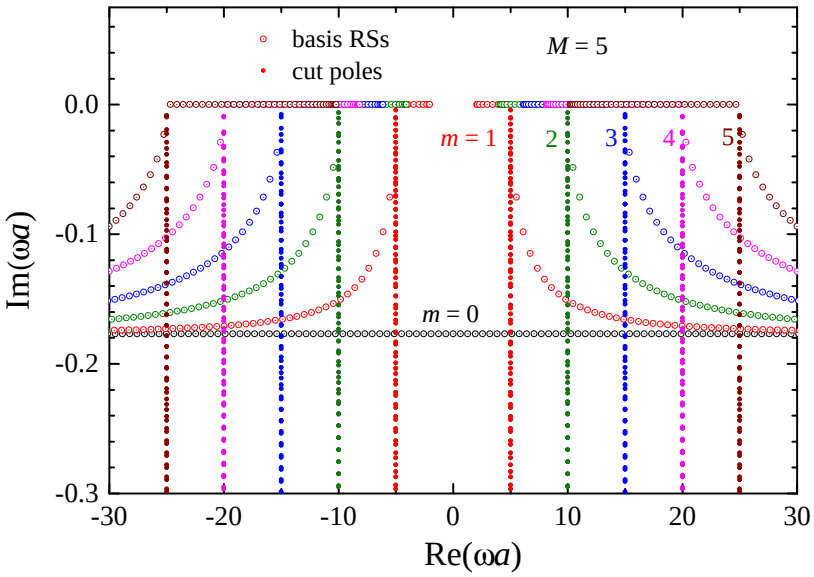

Figure 3.3: Basis RSs and cut poles (used for comparison of the PC-RSE with SMM) for $\epsilon = 6$, $\alpha = \beta = 0$, and $M = 5$ leading to 11 Bragg channels in the basis, each channel labelled with index m. The frequencies of the RS and cut modes of channels m and $-m$ are identical.

SMM related to the increase of the S-matrix size with M. Clearly, for adequate comparison, it is essential to keep the truncation number M the same for both PC-RSE and SMM. However, the necessity to keep M low demonstrates the major weakness of the SMM.

The PC-RSE basis used for the comparison with the SMM is illustrated in Fig. 3.3, for $p = 0$ and $M = 5$, showing the eigenfrequencies of both the RSs and cut modes for all selected 11 Bragg channels. Clearly, for $p = 0$, the positive- and negative-m channels are degenerate (giving the same RS eigenfrequencies), and both degenerate channels must be included in the basis. Additionally, there are now $2M$ cuts with discretized cut modes added to the basis. These cut modes are also degenerate for the same reason as the RSs.

3.3 Cosine modulation of a homogeneous slab

For illustration purposes and also for the ease of comparison with the SMM, the perturbation of the homogeneous slab is taken in the most simple harmonic form:

$$\Delta\varepsilon(x,z) = \left(\alpha + \beta\cos\frac{2\pi x}{d}\right)\Theta(b-|z|)\,, \tag{3.12}$$

where $\Theta(z)$ is the Heaviside step function, $b \leqslant a$, and α and β are some parameters (see Fig. 3.1). We note, however, that the RSE can equally deal with any other shape of the periodic perturbation, not requiring the separation of variables which the perturbation in the form of Eq. (3.12) possesses. The SMM in turn, requires this separation. In fact, the transfer matrices that form the scattering matrix are calculated layer-by-layer through the system (see [7]). Therefore any system changing smoothly in the growth direction will be approximated by a stack of slices homogeneous in z, which are ideally infinitely thin.

For the perturbation given by Eq. (3.12), the matrix elements take the following explicit form:

$$V^{gg'}_{\bar{n}\bar{n}'} = B^{g}_{\bar{n}} B^{g'}_{\bar{n}'} \left(2\alpha\delta_{gg'} + \beta X_{g-g'}\right) b Z^{gg'}_{\bar{n}\bar{n}'}\,, \tag{3.13}$$

where

$$X_g = \delta_{g,g_1} + \delta_{g,g_{-1}} \tag{3.14}$$

with $g_{\pm 1} = \pm 2\pi/d$ and

$$\begin{aligned} Z^{gg'}_{\bar{n}\bar{n}'} &= \left(1+(-1)^{\bar{n}+\bar{n}'}\right)\operatorname{sinc}\left[\left(q^{g}_{\bar{n}} + q^{g'}_{\bar{n}'}\right) b\right] && (3.15)\\ &\quad + \left((-1)^{\bar{n}} + (-1)^{\bar{n}'}\right)\operatorname{sinc}\left[\left(q^{g}_{\bar{n}} - q^{g'}_{\bar{n}'}\right) b\right] && (3.16) \end{aligned}$$

with $\operatorname{sinc} z = \sin z/z$.

For homogeneous perturbations, used in Appendix D for the RSE verification and comparison of the k- and ω representations, we use $\alpha \neq 0$ and $\beta = 0$. For all periodic perturbations we instead take $\alpha = 0$ and $\beta \neq 0$, so that all the matrix elements Eq. (3.1) within the same channel ($g = g'$) are vanishing since $\Delta\varepsilon_0(z) = 0$, according to Eq. (3.2). This property yields a quick convergence of the PC-RSE. In fact, since the diagonal elements of the perturbation matrix are all zeros, the first-order contribution of the PC-RSE is vanishing [12]. Then the lowest-order non-vanishing contribution of the perturbation can only be quadratic in $V_{nn'}^{gg'}$, making its overall effect quantitatively small and the PC-RSE converging quickly to the exact solution.

3.4 RSs of a PC slab

We now show the RSs for a PC slab calculated using Eq. (2.30). Fig. 3.4 shows the basis modes found above, as well as the PC modes and the SMM results which will be used in the next section for verification. We see significant modification of the modes when the perturbation is applied. The $m = 0$ basis modes which were previously evenly spaced and had the same imaginary part are now much more perturbed. For a low real frequency however, the $m = 0$ modes are much less affected by the perturbation. This can be explained by their distance to other modes which reduces their influence.

In the basis, oppositely signed channels e.g $m = \pm 1$ are degenerate due to the normal incidence of the system. When the perturbation is applied however this degeneracy is broken and the modes of opposite signed are combined into even and odd basis states which are perturbed differently. Of particular interest are the WG, the eigenfrequencies of which lie on the real axis. When the perturbation is applied and the degeneracy broken, the frequency of one mode within the pair remains real valued while the other gains an imaginary part.

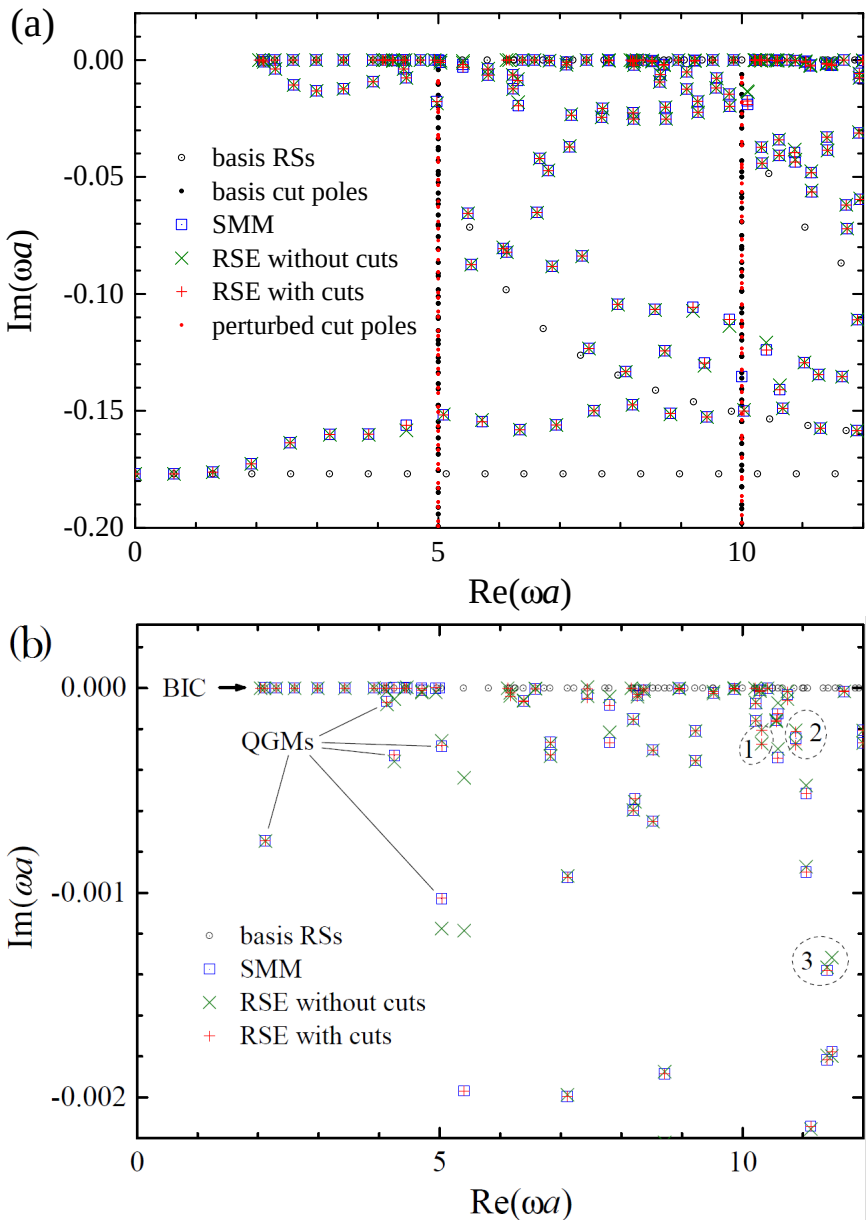

Figure 3.4: (a) RS frequencies of a PC slab with $\epsilon = 6$, $\alpha = 0$, $\beta = 1$, $b = a/2$, and $d = 2\pi a/5$, calculated for $M = 5$ using the PC-RSE ($N = 1998$, $F = 1$) with and without cut modes (red and green crosses) and the SMM (blue squared with dots). Unperturbed RSs and both unperturbed and perturbed cut modes are also shown (black circles with dots, black and blue dots, respectively). (b) Zoom of (a) showing RSs near and on the real axis.

The former is the phenomenon of the bound state in the continuum which is separated from the other modes in the spectrum which are coupled to the photonic continuum outside and are therefore leaky. The other mode in this pair are the quasiguided modes, named due to their high, but not infinite, Q-factors. These modes will be examined in more depth in later sections.

Included as part of the basis are the artificial cut modes. Since these are treated just like any other basis mode, they too produce perturbed modes. While these modes seem artificial, placed here only due to the mathematics of the branch cut, they represent real effects in the transmission spectrum called Rayleigh-Wood anomalies which are due to the opening of a new diffraction order. These perturbed cut modes positioned along the same cut lines at $\mathrm{Re}\,(\omega a) = 5$ and 10, but shifted vertically with respect to their unperturbed positions (compare red and black points). This is a remarkable property of the PC-RSE to leave the cuts unchanged but the cut weight redistributed. This allows us to find the dyadic GF of a PC system which is not possible by other means.

3.5 Verification of the PC-RSE

We now use the SMM as a proven method for finding RSs of a PCS as a verification for the RSE. We first consider a homogeneous dielectric slab in vacuum. Taking $\epsilon = 6$ and $pa = 5$ as an example, we demonstrate numerically in Appendix C a quick convergence with the basis size N of the ML series for the GF to its exact values, given by the analytic formula Eq. (C.3). We show in particular that both k- and ω-representations of the GF (the first without and the second with cuts in the basis) converge in the same way, with the absolute error scaling as $1/N^2$. The contribution of the cuts to the ML expansion in the ω-representation is taken into account in this case in a form of a numerical

integration.

We then apply in Appendix D the RSE to a uniform perturbation of the homogeneous slab for $p \neq 0$, demonstrating for both k and ω representations a quick convergence of the RSE to the analytic solution available for the core-shell geometry used, with the relative error for the wave numbers scaling as $1/N^3$. The RSE in the k representation essentially reproduces the results of [14]. However, the RSE in ω representation is applied to homogeneous systems for the first time. In this representation, the cut contribution is taken into account in the RSE in the form of a subset of artificial cut modes obtained by a numerical discretisation of the cuts and added to the basis. The procedure of the cut discretisation is described in detail in Appendix D.2. These cut modes are then used in the PC-RSE.

Now, in order to verify the PC-RSE, we consider the periodic perturbation Eq. (3.12) with $\alpha = 0$, $\beta = 1$, $d = 2a\pi/5$, and $b = a/2$. The unperturbed system is a homogeneous slab in vacuum of thickness $2a$ and permittivity $\epsilon = 6$. Its RSs and cut modes for TE polarisation and $p = 0$ are shown in Fig. 3.3. Perturbed RSs of the PC slab, calculated via the PC-RSE (with and without cut modes) and by the SMM, are shown in Fig. 3.4 along with all the unperturbed RSs and cut modes present in the displayed spectral range. As already mentioned in Sec. 3.2, the same truncation of the Bragg channels with $M = 5$ was used for both the PC-RSE and SMM.

While the periodic perturbation is not small ($\beta = 1$), leading to a considerable modification of the RSs, one can see in Fig. 3.4 a very good visual agreement between the SMM and the PC-RSE, even when no cut modes are included in the basis (green crosses $\times$). In fact, in this case, there is only a slight discrepancy between the two calculations seen for some RSs close to the cuts (see e.g. region 3 in Fig. 3.4(b)). These discrepancies are fully removed when cut modes

are included in the PC-RSE (red crosses +).

To quantify the agreement between the PC-RSE and SMM we study the relative error for the RS frequencies, which is shown in Fig. 3.5(a). Increasing the basis size N, the error does not improve for some RSs near the cuts, if the cut modes are not included in the basis. Including the cuts, the relative error gradually decreases for all RSs, as the basis size grows. Interestingly, the cut modes do not contribute to all the RSs evenly, and some RSs close to the cuts show rather small errors, which do not improve much when the cut modes are included.

We also show in Fig. 3.5(b) the relative error of the PC-RSE with respect to itself for a larger basis size, using the single truncation parameter $\omega_{\max}$, as described in Sec. 3.2. We take in particular the eigenfrequencies calculated for the total basis size of $N_{\rm tot} \approx 12000$ as the "exact" values in finding the errors shown in Fig. 3.5(b) for different basis sizes. Here $N_{\rm tot} = N + FN$, where N and FN are, respectively, the number of RSs and cut modes in the basis. We study the dependence on F of the relative error in Appendix D.2 (see Fig. D.2(c)) and show that $F \approx 1$ presents an optimal value for determining the RSs within a rather wide spectral range. This value of F is thus used in the calculations presented in this section.

Looking at the dependence of the error on the basis size, presented in Fig. 3.5(b), we see that the error decreases by roughly an order as the basis size doubles, which is close to the $1/N^3$ dependence observed for effective 1D systems treated by the RSE [10, 12, 13]. This demonstrates a high efficiency of the PC-RSE. In fact, its slowest element is matrix diagonalisation for which the compute time scales as N^3. More important is however the overall level of errors: Even for 26 RSs and no cut modes in the basis, the perturbed RSs of the PC slab are calculated with the accuracy of about or less than 10^{-3}. The

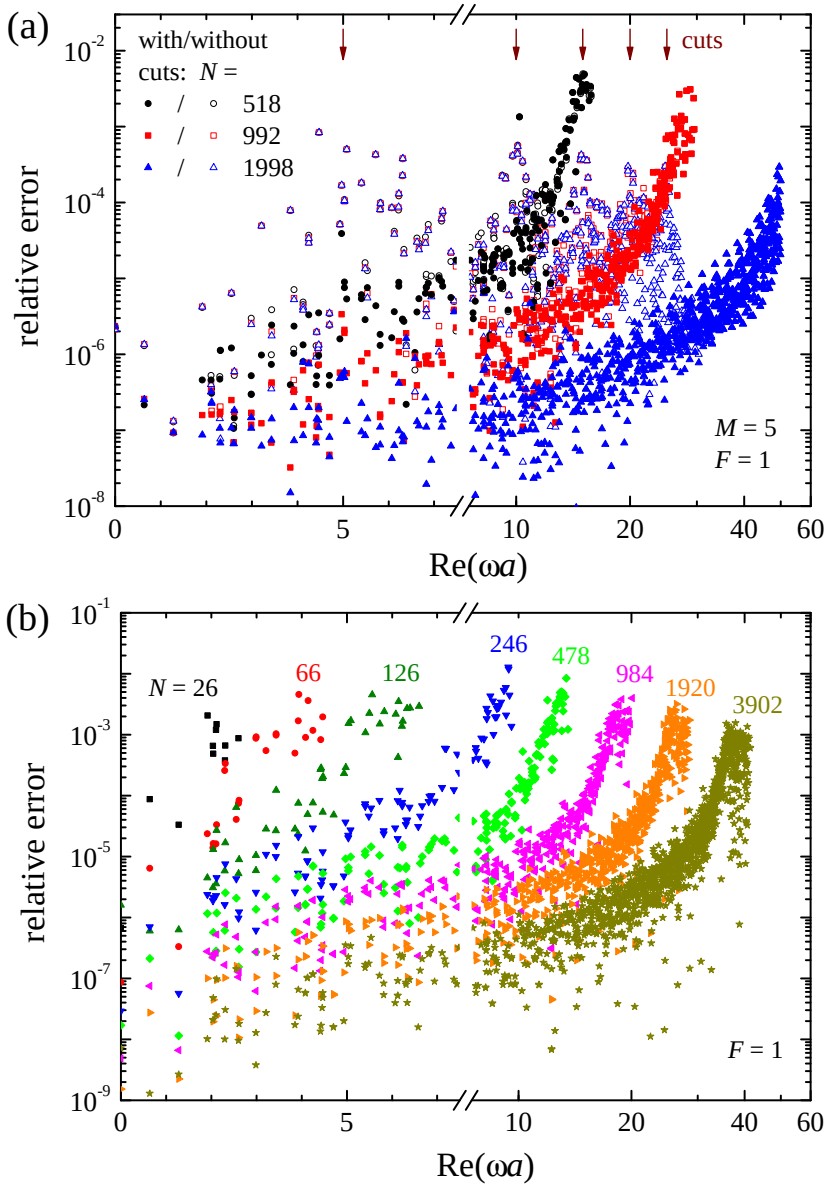

Figure 3.5: (a) Relative error of the PC-RSE compared to the SMM result, taking the latter as "exact", calculated with and without cut modes, for different basis sized as labeled, $F = 1$, and parameters of the PC slab as in Fig. 3.4. The basis consists of the closest to the origin modes, with the same number of modes for each Bragg channel, for $M = 5$. (b) Relative error of the PC-RSE using the $N \approx 6000$ result as "exact", for the same PC slab and the basis size as labeled. The basis consists of all RSs and cut modes within the circle $|\omega| < \omega_{\max}$ in the complex frequency plane. $\varepsilon = 6$, $\beta = 1$, $d = 2\pi/5$ and $b = 0.5a$.

same level of errors is seen in Fig. 3.5(a) when cut modes are not taken into account, for a large number of RSs found within a much wider spectral range. This can be understood by the already mentioned fact that all diagonal elements $V^{gg}_{\bar{n}\bar{n}} = 0$, leading to the effect of the perturbation vanishing in first-order, and therefore to a rather low level of corrections and errors.

A large number of the RSs shown in Fig. 3.4(a) seem to have the imaginary part of the eigenfrequency close to zero. To see this more clearly, we zoom in the view of the imaginary part in Fig. 3.4(b) by a factor of 100. This allows us to distinguish two types of modes. The first type is known as bound states in the continuum (BICs), which can be further split into accidental BICs (A-BICs) and symmetry protected BICs (S-BICs), which are discussed in Ch. 5. These modes, much like WG modes in a planar waveguide, have strictly zero imaginary part and therefore infinite Q factor or lifetime. However, unlike the WG modes, BICs lie in the spectral range where they could (but in reality do not) communicate with the photonic continuum outside of the system. The second type we call quasiguided modes (QGMs) [7] which usually have a very small but nonzero imaginary part of the eigenfrequency (high Q factor), as compared to e.g. FP modes. This is again due to the dominant role of the WG modes in their formation, like for the BIC, while the small imaginary part is caused by the coupling between the WG and leaky modes, see Ch. 4 below for a more detailed analysis of both types of RSs.

We also see in Fig. 3.4(b) some failures of the SMM, showcasing the superiority of the RSE method. The SMM ultimately relies on the Newton-Raphson method of finding the poles of the S-matrix [7, 61]. This means that it uses a small but finite tolerance playing the role of the parameter. If the mode splitting is below the tolerance level, the SMM is unable to resolve them, such as in region 2 of Fig. 3.4(b). Reducing the tolerance can fix this issue, however,

with a potential to generate at the same time spurious solution at another place, such as in region 1 of Fig. 3.4(b). The RSE in turn does not require a tolerance and returns the correct number of RSs in a selected region, neither missing any modes nor producing any spurious solutions. This is an important and unique property of the RSE, following from the completeness of the basis used. Owing to its linearity in ω, the RSE always returns as output a set of perturbed modes which is also complete. Furthermore, the number of perturbed modes is always equal to the number of basis modes used.

3.6 Non-normal incidence

Until now, the in-plane wavevector p was always set to 0, corresponding to a normal incidence electric field exciting the system. However, we have been careful to derive all equations for any value of p and so non-normal incidence requires no further changes to the formulation. The only complication is that there are now no longer degenerate modes which were previously arising from opposite signed values of g which are identical since only g^2 appears in the equations for k. However, with non-zero p the values of $(p+g)^2$ and $(p-g)^2$ are now different for the same value of g and the degeneracy is lifted. This also means that the positive and negative channels open at different frequencies and so the cuts are also no longer degenerate.

The $m = 0$ channel has now also gained a cut at $\mathrm{Re}(\omega a) = 3$ and so there is no longer a channel that is open for all frequencies which will have consequences for the formation of BICs, discussed later in Ch. 5. In fact, we can see in Fig. 3.6(a) that there are three WG modes below the frequency of the first cut (which belongs to the $m = -1$ channel at $\mathrm{Re}(\omega a) = 2$). These all belong to the $m = 0$ channel with the $m = -1$ channel containing no WG modes at all.

The first three $m = 0$ channel WG mode frequencies remain real when the

perturbation is applied. These would appear to be BICs, but in this case these modes exist below the opening of any channels. In the normal incidence case, the $m = 0$ channel was open at all frequencies which provided a pathway to the outside for all modes, those that did not become leaky in the presence of these modes when the perturbation was applied were then labelled BICs since there must be some mechanism separating them from the continuum. In the non-normal incidence case however, the $m = 0$ channel is not open at all frequencies and those modes that lie below the opening of this channel are intrinsically separated from the continuum and thus are not labelled BICs but are instead WG modes.

Fig. 3.6(b) shows the relative error of the RSE method for various basis sizes when compared to a much larger basis ($N = 3268$) just like Fig. 3.5. The RSE converges at the same rate as normal incidence showing the flexibility of the RSE method. Note the remarkable accuracy (10^{-3}) attained for a very small basis size of $N = 6$.

3.7 Other parameters of the system

We finally study the dependence of the RS frequencies calculated via the PC-RSE and their errors on the two structural parameters of the PC slab: the half-width of the core layer b and the period of modulation d, while keeping $\epsilon = 6$, $\alpha = 0$, $\beta = 1$, and $p = 0$ as before.

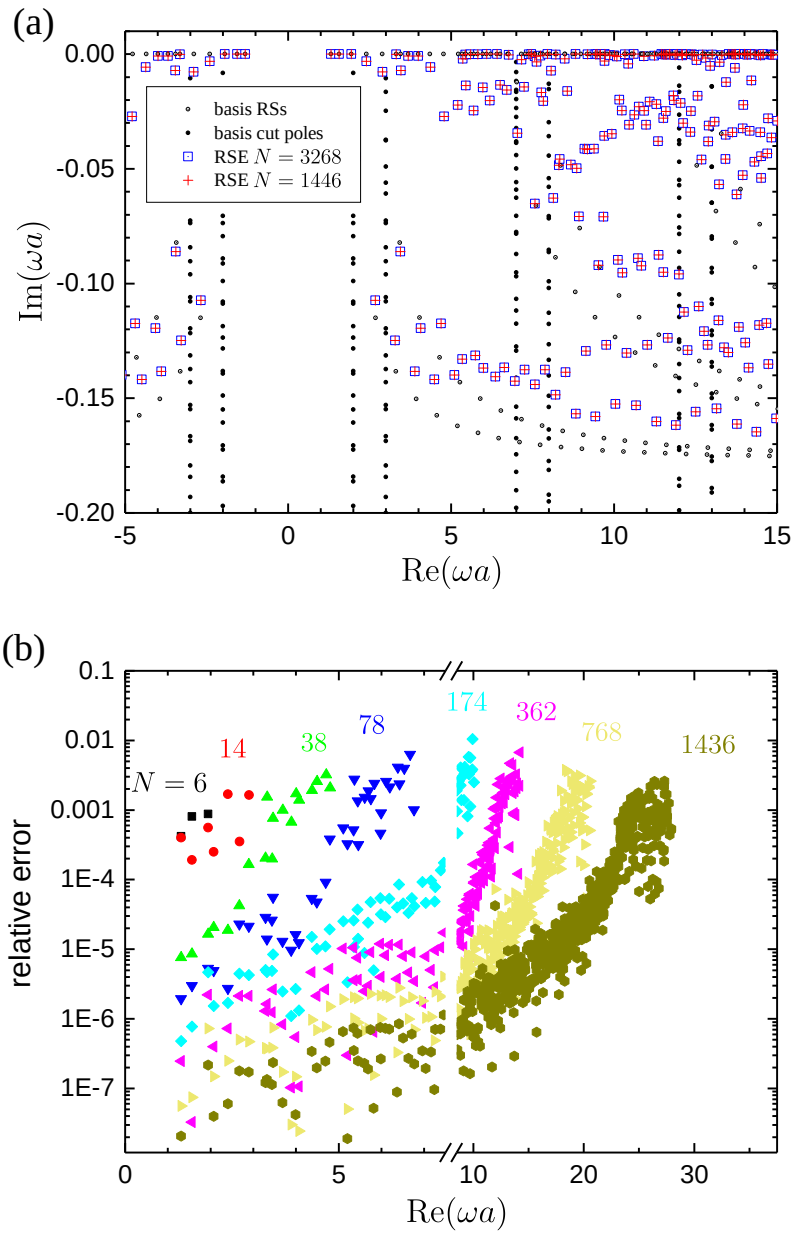

Figure 3.6: (a) RSE results with the same parameters as in Fig. 3.4 but with $p = 3$, shown are the RSE results for two different basis sizes for comparison. (b) the relative error of the RSE for different basis sizes compared to the basis size $N = 3268$ shown in (a).

Increasing b from half-width ($b = a/2$) to the full-width value ($b = a$) does not lead to any significant changes in the spectrum, as one can see in Fig. 3.7(a). The relative error is however getting sensitive to b as $b \to a$. In fact, the error in Fig. 3.7(b) shows that the case of $b = 0.95a$ can produce up to an order of magnitude higher errors (relative to the SMM) compared to the system with $b = 0.5a$. The reason for this increase is related to the ML series changing its convergence properties on the borders of the system, which requires a further study. Presently, it prevents the PC-RSE from being used with exactly $b = a$.

Figures 3.8 and 3.9 show the RS frequencies and the relative error for the period of modulation d, respectively, 5 times smaller and 5 time larger than that used for Fig. 3.4 ($d_0 = 2\pi a/5$). Such changes to the period modify the spectrum of the RSs dramatically, so for instance, in the first case the number of RSs per cut is much larger than in Fig. 3.4 and in the second case – much smaller. Nevertheless, the PC-RSE is working equally well in all these cases, as we can see from almost the same level of errors.

3.8 Other Periodic Perturbations

So far, we have only considered the perturbation of the permittivity to be a cosine wave. This is the simplest case for a photonic crystal, however the RSE can handle more complex perturbations. As it was derived in Ch.2, the RSE can handle any perturbation which can be described by a Fourier series. The only modification to the RSE is the $\Delta\varepsilon_{g-g'}$ term in 3.1, all other terms remain identical to the cosine perturbation described so far. This demonstrates the flexibility of the RSE since any change to the perturbation would require an entirely new calculation in other methods but we are able to use the same basis system for multiple perturbations.

Here, we show the case for a square wave perturbation which is a much more

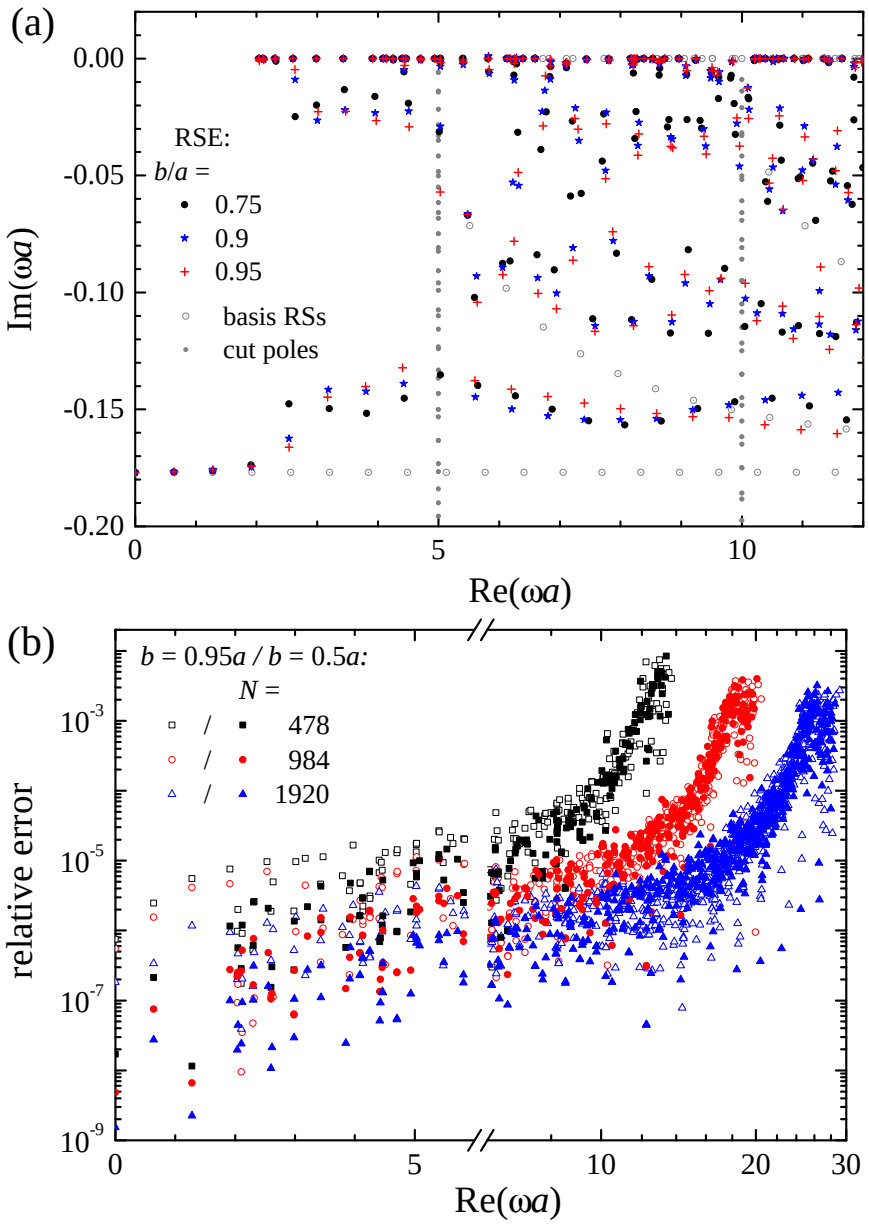

Figure 3.7: (a) RS frequencies of a PC slab with $\epsilon = 6$, $\alpha = 0$, $\beta = 1$, $d = 2\pi a/5$, and $p = 0$, calculated for $F = 1$ and $M = 5$ via the PC-RSE for different values of b as given. Unperturbed RSs and cut modes are also shown (black circles with dots and black dots, respectively). (b) Relative error of the PC-RSE compared to the SMM result, taking the latter as "exact", calculated for different values of b and different basis sizes N as given.

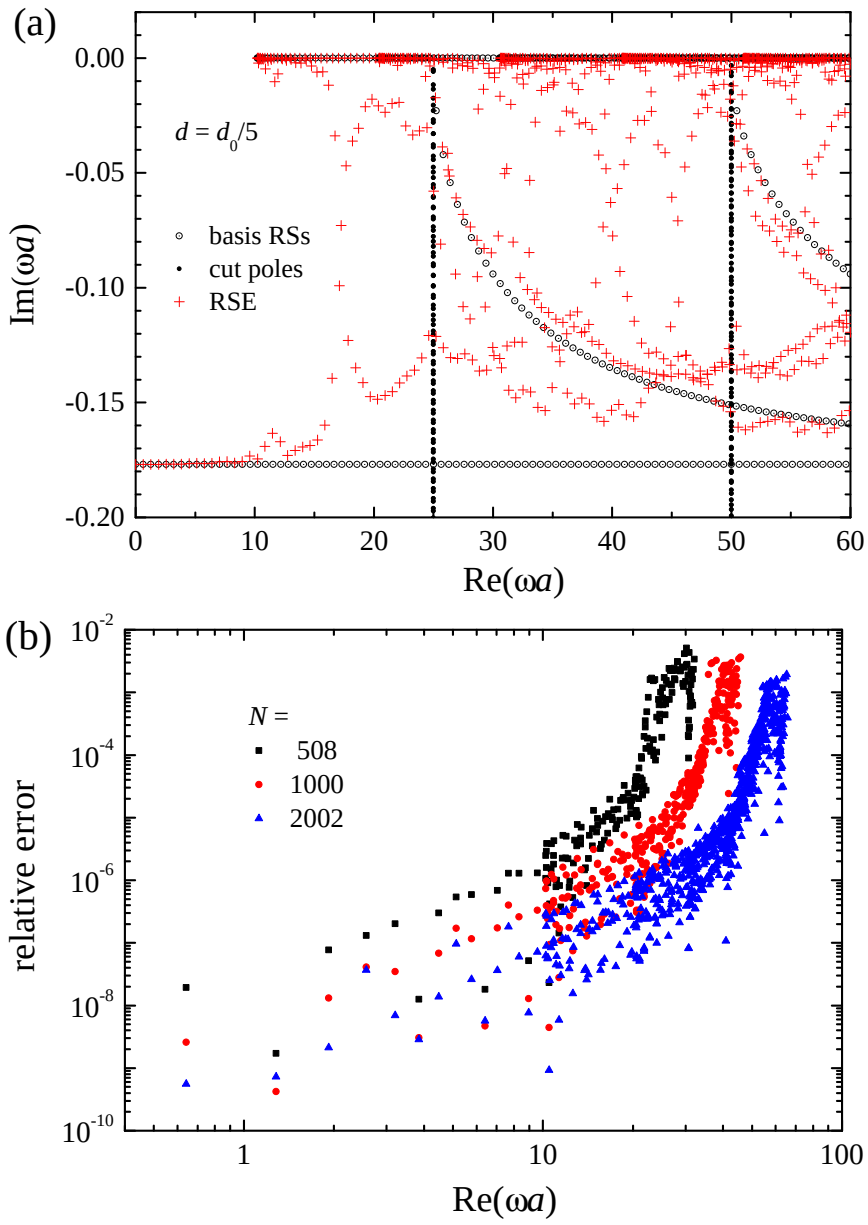

Figure 3.8: (a) RS frequencies of a PC slab with $\epsilon = 6$, $\alpha = 0$, $\beta = 1$, $d_0 = 2\pi a/25$, and $p = 0$, calculated for $F = 1$ via the PC-RSE (red crosses). Unperturbed RSs and cut modes are also shown (black circles with dots and black dots, respectively). (b) Relative error of the PC-RSE compared to the RSE with $N \approx 4000$, taking the latter as "exact", calculated for different basis sizes as given.

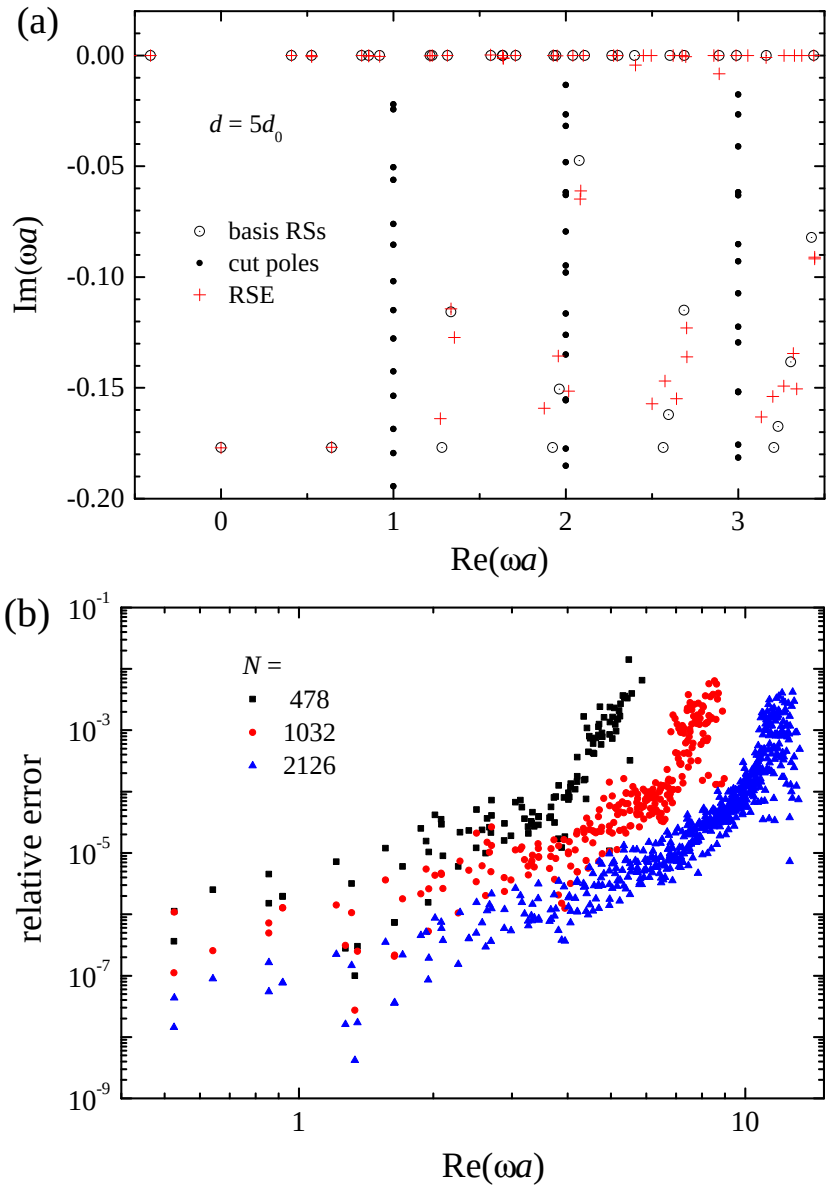

Figure 3.9: As Fig. 3.8 but for $d = 2\pi a$.

realistic system compared to a cosine wave. The square wave is given by the Fourier series:

$$\Delta\varepsilon(x) = \beta\frac{4}{\pi}\sum_{n=1,3,5\ldots}^{\infty}\frac{1}{n}\sin\left(\frac{n\pi x}{d}\right) \tag{3.17}$$

where β is behaving as a perturbation strength parameter like with the cosine perturbation.

Such a perturbation would obviously require an infinite amount of Fourier terms to describe which is not possible to consider. The amount of Fourier terms will be truncated to a finite amount. The exact number of terms considered depends on the number of Bragg harmonics considered in the basis system since the Fourier terms would need to fit inside the perturbation matrix, $V_{nn'}^{gg'}$. This was already discussed in the cosine perturbation section, where we consider all Bragg harmonics within a circle in the frequency plane $|\omega| < \omega_{max}$. Thus, the accuracy of the Fourier series is controlled by the parameter ω_{max}. Fig. 3.10 shows the RSs eigenfrequencies for a square wave perturbation as calculated by the PC-RSE and the relative error for various basis sizes compared to the PC-RSE with a large basis size.

The RSs eigenfrequencies are similar to those of the cosine wave perturbation. This is to be expected since most of the parameters (basis permittivity, perturbation period, perturbation strength etc.) are the same and also the basis is the same. The square wave perturbation still supports BICs and quasi-BICs. The PC-RSE performs exactly the same as with a cosine perturbation, still demonstrating a $1/N^3$ convergence where N is the number of basis modes.

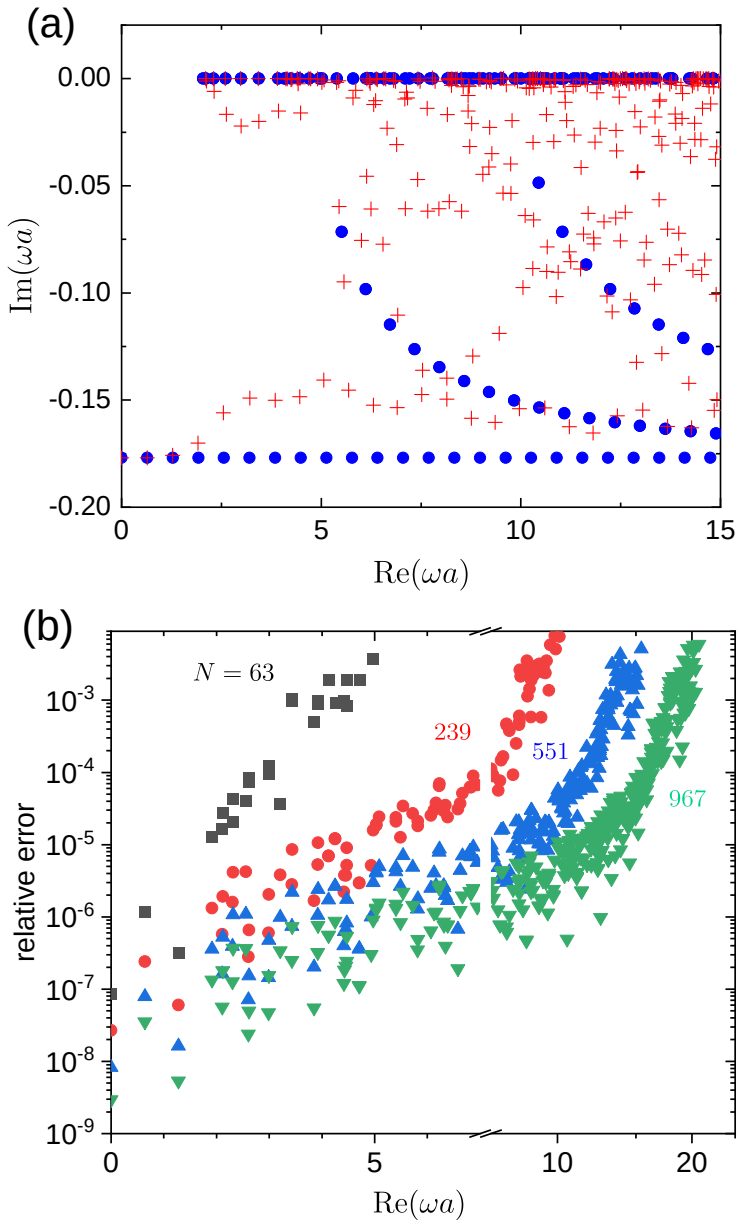

Figure 3.10: (a) Basis states (blue circles) and resonant states for a photonic crystal with a square wave perturbation. (b) Relative error of the RSE for different basis sizes for a square wave perturbation for $\varepsilon = 6$, $\beta = 1$, $a = 1$, $b = 0.5$ and $d = 2\pi/5$.

3.9 Conclusion

In this chapter, we applied the general form of the PC-RSE equation derived in Ch.2 to a specific system. This was initially a homogeneous dielectric slab with a cosine perturbation to it's permittivity.

The basis states are found by solving a simple secular equation. Due to the photonic crystal system coupling all Bragg harmonics, the basis resonant states must be found for all corresponding in-plane wavevectors given by $g = 2\pi m/d$ where $m = 0, \pm 1, \pm 2....$ The number of Bragg harmonics considers is truncated due to finite computer space. Initially, this was truncated to a number which was chosen to match the number used in the scattering matrix method which was used as an established method with which to compare the results of the RSE. After the accuracy was demonstrated and the PC-RSE verified versus the SMM, we then used the more natural truncation of defining a circle in frequency space within which all modes and Bragg harmonics are included thus controlling the number of Bragg harmonics and resonant states in the basis with a single parameter.

We showed that the RSE converges to the correct solution as the number of basis modes, N, increases and that the error scaled as $1/N^3$ demonstrating a quick convergence. The overall level of error is also remarkably low at $< 10^{-3}$ even for small basis sizes or when the cuts are not included. This is revealed to be due to the choice of perturbation which does not have a first-order effect on the system making the overall perturbation mathematically small despite the large physical change. We show the photonic crystal eigenfrequencies calculated by the RSE which include the peculiar bound states in the continuum. These are states which have somehow become separated from the photonic continuum outside the system despite being coupled to modes which radiate into this continuum.

We then show the same system but for non-normal incidence. The equations for the RSE were derived for any angle of incidence and so this is a fairly straight forward step. Non-normal incidence breaks the degeneracy of the Bragg harmonics and causes all symmetry-protected bound states in the continuum to disappear as well as transforming some Fabry-Perot modes from the $m = 0$ channel into waveguide modes which remain waveguide modes even within the photonic crystal.

For completeness, we show some other values of the perturbation width and period, once again demonstrating the convergence of the RSE with increasing basis size.

Finally, we show the RSE for a more complex perturbation to the permittivity, replacing the cosine wave with a square wave which is a simple change for the RSE, the only difference is that the perturbation matrix is less sparse than with a cosine perturbation. We show that the convergence remains unchanged compared to the other examples.

Chapter 4

Origin and evolution of the RSs in a PC slab

In the previous chapter, we showed that the RSE is a reliable and accurate method for calculating the RSs of a PC slab. In this chapter, we use the RSE to reveal more information about the PC RSs such as their origin in the basis system and their evolution through parameter changes. This information is difficult to acquire through other methods due to excessive computation time they require and because they do not treat the system as a perturbation, i.e they do not allow us to trace the evolution of mode with parameter changes.

4.1 Evolution of modes

We use the high efficiency and accuracy of the PC-RSE to find the complete set of the RSs of a PC structure and study the origin, formation and further evolution of the RSs in a PC slab with change of the system parameters. Here we change the most important parameter: the amplitude of the periodic modulation

β. We have already shown in Sec. 3.7 results for varying the thickness of the modulation layer $2b$ and its period d.

Figure 4.1 shows the evolution of the RSs eigenfrequencies with increase of the amplitude β of the periodic modulation, which we call the perturbation strength. In the $p = 0$ case treated here, all unperturbed RSs (and cut modes) except $m = 0$ channel are doubly degenerate, as discussed in Ch. 3.2. The periodic modulation lifts this degeneracy, which is well seen in the figure. Furthermore, leaky and FP modes shift upward, increasing their Q-factors, while the majority of the RSs originating from WG modes are moving down, away from the real axis, in this way having their Q-factors reduced with β. Overall, this picture demonstrates a complicated mixing of basis modes with both infinite and finite Q-factors.

Of particular interest are RSs found close to the real axis of ω. As mentioned in Ch 3.5 above, perturbing the WG modes results in two types of RSs: BICs and QGMs. A closer look provided in Fig. 4.1(b-d) shows however that BICs are formed only within the region $-2\pi/d < \mathrm{Re}\,\omega < 2\pi/d$, bound by the cuts of the $m = \pm 1$ Bragg channels. Figure 4.1(b) demonstrates that each pair of WG modes within this region produces one BIC and one QGM, the latter loosing its quality very quickly with the perturbation strength. Outside this region we see instead that the RSs originating from the WG modes of the homogeneous slab have either Q-factors also quickly decreasing with β or very high Q-factors weakly depending on the strength of periodic modulation. The latter can be called quasi-BICs, the term which has recently become widely used in the literature for such modes [62, 63]. It is also interesting to see a formation of some of the RSs as a result of a rather strong coupling between WG modes which are close in frequency but belong to different Bragg channels, see e.g in Fig. 4.1(b) (Fig. 4.1(d)) the mode repulsion due to the coupling between WG

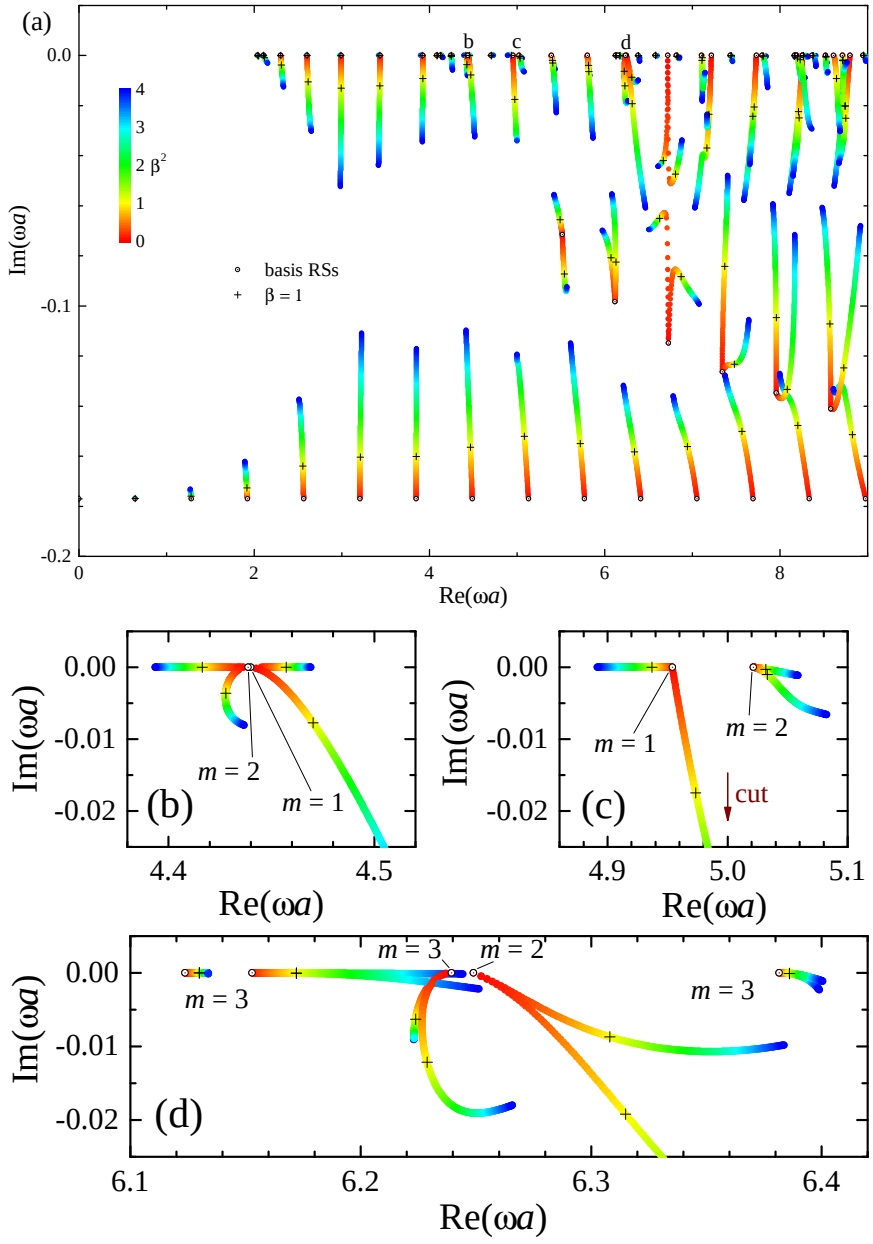

Figure 4.1: Evolution of the RS eigenfrequencies of a PC slab for the amplitude of the period modulation changing from $\beta = 0$ to $\beta = 2$ as given by the colour code. Black dotted circles represent the unperturbed modes ($\beta = 0$) and the black crosses the modes shown in Fig. 3.4 ($\beta = 1$). (b-d) Zoom-in of particular regions in the complex frequency plane close to the real axis, with the values of m indicating the Bragg order of the unperturbed modes. $\varepsilon = 6$, $b = 0.5a$, $d = 2\pi/5$.

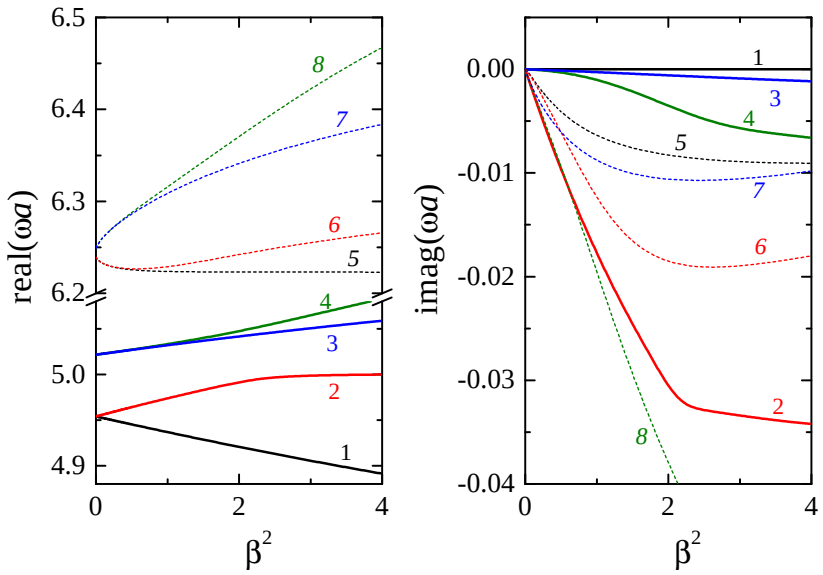

Figure 4.2: The real and imaginary parts of the modes shown in Fig 4.1(c) and four central modes in Fig 4.1(d) as function of the permittivity modulation amplitude squared, β^2.

modes of $m = 2$ and $m = 1$ ($m = 3$ and $m = 2$) channels.

As already discussed in Ch. 3, the perturbation does not contribute in first-order (for $\alpha = 0$), and thus the RSs eigenfrequencies change $\propto \beta^2$ for small β, in accordance with Eq. (38) of [12], see Fig. 4.2. However, in the case of the above mentioned strong coupling between the channels, this linear in β^2 regime takes place only at very low values of β, see e.g modes 5-8 in Fig. 4.2. Another interesting feature well seen in Fig. 4.2 is that the degenerate pair of basis WG modes producing a BIC-QGM pair (modes 1 and 2) shows a linear in β^2 splitting, while any other pair of states, not containing BICs, remains degenerate in this order. This makes BICs even more peculiar.

4.2 Contribution of basis modes

To understand this and some other properties of BICs, we look at the basis mode contribution to different RSs. We show in Fig. 4.3 the mode contribution to the BIC-QGM pair selected close to the cut of the first Bragg channel. Other types of modes – FP, leaky and cut modes – are considered in Appendix E. The size of each circle represents how much that mode contributes, with the circle area proportional to $\sqrt{|c_n^g|}$, chosen (instead of the natural $|c_n^g|^2$) in order to demonstrate more clearly the role of different basis modes. We see that all the basis RSs and cut modes of the given parity contribute to these states, even though the relevant WG mode has the dominant and indeed very large contribution to both states. It becomes also clear that the main difference between the BIC and the QGM in the studied pair is that the leaky modes of the 0th Bragg channel do not contribute to the BIC. This confirms that the BICs found in this system are symmetry-protected [43, 48, 64, 65].

In fact, owing to the symmetry of the system, the BIC shown in Fig. 4.3(a) has a wave function which is odd in the x direction and thus does not couple to the $m = 0$ channel containing only even states. In other words, the $m = 0$ channel is not present in the subgroup of odd states, and therefore this BIC is not even falling into the continuum: for this subgroup, the continuum starts at the cut positions of the $m = \pm 1$ channels. Furthermore, all doubly degenerate basis states contribute to the QGM (BIC) with the same (opposite) amplitude, $c_n^g = \pm c_n^{-g}$, also reflecting selection by symmetry.

Note that the other mirror symmetry of the system, which is in the z-direction, also results in the formation of the basis and perturbed RSs of even and odd parity. It is clear, for example, that every other FP mode does not contribute to the states in Fig. 4.3. Indeed, modes of the opposite parity in z do not couple to each other, and both the QGM and BIC shown in Fig. 4.3 are

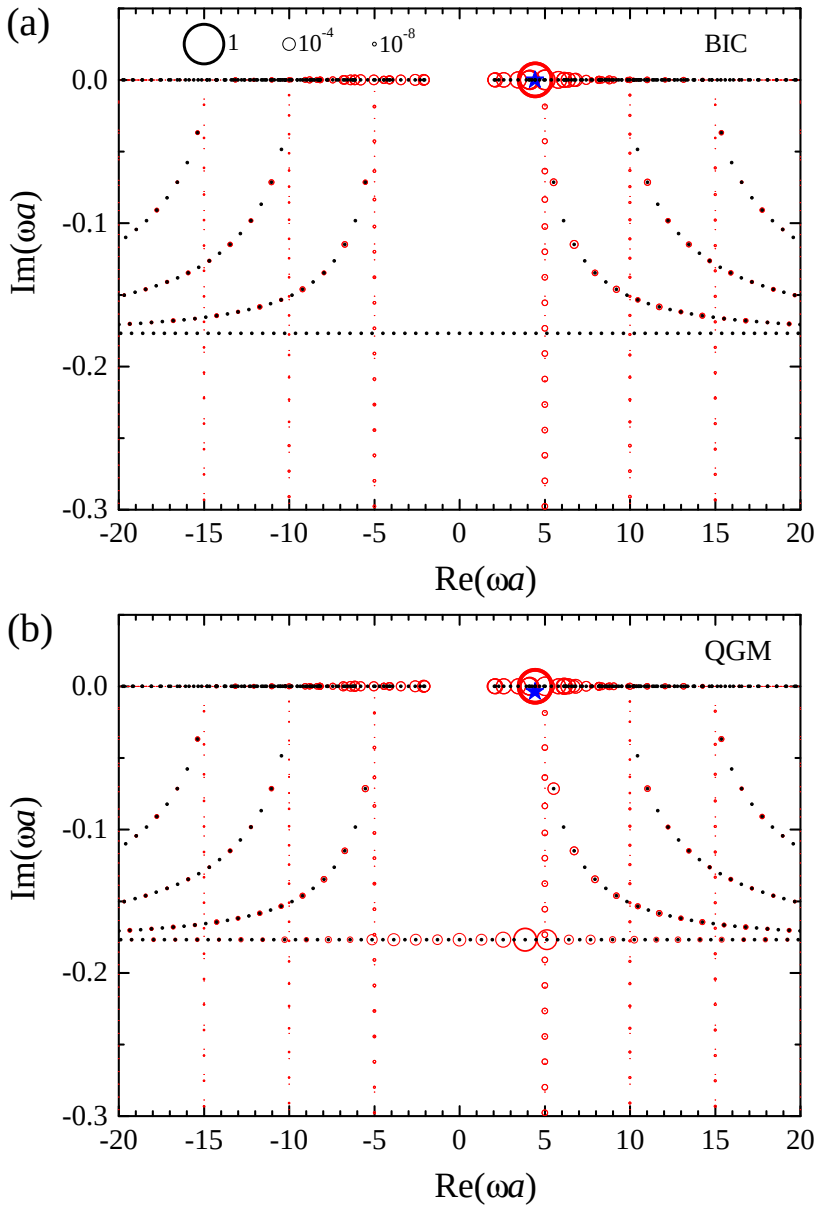

Figure 4.3: Basis mode contribution to (a) bound state in the continuum and (b) quasi-guided mode, a pair of modes originating from $m = 1$ WG mode and shown by black crosses in Fig. 4.1(c). The area of each circle is proportional to $\sqrt{|c_n^g|}$. A key showing the relationship between the circle area and $|c_n^g|^2$ is given as black circles. $\varepsilon = 6$, $b = 0.5a$, $d = 2\pi/5$, $\beta = 1$.

of even parity. This implies in particular that the basis size can be halved for this kind of perturbation.

It is also clear from Fig. 4.3 that the cut modes contribute very little to the perturbed BIC and QGM but are nonetheless required for accuracy. We have seen, in particular, that including even one cut mode, representing the full cut, is far better than not including any cut modes, despite the cut being very badly approximated.

Finally, the observed splitting $\propto \beta^2$ within the BIC-QGM pair can be understood as a result of the leaky modes of the $m = 0$ Bragg channel affecting (not affecting) the QGM (BIC). If this channel contributes, the effect of the leaky modes appears already in the 2nd order in the perturbation β, and thus causes the splitting of the BIC and QGM in this order.

The studied systems can also support non-symmetry protected BICs which are studied further in Ch. 5. These kinds of BICs can form in these systems by tuning their spatial and material parameters, such as the period and strength of the periodic modulation, and the thickness of the substrate layer (see e.g. [49]).

4.3 Conclusion

In this chapter we focused on the physical significance and qualitative understanding of the results of the previous chapter. We took advantage of the low computational cost of the RSE method to find the path that modes move through in frequency space as the permittivity contrast is increased. This revealed, in particular, the nature of the bound states in the continuum which are entirely real in frequency space. Fig. 4.1 illustrated the difference in evolution with the permittivity strength β between symmetry-protected BICs whose eigenfrequencies remained real for all values of β and the accidental BICs which are only real for one particular value of β.

Figure 4.2 showed that there was no first order contribution of the perturbation since the mode eigenfrequencies shift linearly with β^2 for small β. This was a consequence of the chosen perturbation which did not include a homogeneous part i.e $\alpha = 0$. This figure also demonstrated the degeneracy of all pairs of modes in β^2 order except for the BIC-QGM pair due to the QGM coupling to a leaky channel and the BIC remaining separated from the leaky channels.

We then showed how each mode in the basis contributes to a particular PC mode. This was possible due to the fact that the RSE treats the PC system as perturbation to the basis system. We focussed on a BIC and QGM which originate from the same degenerate pair of WG modes. We showed that the most significant difference between the two modes is that the BIC has no contribution from the $m = 0$ channel unlike the QGM. This was due to the fact that the $m = 0$ channel contains only even-in-x modes which completely decouple from the odd-in-x BIC, therefore the observed BICs are symmetry-protected.

Chapter 5

Bound states in the continuum in photonic crystals

Much like in the last chapter, we use the advantages of the RSE to study the origin of modes and their evolution with paramter changes, such as the thickness of the periodic layer and its permittivity contrast. However, in this chapter we focus on bound states in the continuum and what separates them from the other modes in the spectrum. This allows us to reveal the role of different basis states of the homogenous dielectric slab in the formation of the eigenmodes of the PC slab and to demonstrate the importance of the basis guided modes in the formation of BICs.

We will also separate the cases of symmetry-protected and accidental bound states in the continuum which is something that is not very well defined in the literature.

5.1 Symmetry protected and accidental BICs

There are two main mechanisms by which BICs are disconnected from the radiation continuum: by virtue of symmetry and by the tuning of parameters such that the radiation from all radiating channels is suppressed. These are known as symmetry-protected (S-BICs) and accidental BICS (A-BICs), respectively [43, 64, 83]. In a system that exhibits one or more symmetries, the modes of different symmetry classes completely decouple. This causes the two symmetry classes to have different radiative threshold frequencies so that a mode from one symmetry class remains as a guided mode while lying within the continuum of the other symmetry class and in this way forms an S-BIC. Although these are called BICs in the literature, they are akin to the guided modes in a homogeneous system, since they are separated in frequency from the radiation continuum onset.

A-BICS, however, are not dependent on the symmetry of the system but are instead sensitive to its spatial and geometric parameters. Unlike S-BICS, these modes are decoupled from the continuum by destructive interference occurring at the edges of the system which cancel any outgoing, travelling solutions. In PC systems, in particular, it is only necessary for the influence of radiating Bragg channels to be cancelled in this way for an A-BIC to form. This cancellation of electric fields at the edges of the system is similar to that observed for BICs in an open Sinai billiard [85], a non-periodic system which nevertheless shares some physical properties with a PC slab, see a more detailed discussion at the end of Sec. 5.3 below.

To distinguish between A-BICs and S-BICs in practice, a standard approach in the literature is by breaking the symmetry of the system which ensures that all S-BICs disappear from the spectrum of the RSs. In PC systems this is done by simply allowing a non-vanishing in-plane component of the wave number,

equivalent to a non-normal incidence of light [43, 83]. In this chapter, based on the resonant-state expansion (RSE), we will not only distinguish between A-BICs and S-BICs without breaking the symmetry, but also formulate mathematical criteria for the different types of BICs.

Interestingly, the role of different basis states of a homogeneous slab in the formation of BICs in PC structures has been very recently studied within a simple coupled-wave model [65], reducing the basis to only a few propagating waveguide modes, coupled via diffraction grating, and neglecting any evanescent channels. Compared to this model, the RSE takes into account all possible channels and basis modes within each channel, striving towards the exact solution. Another most recent paper [82] studying BICs in PC slabs uses instead the modes of an infinite PC as basis for treating a finite PC slab. The semi-analytic model developed in that paper also neglect any evanescent solutions and in practice presents a reduced approximate version of the rigourous scattering-matrix method [6, 7].

5.2 RS fields of a PC slab calculated by the RSE

The electric field of the basis system is given by Eq. (3.8) and in the full space by Eq. (C.8). Since the RSE treats the RSs of the perturbed system as a sum of the RSs of the basis, we can also construct the perturbed electric field the same way. The electric field of a perturbed RS (or a perturbed cut mode) is then given by $\mathbf{E}(x,z,t) = \mathbf{e}_y E(x,z) e^{i(px-\omega t)}$, where

$$E(x,z) = \sum_{g\bar{n}} c^g_{\bar{n}} E^g_{\bar{n}}(z) e^{igx} \quad \text{for} \quad |z| \leqslant a \tag{5.1}$$

is the corresponding scalar wave function *within* the basis system. We see that the perturbed wave function $E(x,z)$ is expressed in Eq. (5.1) as a superposition

of the basis modes $E^g_{\bar{n}}(z)$ combined with plane waves e^{igx} of the Bragg channels, with the expansion coefficients $c^g_{\bar{n}}$ and the eigenfrequency ω being a solution of Eq. (2.30).

Although the basis RSs are defined by Eq. (C.8) both within and outside the basis slab, the expansion Eq. (5.1) for a perturbed mode is valid only within the bounds of the basis system, i.e. for $|z| \leqslant a$. To find the electric field of the perturbed mode outside the basis system, we can use the homogeneity of the outside medium, which allows us to find an explicit analytic solution in terms of plane waves. This solution is exactly matching the field Eq. (5.1) on the surface of the basis system, i.e. at $z = \pm a$. We therefore find the field *outside* the basis system also in terms of the expansion coefficients $c^g_{\bar{n}}$:

$$E(x,z) = \sum_g e^{igx} e^{i\varkappa_g(|z|-a)} \sum_n c^g_{\bar{n}} E^g_{\bar{n}}(\pm a) \quad \text{for} \quad |z| \geqslant a\,, \tag{5.2}$$

where the sign + (−) refers to the region $z \geqslant a$ ($z \leqslant -a$), and

$$\varkappa_g = \sqrt{\omega^2 - (p+g)^2}\,. \tag{5.3}$$

Equation (5.3) for the normal component $\varkappa_g$ of the light wave vector in vacuum for the g-th Bragg channels again introduces a square-root ambiguity. However, the positions of the cuts for the perturbed system are known and are actually the same as for the basis system. This unambiguously determines the following choice of the root in Eq. (5.3):

$$\begin{aligned} &\operatorname{Im}\varkappa_g \leqslant 0 \qquad \text{if} \qquad |\operatorname{Re}\omega| > |p+g|\,, \\ &\operatorname{Im}\varkappa_g > 0 \qquad \text{if} \qquad |\operatorname{Re}\omega| < |p+g|\,, \end{aligned} \tag{5.4}$$

which can be obtained by analytic continuation, using the corresponding values of $\varkappa_g$ on the real frequency axis. For a better understanding of the meaning

of Eq. (5.4), let us assume for definiteness that $\mathrm{Re}\,\omega > 0$. This assumption does not impose any limitations as the modes with $\mathrm{Re}\,\omega < 0$ are solutions which are the complex conjugate of their mirror images with respect to the imaginary axis in the complex ω-plane — this is a general property of the RSs of an optical system, related to its time-inversion symmetry [13]. Then the first case in Eq. (5.4) corresponds to a so-called *open* Bragg channel, for which $e^{i\varkappa_g z}$ represents a wave propagating away from the system in the positive z-direction. Such a wave has a constant amplitude if the mode eigenfrequency ω is purely real (in this case this amplitude is zero in reality, see a discussion in Sec. 5.3 below), or an exponentially growing amplitude, due to $\mathrm{Im}\,\varkappa_g < 0$, if the mode eigenfrequency is complex, i.e. $\mathrm{Im}\,\omega < 0$. Note that this exponential growth is a typical spatial behaviour of the RSs [7, 23, 86]. The second case in Eq. (5.4) corresponds to a *closed* Bragg channels, for which the field due to $e^{i\varkappa_g z}$ is exponentially decaying with the distance from the system, due to $\mathrm{Im}\,\varkappa_g > 0$, no matter whether the eigenfrequency ω is real or complex. Note that the case of $\mathrm{Re}\,\omega = p + g$, not included in Eq. (5.4), corresponds to cut modes.

We can see from the expansions Eqs. (5.1) and (5.2) that the coefficients $c_{\bar{n}}^{g}$ act as amplitudes controlling how much each basis mode contributes to a given perturbed state. This makes it possible, in particular, to determine which basis mode the perturbed state "originates" from, that is, which basis mode it would evolve from if the position of the mode were traced out as the contrast of the periodic modulation is increased.

5.3 Bound states in the continuum and their formation mechanisms

As well as allowing us to be able to construct the perturbed electric field, the eigenvectors $c_{\bar{n}}^{g}$ of the RSE allow us to easily identify BICs in the system and to be able to distinguish between S-BICs and A-BICs. As BICs have localized (i.e. bound) wave functions, their eigenfrequencies ω have to be purely real, otherwise an excitation of the system into such an optical mode would decay in time, which would in turn require an exponential growth of the wave functions. And vice versa, all real-eigenfrequency modes have to have localized wave functions, which means they can only be bound states. A purely harmonic behaviour in vacuum (with a finite constant amplitude) is not possible for an isolated optical mode at real frequency as this would also mean a flow of energy to the outside of the system. Mathematically, this implies, in accordance with Eq. (5.4) and the discussion following it in Sec. 5.2, that

$$\sum_{n} c_{\bar{n}}^{g} E_{\bar{n}}^{g}(\pm a) = 0 \tag{5.5}$$

for every Bragg channel g satisfying the inequality

$$|p + g| < |\omega| \,, \tag{5.6}$$

where ω is the *real* frequency of the mode. This is a general condition for any BIC. Note that in addition to BICs, also guided modes with real frequencies $|\omega| < |p|$ can form in the energy spectrum of a PC slab in vacuum (the last inequality is modified for a PC slab with a substrate or two different substrates replacing vacuum on either side of the slab [7]).

For S-BICs, however, a stronger condition replaces Eq. (5.5):

$$c_{\bar{n}}^{g} = 0\,. \tag{5.7}$$

This should be fulfilled for all basis states n for the Bragg channels g selected by the inequality Eq. (5.6). In fact, as already mentioned in the start of this chapter, S-BICs are formed due to the decoupling of modes of different symmetry, so while all modes of one symmetry class couple to the radiation continuum outside the system and become leaky, some modes of the other symmetry class do not and remain bound to the system. All the matrix elements $V_{\bar{n}\bar{n}'}^{gg'}$ between different symmetry classes vanish by symmetry, and the RSE equation (2.30) yields immediately Eq. (5.7). For example, in the case of a PC slab for $p = 0$ and mirror symmetry in the z-direction, these two symmetry classes are, respectively, even and odd solutions in the periodic x-direction. The corresponding even and odd-parity basis modes do not couple to each other, leading to Eq. (5.7) for the even-mode contribution to the odd-parity states. From this follows, in particular, that Eq. (5.7) results in S-BICs existing only below the first Bragg channel threshold, i.e. for $|\omega| < 2\pi/d$, as it has been demonstrated numerically in [32]. One could even argue that S-BICs are simply guided modes of the odd-symmetry class.

Equation (5.7) is a defining characteristic for S-BICs that is not seen in A-BICs which would be otherwise difficult to differentiate. The RSE method reveals how this decoupling occurs mathematically. A-BICs, on the other hand, can form at any frequency given that the parameters of the system are properly tuned. Unlike S-BICs the values of $c_{\bar{n}}^{g}$ are not necessarily zero for leaky modes. Instead, according to Eq. (5.5), it is the summation of the basis electric fields at the edges of the system that becomes zero, representing destructive interference. For an A-BIC to form, this destructive interference only needs to occur

in channels that contain leaky modes, i.e. for all g satisfying Eq. (5.6).

The condition for A-BICs Eq. (5.5) with generally non-vanishing amplitudes $c_{\bar{n}}^{g}$ can be also seen as orthogonality of vectors with component $c_{\bar{n}}^{g}$ and $E_{\bar{n}}^{g}(\pm a)$, labeled by $\bar{n}$, for each relevant g. If only one value of g contributes (for example $g = 0$, for sufficiently small $|\omega|$), and the PC slab possesses a mirror symmetry in the z-direction, the same as for the basis system, then the two equations given by Eq. (5.5), with $+a$ and $-a$ in the argument of the basis functions, produce only one (for each parity in the z-direction) "vector orthogonality" condition for an A-BIC to occur, which is easy to satisfy by tuning a single parameter of the system, as demonstrated in Sec. 5.4 below. However, for a PC slab without mirror symmetry, and for larger frequencies, Eq. (5.5) contains two or more conditions of orthogonality of vectors, which are harder to meet and which may require a simultaneous tuning of, respectively, two or more parameters of the system.

As already mentioned at the start of this chapter, the condition for A-BICs Eq. (5.5), provided by the RSE, which physically reflects the phenomenon of destructive interference and cancellation of the field at the edges of the system, has some similarity with a BIC condition developed in the theory of an open Sinai billiard [85]. The latter presents an interesting example of an open optical system treated in a rigorous way without introducing the RSs explicitly, but rather mapping Maxwell's wave equation onto a non-Hermitian matrix eigenvalue problem, using as basis the eigenstates of a closed system supplemented with guided and evanescent modes of leaky channels. While the open Sinai billiard is not a periodic system, it has a remarkable similarity with a PC slab, in terms of the existence of open (i.e. leaky) and closed (i.e. evanescent) channels which are analogous, respectively, to the discussed above open and closed Bragg channels of a PC slab. It has been shown in [84, 85] that, neglecting the contri-

bution of evanescent channels, the condition determining BICs in such a system can be formulated in term of a vanishing coupling matrix element between a relevant mode of the closed resonator and the leaky channel. While for some BICs this approximation works very well, in some other cases the contribution of evanescent mode can more significant, as has been also demonstrated in [85]. In PC systems instead, the A-BIC condition Eq. (5.5) is exact.

5.4 Evolution of modes: Comparing Symmetry-protected and accidental BICs

One of the advantages of the RSE method is the speed at which it can calculate the RSs of an optical system within a wide spectral range. This becomes crucial if one needs to change one or several parameters of the optical system in order to optimise its optical properties or to achieve a desired effect. In fact, if the basis system remains the same while varying parameters of the target system, the perturbation matrix can be pre-calculated as it is using the same basis functions, or at least its calculation can be optimised. Then the only computationally expensive element of the RSE is matrix diagonalisation. For example, for the perturbations treated in this work with the relative error in the RS frequency of about 10^{-5} or lower, one needs for determining the full spectrum of the RSs in a wide spectral range to diagonalize a 4500×4500 matrix which requires only 680 seconds on a standard computer. This allows the RSE to be run several thousand times within a manageable time frame, in order to explore the parameter space of the PC system and to trace the evolution of its optical modes while its structural and/or material parameters are changing. This is particularly important for studying A-BICs, as discussed in the previous section.

In this section, we again use the cosine perturbation described in Eq. (3.12)

and vary the parameters of this perturbation (namely, the perturbation strength and width), in order to study symmetry protected and accidental BICs in such a system.

The evolution of a large number of the RSs with change of the permittivity contrast β has been already considered for this system in Ch 4. In this section, we focus only on a pair of the RSs originating from the fundamental guided modes of the homogeneous slab - that is, the modes that they can be traced from when varying β - corresponding to the first-order Bragg channels, i.e. with $g = g_{\pm 1}$. As already mentioned, we consider the RSs of the PC slab with the in-plane wave number $p = 0$ so the Bragg channels with opposite signs of g in the basis are degenerate by symmetry. This degeneracy also manifests itself in the orthogonality of even and odd states along the x-axis. As a consequence of this orthogonality, the matrix elements of the perturbation between even and odd basis states vanish by symmetry, thus allowing formation of S-BICs as discussed in Ch 5.3. Clearly, these S-BICs exist only for zero in-plane vector p that guarantees the mirror symmetry of the electro-magnetic field in the x-direction. With any deviation from $p = 0$ condition, breaking the symmetry, these S-BICs transform into modes with finite Q-factors.

Figure 5.1 demonstrates the evolution of the fundamental pair of RSs for $p = 0$ as the periodic modulation contrast β increases. As discussed in Ch. 4, being doubly degenerate by symmetry at $\beta = 0$ (no periodic modulation), the fundamental guided mode splits for a nonzero β into an S-BIC and a quasi-guided mode (QGM), the latter having a rather high but still finite Q-factor. These two modes are further separated as β increases. However, as clear from Fig. 5.1, for a certain value of β (at around $\beta \approx 4.34$), the QGM transforms into an A-BIC with an infinite Q-factor (corresponding to zero imaginary part of its eigenfrequency).

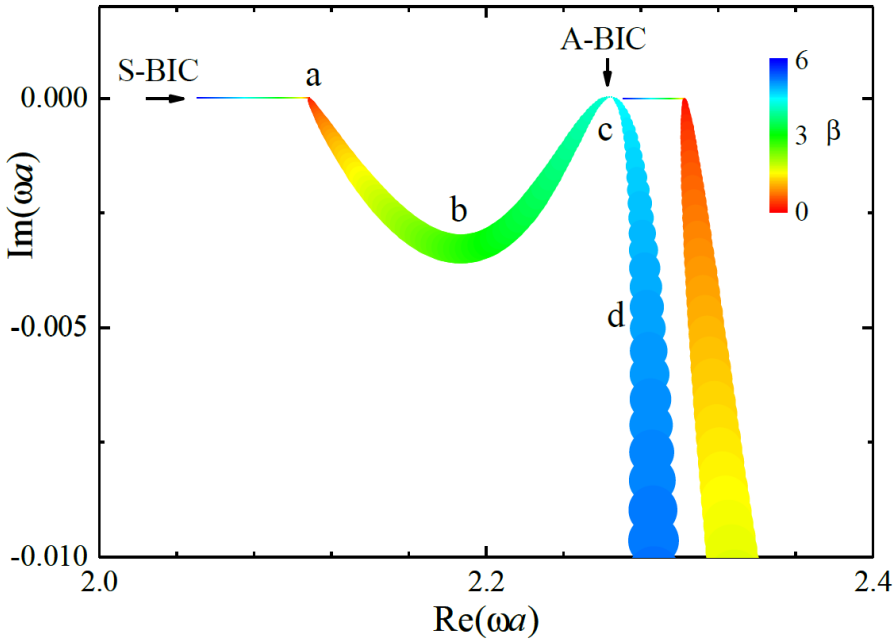

Figure 5.1: Evolution of the RS eigenfrequencies (centers of the colored circles) and the zeroth Bragg channel contribution $|C_0|$, defined by Eq. (5.8) (circle area), for the amplitude of the periodic modulation β (circle color) changing between $\beta = 0$ and $\beta = 6$. As β grows, a doubly degenerate fundamental guided mode of the first Bragg channel (a) splits into a symmetry protected BIC with an infinite Q-factor and a QGM with a finite Q-factor (b,d) which becomes an accidental BIC (c) at $\beta \approx 4.34$. The schematic of the system can be seen in Fig. 3.1. The basis system is a dielectric slab in vacuum, having width $2a$ and permittivity $\varepsilon = 6$. The perturbation has period $d = 2\pi/5$ and width $b = 0.5a$

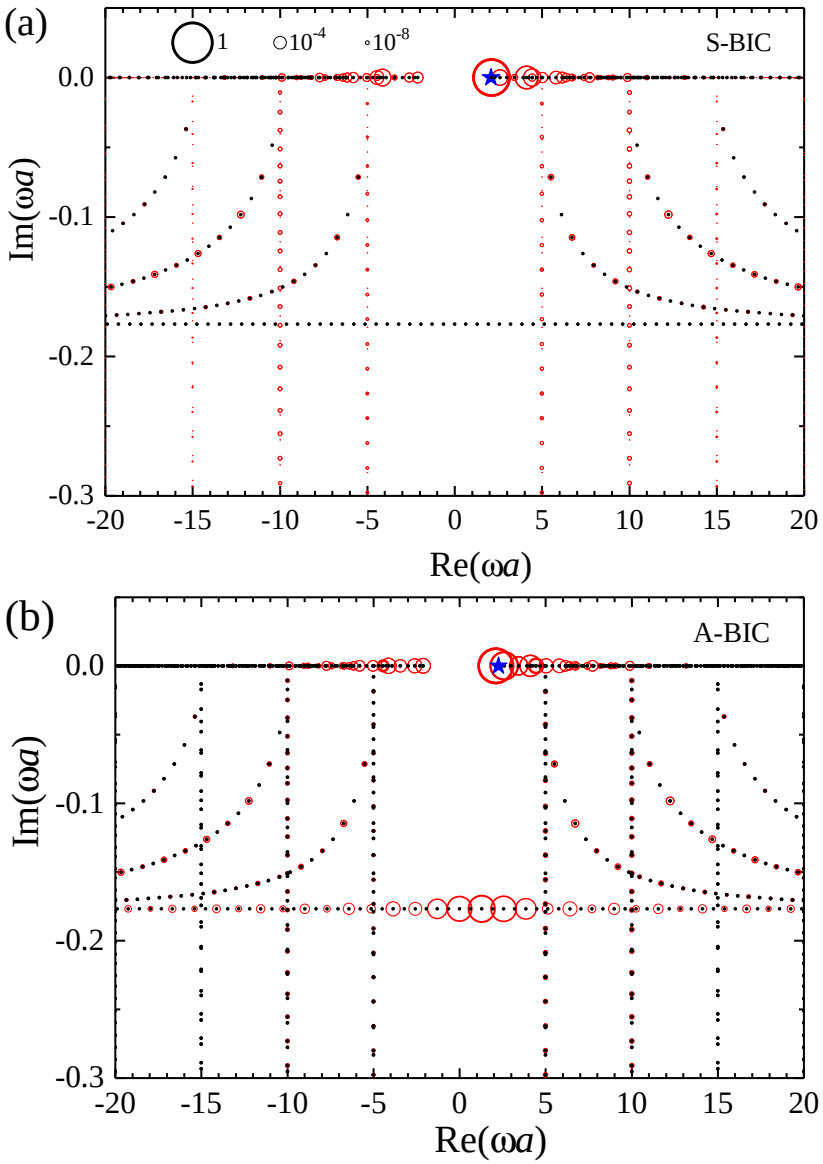

Figure 5.2: Basis mode contributions (red circles, centered at the basis mode frequencies) for (a) symmetry protected and (b) accidental BIC at $\beta = 4.34$, both originating from the same doubly degenerate fundamental guided mode of the homogeneous slab with $m = \pm 1$. The circle area is proportional to $\sqrt{|c_n^g|}$ of the basis mode amplitude c_n^g, and a key showing the relationship between the circle area and $|c_n^g|^2$ is given by back circles and the numbers next to them. Blue star gives the position of the BIC eigenfrequency and black dots of the basis RSs.

The symmetry-protected and accidental BICs, originating from the same fundamental guided mode of the homogeneous slab, are compared in Fig. 5.2, where the contribution of a large number of basis modes to both states is shown by red circles centered at the basis mode frequencies and having the area of the circle proportional to the modulus of the square root of the expansion coefficient, $\sqrt{|c^g_{\bar{n}}|}$. Among several thousand of modes used in the basis, only a limited number of basis states give an appreciable contribution to the perturbed RSs, with a clearly dominating role of the fundamental guided mode, see the largest circle close to the black star, which in turn shows the perturbed mode position on the real axis.

A remarkable difference between the two BICs is a vanishing (non-vanishing) contribution to S-BIC (A-BIC) of the individual basis modes of the zeroth Bragg channel. These basis modes all have the same imaginary part and equidistant separation in the complex frequency plane, see Fig. 5.2. In accordance with a discussion in Sec. 5.3 above, all $c^0_{\bar{n}} = 0$ for the S-BIC, while $c^0_{\bar{n}} \neq 0$ for the A-BIC, for all modes $\bar{n}$ of the same (even) parity along z-axis. However, the vector with components $c^0_{\bar{n}}$ is orthogonal to the vector $E^0_{\bar{n}}(a)$ for the A-BIC, as also discussed in Sec. 5.3. The absolute value of the dot product of these two vectors,

$$C_0 = \sum_{\bar{n}} c^0_{\bar{n}} E^0_{\bar{n}}(a), \tag{5.8}$$

is shown by the circle area in Fig. 5.1, while the center of the circle gives the position of the perturbed RS frequency. Clearly, C_0 is vanishing at the A-BIC and is strictly zero for the S-BIC at all values of the periodic modulation amplitude β.

The transformation of the QGM, passing through the A-BIC as β increases, is accompanied by a morphological change of the wave function, which is demonstrated in Fig. 5.3. It shows both the amplitude (intensity) and the phase (color)

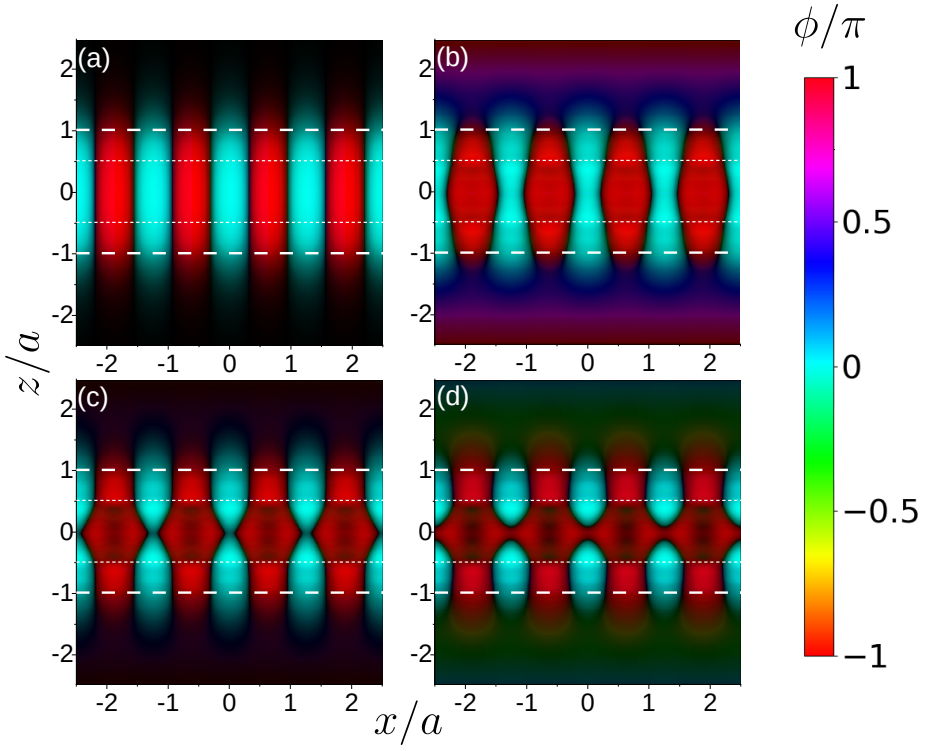

Figure 5.3: The amplitude (brightness) and phase (color) of the electric field of the fundamental optical mode in Fig. 5.1 at the positions labelled a-d, corresponding to the following mode type and permittivity contrast β: (a) fundamental basis guided mode of the first Bragg channel at $\beta = 0$; (b) QGM before the BIC, at $\beta = 3$; (c) A-BIC at $\beta \approx 4.34$; (d) QGM after the BIC, at $\beta = 5$. The thick (thin) dashed lines indicate the edges of the slab at $z = \pm a$ (periodic perturbation at $z = \pm b$). $\varepsilon = 6$, $b = 0.5a$, $d = 2\pi/5$

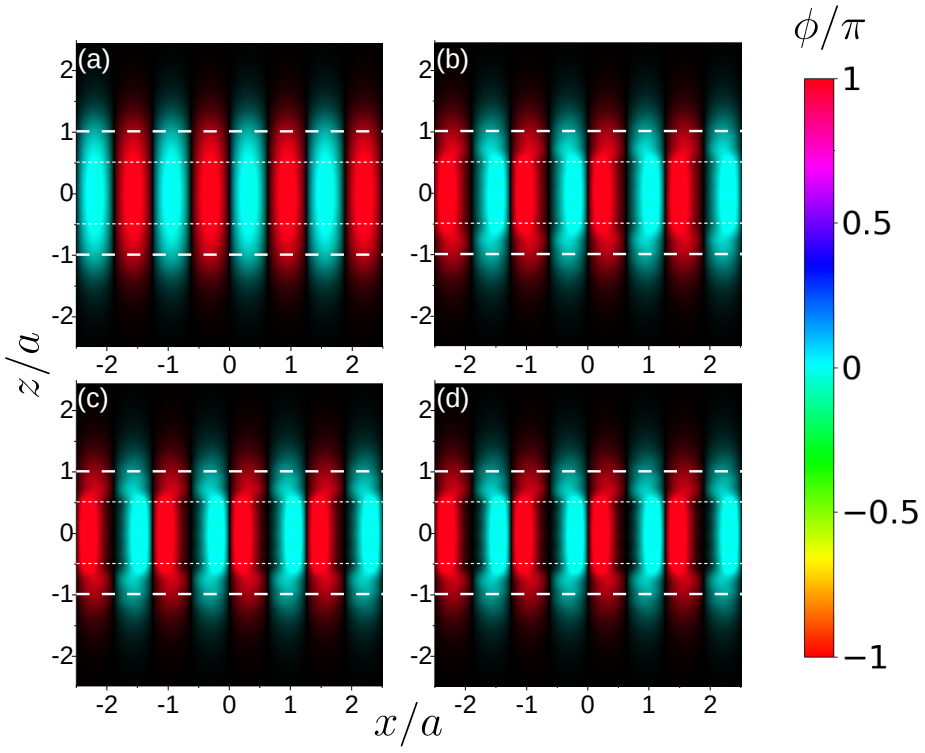

Figure 5.4: As Fig. 5.3 but for the S-BIC shown in Fig. 5.1. The values of the permittivity contrast β and all other parameters are the same as in Fig. 5.3.

of the wave function of the QGM at four different values of β, starting from $\beta = 0$ in Fig. 5.3(a) at which the RS coincides with the fundamental guided mode of the homogeneous basis slab. The other three panels (b)–(d) in Fig. 5.3 show the wave function of the mode before, at, and after the A-BIC. These four positions are also labeled (with the same letters a-d) in the complex-frequency plot, Fig. 5.1. As the QGM originates from the fundamental guided mode of the homogeneous slab, corresponding to the first Bragg channel, the amplitude of the electric field of this fundamental QGM before it transforms into the A-BIC has only one maximum in the z-direction and two maxima per period d in the x-direction, the same as for the basis mode. After the A-BIC, however, the field amplitude shows three maxima in the z-direction representing a growing contribution from a higher-order basis mode, specifically the third guided mode in the first Bragg channel. Note that the second guided mode does not contribute since it is of the opposite parity to the fundamental mode from which the QGM originates. In the x-direction, the morphology of QGM does not change much: There are always two maxima per period indicating that there is no major change in the contribution from higher-order Bragg channels within this β range.

It can also be seen that the field quickly decays outside of the system, in a similar way for both the basis mode and the A-BIC, compare Fig. 5.3(a) and (c). In fact, since both modes are bound, there are no travelling or exponentially growing solutions outside the system; instead, there are only evanescent waves, unlike the other two cases which are shown in Fig. 5.3(b) and (d). For them, a non-vanishing growing field, though very small, is seen in the region outside the system. One can see from the color of the plots that the fields in Fig. 5.3(b) and (d) are almost real, which is consistent with the fact that the Q-factor of the QGM shown is very high, see Fig. 5.1. Interestingly, the phase of the

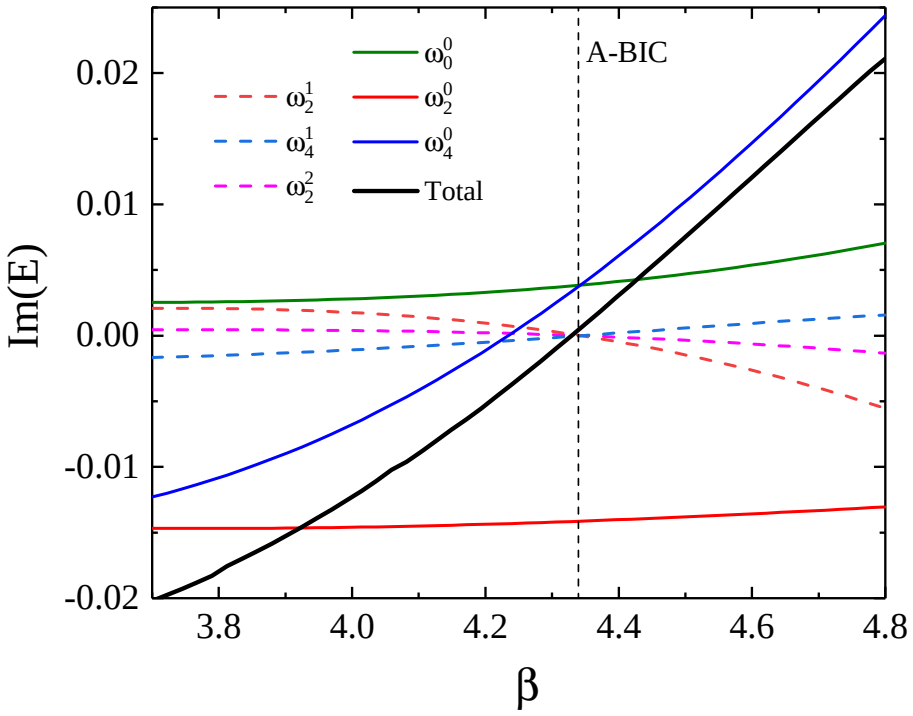

Figure 5.5: Contributions of basis modes to the imaginary part of the normalised electric field of the fundamental QGM as functions of the permittivity contrast β. Only the top 6 contributions are shown, corresponding to the basis mode frequencies $\omega_0^0 = -0.177i$, $\omega_2^0 = 1.283 - 0.177i$, $\omega_4^0 = 2.565 - 0.177i$, $\omega_2^1 = 2.108$, $\omega_4^1 = 2.605$, and $\omega_2^2 = 4.123$. The total electric field of the QGM is given by a black thick line. The vertical dashed line shows the value of $\beta = 4.34$ where the QGM becomes the accidental BIC. $b = 0.5a$, $d = 2\pi/5$, $\varepsilon = 6$

wave function is either close to 0, or to π, with the amplitude of the wave function almost vanishing on lines separating these two phase regions. The wave functions of the basis guided mode and the A-BIC shown, respectively, in Fig. 5.3(a) and (c) are purely real, as expected for any bound states, having also purely real eigenfrequencies. These real wave functions just change their sign along the lines separating the above mentioned 0- and π-phase areas.

For the same values of β as in Fig. 5.3, we show in Fig. 5.4 also the evolution of the S-BIC which originates from the same doubly degenerate pair of guided modes as the QGM mode/A-BIC in Fig. 5.3. Clearly, the modes shown in Figs. 5.3 and 5.4 are, respectively, of the even and odd parity in the x-direction. The fact that the S-BIC does not gain any leakage for any value of β is consistent with the dark areas outside the slab in all four panels of Fig. 5.4. As β increases, the S-BIC does not change much within the slab either. In fact, there is only a slight morphological change in the x-direction, but no change in the z-direction is observed. This suggests that this S-BIC is not communicating much with higher order modes. The overall lack of evolution of the S-BIC is also consistent with the fact that this mode is not moving much in the complex frequency plane as compared to its even counterpart, as it is clear from Fig. 5.1. The S-BIC is also quite isolated in frequency from other basis states which effectively reduces their impact. In fact, as we know, the S-BIC is not communicating at all with the nearby $g = 0$ modes due to symmetry, compare Figs. 5.2 (a) and 5.2 (b).

We now want to see how the summation of complex basis electric fields shown in Eq. (5.1) create an entirely real field at the A-BIC. To do this, we plot in Fig. 5.5 the imaginary part of the weighted basis fields $c_{\tilde{n}}^{g} E_{\tilde{n}}^{g}$ against β, the sum of which will clearly be zero at the A-BIC. In order to produce a readable plot we can limit ourselves to just the top few contributors. In this case, only the top six modes with the highest contributions to the A-BIC, well seen in

Fig. 5.2(b), are used.

It can be seen in Fig. 5.5 that the imaginary part of the weighted basis fields from the guided modes all come to zero at the A-BIC. This is expected behaviour since the guided-mode fields and the A-BIC field are purely real, so naturally the corresponding eigenvector components $c_{\tilde{n}}^{g}$ are also real. There are, however, leaky modes from the $g = 0$ Bragg channel which are all complex (except the central mode) and so do not necessarily produce real fields at the A-BIC, thus these fields are required to cancel in some way. Fig. 5.5 shows that the weighted basis fields do not have a simple cancellation at the A-BIC. Instead, there are a series of partial cancellations leading to a complete cancellation overall showing that indeed the A-BICs are a result of "accidental" destructive interference of leaky modes.

5.5 Varying other parameters

We now extend the parameter space while looking for A-BICs to include both the perturbation strength β and the perturbation width b. By varying both parameters, we need to run the RSE thousands of times, where both the high efficiency and the high accuracy of the RSE become crucial. Focusing on the same fundamental QGM, we plot in Fig. 5.6 its Q-factor defined as $Q = |\mathrm{Re}\,\omega/(2\mathrm{Im}\,\omega)|$, color-coded on the β–b plane. Both parameters have natural limits, $b < a$ and $\beta < \varepsilon_s$, which were used in the plot. The latter condition is a requirement that the system stays dielectric, having a positive permittivity, while the former is a fundamental limitation of the RSE that the perturbation must stays within the volume of the basis system. Note, however, that the present version of RSE applied to planar PC structures suffers from the lack of convergence as $b \to a$ as discussed in Ch. 3.7, so that Fig. 5.6 shows a plot up to $b = 0.75a$ only (but the data is reliably calculated up to $b = 0.95a$). The Q-factor of the studied

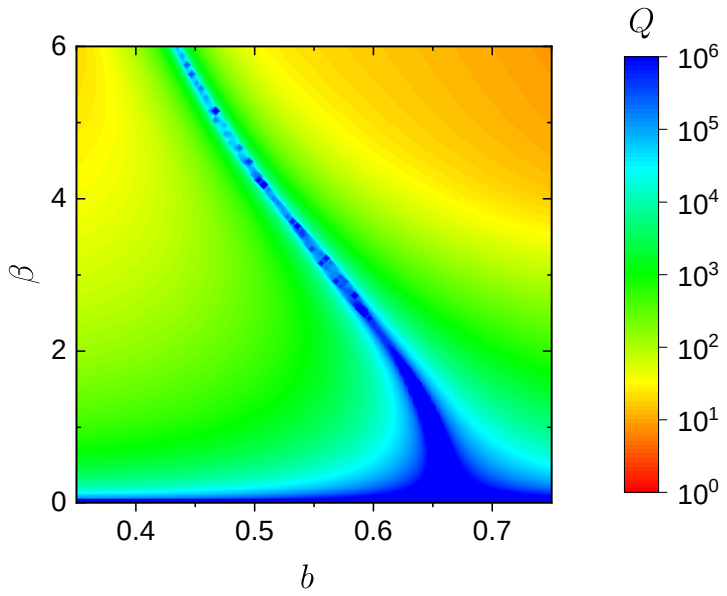

Figure 5.6: The quality factor Q of the fundamental QGM of the PC slab as a function of the permittivity contrast β and the half-width of the perturbation layer, b. $\varepsilon = 6$, $d = 2\pi/5$

mode reaches a numerical value of $Q = 10^6$ as it is clear from Fig. 5.6, which also demonstrates a high accuracy of the RSE calculation of the mode, with the relative error of about 10^{-6}.

We see from Fig. 5.6 that an A-BIC is formed at any value of β, provided that the other parameter is properly tuned, presenting a line in the two-dimensional parameter space. However, no A-BIC is formed for $b > 0.7a$ which can be understood as the system does not have thick enough substrate layer (not affected by the periodic modulation) where the destructive interference of leaky modes necessary for A-BIC formation could occur. Clearly, the properties of the A-BIC are also affected by both parameters as can be seen from the strongly inhomogeneous profile of the Q-factor. In fact the range of high Q-values becomes wider as β decreases, eventually approaching the limit of the infinite Q for the original guided mode of the homogeneous dielectric slab at $\beta = 0$, where b is no longer

a variable of the system.

5.6 Conclusion

We have applied the resonant-state expansion (RSE) to planar photonic-crystal structures, in order to find in these systems symmetry protected and accidental bound-states in the continuum (BICs) and to study their properties. We have shown that the eigenvector analysis naturally following from the RSE formalism is a useful tool for identifying BICs, and have provided a rigorous mathematical criterion for differentiating between symmetry-protected and accidental BICs. We have demonstrated how the electro-magnetic field of a resonant state of a photonic-crystal slab can be broken down into homogeneous-slab basis field components and how those contributions change as the periodic perturbation is modified. In particular, the basis electric fields sum together to create an entirely real field of an accidental BIC, which true to its name is an accidental cancellation of an infinite number of partial leaky waves with no one field fully compensating another. We have furthermore demonstrated that the RSE is an efficient tool for finding the BICs in planar photonic crystal systems due to the unprecedented speed at which it can calculate the modes, thus allowing a multidimensional parameter space to be explored with a high resolution.

Chapter 6

Conclusions

We have presented a unique approach in the theory of planar photonic-crystal structures, which allows us to reveal the nature of resonances in the optical spectra and to quantify them precisely. This concept is based on using the analytical resonant states of a homogeneous slab, along with its cut modes responsible for Rayleigh-Wood anomalies, as the most natural and simple basis for expanding the resonant states of a photonic-crystal slab. We have developed the photonic-crystal resonant-state expansion (PC-RSE), capable of doing this accurately and efficiently, and illustrated it on examples of TE-polarized modes in a photonic crystal slab with a 1D periodic harmonic modulation. These examples provided a proof of concept and also a verification of the PC-RSE by comparing it with the accurate scattering-matrix method.

We have presented a general formalism of the PC-RSE and its application to dielectric photonic-crystal structures. We investigated the dyadic Green's function of the slab and introduced the concept of cut modes in ω-space which allows the resonant-state expansion to work as efficiently as in k-space, where there are no cuts. We demonstrate that the PC-RSE is an asymptotically exact

approach, which (i) depends on a single parameter – truncation frequency $\omega_{\max}$, determining the basis size; (ii) guarantees completeness, i.e. has no missing or spurious modes, so that any observable can be represented as a superposition of the modes found; (iii) technically reduces solving Maxwell's wave equation to a matrix diagonalisation, thus making the application of the PC-RSE a fully automated and straightforward procedure, not requiring any supervision. The PC-RSE provides an accurate and efficient tool for calculating all physically relevant eigenstates of the photonic crystal system within the selected spectral range. In particular, it can be effectively used repeatedly many times or in parallel, in order to investigate an arbitrarily large space of the physical parameters characterising the system, for revealing and optimising its fundamental properties. One of the important future applications of the PC-RSE is optimisation of photonic-crystal cavities, with a correct account of the radiative losses of high-quality modes.

We have also demonstrated how the PC-RSE can be used to study the origin and physical properties of the optical modes. For illustration, we have traced the evolution of the optical modes in a photonic crystal slab increasing the amplitude of the periodic modulation of the permittivity, starting from a homogeneous slab with no modulation. This allowed us, in particular, to reveal the dominant role of the waveguide modes in the formation of bound states in the continuum and quasi-guided modes. Furthermore, the PC-RSE allows us to quantify precisely the contribution of each basis state to the optical mode of interest, which we have also demonstrated in the present work.

We used the PC-RSE to study the properties of accidental and symmetry-protected bound states in the continuum in photonic crystal slabs. We showed that the eigenvectors found using the PC-RSE formalism naturally creates a useful tool for identifying BICs and provided mathematical criteria for S-BICs

and A-BICs respectively. The PC-RSE allowed us to find the electric fields of the photonic crystal modes by describing them as a superposition of electric fields from the basis. The efficiency of the PC-RSE allowed us to study the electric field at many different values of the permittivity modulation strength, showing morphological changes to the field as the modes evolves into a bound states in the continuum.

Appendix A

Dyadic Green's function for a non-periodic slab

Let us consider arbitrary dependencies of the permittivity $\varepsilon(z)$ and permeability $\mu(z)$ within a non-periodic slab occupying the region $|z| \leqslant a$ and surrounded by vacuum, so that outside the slab $\varepsilon = \mu = 1$. Denoting the components of the dyadic GF as $(\hat{\mathcal{G}}_p)_{ij} = G_{ij}(z, z')$, Eq. (2.16) becomes

$$\begin{pmatrix} \omega\varepsilon & -\partial_z & ip \\ \partial_z & \omega\mu & 0 \\ -ip & 0 & \omega\mu \end{pmatrix} \begin{pmatrix} G_{11} & G_{12} & G_{13} \\ G_{21} & G_{22} & G_{23} \\ G_{31} & G_{32} & G_{33} \end{pmatrix} = \hat{\mathbf{1}}\delta(z - z')\,. \tag{A.1}$$

Owing to the reciprocity of the optical system, the GF has the following property:

$$G_{ij}(z, z') = G^{\dagger}_{ji}(z', z)\,, \tag{A.2}$$

where the adjoint † means replacing $p \to -p$.

From Eq. (A.1) we obtain for the first column of $\hat{\mathcal{G}}_p$:

$$\begin{aligned}
\hat{U}(\mu;\omega)G_{11}(z,z';\omega) &= \omega\mu(z)\delta(z-z')\,, && \text{(A.3)}\\
G_{21}(z,z') &= -\frac{1}{\omega\mu(z)}\partial_z G_{11}(z,z')\,, && \text{(A.4)}\\
G_{31}(z,z') &= \frac{ip}{\omega\mu(z)}G_{11}(z,z')\,, && \text{(A.5)}
\end{aligned}$$

where the operator $\hat{U}$ is defined as

$$\hat{U}(\zeta;\omega) = \zeta(z)\partial_z\frac{1}{\zeta(z)}\partial_z + \omega^2\varepsilon(z)\mu(z) - p^2 \qquad \text{(A.6)}$$

with $\zeta(z)$ being a weight function. For the second column of $\hat{\mathcal{G}}_p$, it follows from Eq. (A.1) that

$$\begin{aligned}
G_{12}(z,z') &= \frac{1}{\omega\chi(z)}\partial_z G_{22}(z,z')\,, && \text{(A.7)}\\
\hat{U}(\chi;\omega)G_{22}(z,z') &= \omega\chi(z)\delta(z-z')\,, && \text{(A.8)}\\
G_{32}(z,z') &= \frac{ip}{\omega\mu(z)}G_{12}(z,z')\,, && \text{(A.9)}
\end{aligned}$$

where

$$\chi(z) = \varepsilon(z) - \frac{p^2}{\omega^2\mu(z)}\,. \qquad \text{(A.10)}$$

Note that Eq. (A.8) is essentially the same as Eq. (A.3), provided that $\mu(z)$ is replaced with $\chi(z)$. Finally, for the third column of $\hat{\mathcal{G}}_p$ we obtain

$$\begin{aligned}
\hat{U}(\mu;\omega)G_{13}(z,z') &= -ip\delta(z-z')\,, && \text{(A.11)}\\
G_{23}(z,z') &= -\frac{1}{\omega\mu(z)}\partial_z G_{13}(z,z')\,, && \text{(A.12)}\\
G_{33}(z,z') &= \frac{ip}{\omega\mu(z)}G_{13}(z,z') + \frac{\delta(z-z')}{\omega\mu(z)}\,, && \text{(A.13)}
\end{aligned}$$

demonstrating in particular that the longitudinal component $G_{33}(z,z')$ is divergent at $z=z'$, due to the δ function in the last term. Also, Eq. (A.11) contains exactly the same operator as in Eq. (A.3), and therefore

$$G_{13}(z,z') = -\frac{ip}{\omega\mu(z')} G_{11}(z,z')\,. \tag{A.14}$$

Using the reciprocity Eq. (A.2) and Eqs. (A.4), (A.12), and (A.14), we further obtain

$$G_{12}(z,z') = G_{21}(z',z) = -\frac{1}{\omega\mu(z')}\partial_{z'} G_{11}(z,z')\,, \tag{A.15}$$

$$G_{32}(z,z') = G_{23}^{\dagger}(z',z) = -\frac{ip}{\omega^2\mu(z)\mu(z')}\partial_{z'} G_{11}(z,z')\,, \tag{A.16}$$

and therefore

$$\begin{aligned} G_{22}(z,z') &= -\frac{1}{\omega\mu(z)}\partial_z G_{12}(z,z') + \frac{\delta(z-z')}{\omega\mu(z)} \\ &= \frac{1}{\omega^2\mu(z)\mu(z')}\partial_z\partial_{z'} G_{11}(z,z') + \frac{\delta(z-z')}{\omega\mu(z)}\,. \end{aligned} \tag{A.17}$$

Finally,

$$G_{13}(z,z') = G_{31}^{\dagger}(z',z) = -\frac{ip}{\omega\mu(z')} G_{11}(z,z')\,, \tag{A.18}$$

in agreement with Eq. (A.14). Collecting all this information about the GF components, we find a compact expression for the full dyadic GF:

$$\begin{aligned} \hat{\mathcal{G}}_p(z,z') &= \hat{O}_p(z;\omega)\otimes\hat{O}_{-p}(z';\omega) G_{11}(z,z') \\ &\quad + \frac{\hat{\mathbf{1}}_2+\hat{\mathbf{1}}_3}{\omega\mu(z)}\delta(z-z')\,, \end{aligned} \tag{A.19}$$

where $\hat{\mathbf{1}}_j$ are 3×3 matrices with elements $(\hat{\mathbf{1}}_j)_{ii'} = \delta_{ii'}\delta_{ij}$ and $\hat{O}_p$ is a vector

operator defined as

$$\hat{O}_p(z;\omega) = \begin{pmatrix} 1 \\ -\frac{1}{\omega\mu(z)}\partial_z \\ \frac{ip}{\omega\mu(z)} \end{pmatrix} . \tag{A.20}$$

Solving Eq. (A.3) with outgoing boundary conditions and studying the pole structure and the cuts of the GF in the complex ω-plane, as done in Appendix B for a general planar system, allows us to find the ML expansion for G_{11}:

$$G_{11}(z,z) = \sum\!\!\!\!\!\!\int_n \frac{E_n(z)E_n(z')}{\omega-\omega_n} , \tag{A.21}$$

and also for

$$g(z,z') = \frac{G_{11}(z,z)}{\omega} = \sum\!\!\!\!\!\!\int_n \frac{E_n(z)E_n(z')}{\omega_n(\omega-\omega_n)} , \tag{A.22}$$

where $E_n(z)$ is the only non-vanishing component (along y) of the electric field of the RS n, satisfying an equation

$$\hat{U}(\mu;\omega_n)E_n(z) = 0 , \tag{A.23}$$

or $E_n(z)$ is the wave function of the cut pole, see Appendix B for details. Obviously, $E_n(z)$ depends on p^2, as so does the operator $\hat{U}$, and thus $E_n(z)$ is not sensitive to a change of sign of p, so that $E_n^\dagger(z) = E_n(z)$.

Comparing Eqs. (A.21) and (A.22) and substituting (A.22) into Eq. (A.3), we obtain a closure relation

$$\varepsilon(z) \sum\!\!\!\!\!\!\int_n E_n(z)E_n(z') = \delta(z-z') \tag{A.24}$$

and a sum rule

$$\sum\!\!\!\!\!\!\int_n \frac{E_n(z)E_n(z')}{\omega_n} = 0 . \tag{A.25}$$

Using Eqs. (A.21) and (A.25), we obtain from Eq. (A.19) the ML expansion Eq. (2.18) of the full dyadic GF, in which

$$\boldsymbol{\mathcal{F}}_n(z;p) = \hat{O}_p(z;\omega_n)E_n(z)\,. \tag{A.26}$$

Note that in general, one also needs to include in Eq. (2.18) for completeness longitudinal static modes, in order to take into account the effect of the $\omega = 0$ pole of the GF.

Appendix B

Mittag-Leffler expansion of the GF for a homogeneous system

Let us now consider the scalar GF $g(z, z')$ of a general planar system homogeneous in the x-direction and described by arbitrary functions $\varepsilon(z)$ and $\mu(z)$, and derive its ML expansion given by Eq. (A.22). The GF satisfies an equation

$$\hat{U}_{k^2}(z)g(z, z') = \mu(z)\delta(z - z')\,, \tag{B.1}$$

where the operator $\hat{U}_{k^2}(z)$ is given by

$$\hat{U}_{k^2}(z) = \mu(z)\partial_z \frac{1}{\mu(z)}\partial_z + k^2\varepsilon(z)\mu(z) + p^2[\varepsilon(z)\mu(z) - 1]\,, \tag{B.2}$$

in accordance with it definition Eq. (A.6), now written in terms of $k^2 = \omega^2 - p^2$.

To simplify the derivation, we assume that $\varepsilon(z) = \mu(z) = 1$ outside the

system ($|z| > a$). In this case Eq. (B.1) outside the system takes the form

$$(\partial_z^2 + k^2) g(z, z') = \delta(z - z') \tag{B.3}$$

with k being the normal component of the wave number in vacuum. Applying the outgoing wave boundary conditions, we find that

$$g(z, z') = g(\pm a, z') e^{\pm ikz} \quad \text{for} \quad |z| > a \quad \text{and} \quad |z'| < a \,, \tag{B.4}$$

where $+$ $(-)$ refers to $z > a$ ($z < -a$). The outgoing wave boundary conditions for solving Eq. (B.1) can therefore be written in the following way

$$(\partial_z \mp ik)\; g(z, z')|_{z=\pm a} = 0 \,, \tag{B.5}$$

explicitly showing that $g(z, z')$ is an *analytic* function of k. Having a countable number of simple poles in the complex k-plane, which are at the RS wave numbers, $k_n = \sqrt{\omega_n^2 - p^2}$, and are vanishing at $k \to \infty$, the GF $g(z, z')$ can be written as

$$g(z, z') = \sum_n \frac{R_n(z, z')}{k - k_n} \,, \tag{B.6}$$

using the Mittag-Leffler theorem Eq. (1.26). To find an explicit form of the residue $R_n(z, z')$ we use Maxwell's wave equation without sources

$$\hat{U}_{k_n^2}(z) E_n(z) = 0 \,, \tag{B.7}$$

determining the RS wave functions $E_n(z)$, as well as the one with a source term [12, 55],

$$\hat{U}_{k^2}(z) E(z; k) = \mu(z)(k - k_n)\sigma_n(z) \,, \tag{B.8}$$

determining its analytic continuation $E(z; k)$ in the complex k-plane about the

point k_n, such that $E(z;k_n) = E_n(z)$. The source $\sigma_n(z)$ can be any function vanishing outside the system and normalised in such a way that

$$\int_{-a}^{a} E_n(z)\sigma_n(z)dz = k_n\,. \tag{B.9}$$

In optical systems with degenerate RSs (e.g due to symmetry), such that $k_n = k_m$ for $m \neq n$, $\sigma_n(z)$ is chosen in such a way that $\int_{-a}^{a} E_m(z)\sigma_n(z)dz = \delta_{nm}$.

Solving Eq. (B.8) with the help of the GF $g(z,z')$ and using its ML expansion Eq. (B.6), we find

$$E(z;k) = \sum_{n'} \frac{k-k_n}{k-k_{n'}} \int_{-a}^{a} R_{n'}(z,z')\sigma_n(z')dz'\,. \tag{B.10}$$

Then taking the limit $k \to k_n$, Eq. (B.10) becomes

$$E_n(z) = \int_{-a}^{a} R_n(z,z')\sigma_n(z')dz'\,, \tag{B.11}$$

which can be written, after combining it with Eq. (B.9), as

$$\int_{-a}^{a} \left[\frac{E_n(z)E_n(z')}{k_n} - R_n(z,z')\right] \sigma_n(z')dz' = 0\,. \tag{B.12}$$

The last equation must be satisfied for any normalised $\sigma_n(z)$, suited for generating the analytic continuation. Clearly, such a function is not unique, therefore the integrand in the last equation should be vanishing, which gives $R_n(z,z') = E_n(z)E_n(z')/k_n$ and results in the following series for the GF:

$$g(z,z') = \sum_{n} \frac{E_n(z)E_n(z')}{k_n(k-k_n)}\,. \tag{B.13}$$

We now find the normalisation of $E_n(z)$ which is determined by the ML form Eq. (B.13), which in turn follows from the normalisation of the source Eq. (B.9).

We therefore use it again, substituting $\sigma_n(z)$ from Eq. (B.8) into Eq. (B.9) and subtracting a similar integral vanishing due to Eq. (B.7):

$$\begin{aligned}(k-k_n)k_n &= \int_{-a}^{a}\frac{1}{\mu}E_n\hat{U}_{k^2}E dz - \int_{-a}^{a}\frac{1}{\mu}E\hat{U}_{k_n^2}E_n dz \\ &= \left[\frac{E_n}{\mu}\partial_z E - \frac{E}{\mu}\partial_z E_n\right]_{-a}^{a} + (k^2-k_n^2)\int_{-a}^{a}E_n E\varepsilon dz\,,\end{aligned}$$

where the first term in the second line is obtained integrating by parts. Finally, using the outgoing wave boundary conditions for E and E_n,

$$\left(\frac{1}{\mu(z)}\partial_z \mp ik\right)E(z;k)|_{z=\pm a} = 0\,, \tag{B.14}$$

$$\left(\frac{1}{\mu(z)}\partial_z \mp ik_n\right)E_n(z)|_{z=\pm a} = 0\,, \tag{B.15}$$

similar to Eq. (B.5), we arrive, after taking again the limit $k \to k_n$, at the normalisation condition for the RS wave function:

$$2\int_{-a}^{a}E_n^2(z)\varepsilon(z)dz - \frac{E_n^2(a)+E_n^2(-a)}{ik_n} = 1\,, \tag{B.16}$$

which is the same as the one provided in [14] without proof.

Note that Eq. (B.16) is equivalent to the general normalisation Eq. (2.20) used for the TE polarisation. In fact, using Eq. (2.20) for $z_1 = -a$ and $z_2 = a$ and the fields replaced by their analytic continuations for the purpose of taking the frequency derivatives, we find (denoting here for brevity iH with just H)

$$1 = \int_{-a}^{a}\left[\varepsilon E^2 + \mu(H_x^2 - H_z^2)\right]dz - \left[E\partial_\omega H_x - H_x\partial_\omega E\right]_{-a}^{a}\,, \tag{B.17}$$

(see Eqs. (2.5), (A.20), and (A.26)). Then using

$$H_x = -\frac{1}{\omega\mu}\partial_z E\,, \quad H_z = \frac{ip}{\omega\mu}E\,, \tag{B.18}$$

and

$$\left(\mu\partial_z\frac{1}{\mu}\partial_z+\omega^2\varepsilon\mu-p^2\right)E=0\,, \tag{B.19}$$

valid for $k=k_n$, we find, integrating by parts:

$$\begin{aligned}
&\int_{-a}^{a}\mu(H_x^2-H_z^2)dz\\
&=\frac{1}{\omega^2}\int_{-a}^{a}\frac{1}{\mu}[(\partial_z E)^2+p^2E^2]dz\\
&=\frac{[E\partial_z E]_{-a}^{a}}{\omega^2}+\frac{1}{\omega^2}\int_{-a}^{a}\frac{1}{\mu}\left[-E\mu\partial_z\frac{1}{\mu}\partial_z E+p^2E^2\right]dz\\
&=\frac{[E\partial_z E]_{-a}^{a}}{\omega^2}+\int_{-a}^{a}\varepsilon E^2dz\,.
\end{aligned} \tag{B.20}$$

We then use the analytic form of the fields outside the system:

$$E(z;k)=A_{\pm}e^{\pm ikz}\,,\quad H_x(z;k)=\mp\frac{ik}{\omega}E(z;k)\,, \tag{B.21}$$

where, again, $+$ $(-)$ corresponds to $z\geqslant a$ $(z\leqslant -a)$, and the amplitudes $A_{\pm}$ are also functions of ω or k. However, their frequency dependence does not contribute to the normalisation, since

$$E\partial_\omega H_x-H_x\partial_\omega E=\mp E^2\partial_\omega\frac{ik}{\omega}=\mp\frac{p^2}{ik\omega^2}E^2\,. \tag{B.22}$$

Collecting all the "surface" terms and differentiating the field outside the system, using the explicit form of E given by Eq. (B.21), we obtain

$$\begin{aligned}
&-[E\partial_\omega H_x-H_x\partial_\omega E]_{-a}^{a}+\frac{[E\partial_z E]_{-a}^{a}}{\omega^2}\\
&=\left(\frac{ip^2}{k\omega^2}+\frac{ik}{\omega^2}\right)\left[E^2(a)+E^2(-a)\right]\\
&=-\frac{E^2(a)+E^2(-a)}{ik}\,,
\end{aligned} \tag{B.23}$$

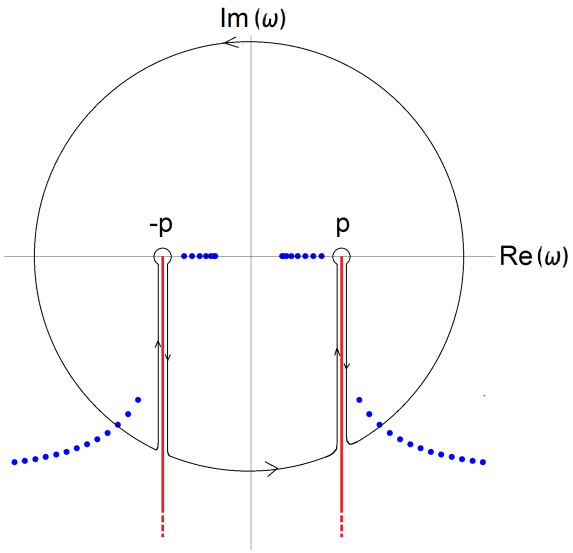

Figure B.1: Poles (blue dots) and cuts (red lines) of the GF in the complex ω plane, as well the contour of integration leading to the ML expansion Eq. (B.26), which includes the cut contributions displayed.

which proves that Eq. (2.20) results in the normalisation given by Eq. (B.16).

Equation (B.13) is the ML series of the GF in k-representation. However, the RSE formulated in Ch.2 requires a ML form of the GF in the ω-representation. Being treated as a function of frequency ω, the GF has simple poles due to the RSs at $\omega = \omega_n$ (where $\omega_n^2 = k_n^2 + p^2$), which are distributed in the complex ω plane symmetrically with respect to the imaginary axis, see Fig. B.1. The residues of the GF at these poles are given by

$$\begin{aligned} \lim_{\omega\to\omega_n} g(z,z')(\omega-\omega_n) &= \left.\frac{\partial\omega}{\partial k}\right|_{k_n} \lim_{k\to k_n} g(z,z')(k-k_n) \\ &= \frac{k_n}{\omega_n} R_n(z,z')\,, \end{aligned} \tag{B.24}$$

where $R_n(z,z')$ is found earlier (see Eq. (B.13)).

Apart from these poles, the GF $g(z,z')$ is analytic in the complex k-plane, as

shown above. However, in the complex ω plane $g(z, z')$ has branch cuts, owing to the link between k and ω,

$$k = \sqrt{\omega^2 - p^2}\,, \tag{B.25}$$

with the branch points at $\omega = \pm p$. Therefore, applying the ML theorem in the frequency plane results instead in

$$g(z, z') = \sum_n \frac{E_n(z)E_n(z')}{\omega_n(\omega - \omega_n)} + I_1(z, z'; \omega) + I_2(z, z'; \omega)\,, \tag{B.26}$$

where the sum includes only the RSs on the selected Riemann sheet, which in our case include all the WG and FP modes but does not contain anti-WG modes, unlike the series in Eq. (B.13). Integrals

$$I_{1,2}(z, z'; \omega) = -\frac{1}{2\pi i}\int_{\pm p}^{\pm p - i\infty} \frac{\Delta g(z, z'; \omega')}{\omega - \omega'} d\omega'\,, \tag{B.27}$$

describe the contribution of the cuts, which are chosen as vertical straight lines in the complex ω-plane going from the branch points $\pm p$ down to $-i\infty$, see Fig. B.1. According to [16], this choice of the cuts almost minimizes their contribution to the GF. The jump of the GF value across the cut is given by the function

$$\Delta g(z, z'; \omega) = g_k(z, z') - g_{-k}(z, z')\,, \tag{B.28}$$

where we have added index k for convenience, in order to emphasize the fact that k is changing to $-k$ when going through the cut with an infinitesimal change of ω.

The jump of the GF Eq. (B.28) can be evaluated in the general case by using

the explicit form of the GF,

$$g(z,z') = \frac{E_L(z_<)E_R(z_>)}{E_L\dot{E}_R - \dot{E}_L E_R}\,, \tag{B.29}$$

in terms of the "left" and "right" functions, $E_L(z)$ and $E_R(z)$, respectively. These are solution of the homogeneous wave equation (B.19) and the left or right outgoing boundary condition. More explicitly, they are given by

$$E_L(z) = \begin{cases} e^{-ikz}, & z < -a, = \\ B_+ f_+(z) + B_- f_-(z), & |z| < a \end{cases} \tag{B.30}$$

and

$$E_R(z) = \begin{cases} C_+ f_+(z) + C_- f_-(z), & |z| < a \\ e^{ikz}, & z > a \end{cases} \tag{B.31}$$

in terms of $f_+(z;\omega)$ and $f_-(z;\omega)$, two arbitrary linearly independent solutions of Eq. (B.19) within the slab. While these functions (depending on ω) do not change when changing the sign of k, the coefficients $B_\pm$ and $C_\pm$ do modify, leading to non-vanishing contributions to the jump Δg of the GF across the cuts. Here in Eq. (B.29), $z_< = \min(z,z')$ and $z_> = \max(z,z')$, and the derivative

$$\dot{E}(z) \equiv \frac{1}{\mu(z)}\partial_z E(z) \tag{B.32}$$

is introduced for convenience.

Now, choosing the functions $f_\pm(z)$ in such a way that

$$f_+(a)f_-(a) + f_+(-a)f_-(-a) = 0\,, \tag{B.33}$$

$$\dot{f}_+(a)\dot{f}_-(a) + \dot{f}_+(-a)\dot{f}_-(-a) = 0\,, \tag{B.34}$$

$$f_+(-a)\dot{f}_+(a) + f_+(a)\dot{f}_+(-a) = 0\,, \tag{B.35}$$

$$f_-(-a)\dot{f}_-(a) + f_-(a)\dot{f}_-(-a) = 0\,, \tag{B.36}$$

which can always be fulfilled, for any profiles of $\varepsilon(r)$ and $\mu(r)$. We obtain, after simple algebra, a convenient form of the cut integrand

$$-\frac{1}{2\pi i}\Delta g(z,z';\omega) = \sum_{s=\pm} \sigma_s f_s(z) f_s(z')\,, \tag{B.37}$$

where

$$\sigma_s(\omega) = \frac{1}{\pi}\,\frac{k}{\dot{f}_s^2(a) + \dot{f}_s^2(-a) + k^2[f_s^2(a) + f_s^2(-a)]}\,. \tag{B.38}$$

This form allows us to include the contribution of the cuts on equal footing with the RSs, treating the cuts as continua of poles of the GF:

$$\begin{aligned} g(z,z') &= \sum_n \frac{E_n(z)E_n(z')}{\omega_n(\omega-\omega_n)} \\ &\quad + \sum_{s=\pm}\sum_{s'=\pm}\int_{s'p}^{s'p-i\infty} \frac{E_s(z;\omega')E_s(z';\omega')}{\omega'(\omega-\omega')}d\omega' \\ &\equiv \sum\!\!\!\!\!\!\int_n \frac{E_n(z)E_n(z')}{\omega_n(\omega-\omega_n)}\,, \end{aligned} \tag{B.39}$$

where

$$E_s(z;\omega) = \sqrt{\omega\sigma_s(\omega)}f_s(z;\omega)\,. \tag{B.40}$$

Note that in Eqs. (B.38), (B.39), and (B.40), we have added ω to the arguments of E_s, σ_s, and f_s, earlier omitted for brevity of notations, in order to emphasize their frequency dependence.

Appendix C

GF for a homogeneous slab

Consider a dielectric slab in vacuum, having thickness $2a$ and constant permittivity and permeability. Their profiles in space are described by

$$\varepsilon(z) = 1 + (\epsilon - 1)\Theta(a - |z|)\,, \tag{C.1}$$

$$\mu(z) = 1 + (\mu - 1)\Theta(a - |z|)\,. \tag{C.2}$$

Within the slab ($|z|$, $|z'| \leqslant a$) the GF has the form

$$g(z, z') = -\frac{\mu}{2iq}\frac{\varphi(z_<)\varphi(-z_>)}{1 - \xi^2}\,, \tag{C.3}$$

see Eq. (B.29) in which, due to the mirror symmetry, the left and right solutions are given by the same function, $E_L(z) = E_R(-z) = \varphi(z)$, with

$$\varphi(z) = e^{iqz} + \xi e^{-iqz}\,, \tag{C.4}$$

$$\xi = \frac{1+\eta}{1-\eta}e^{-2iqa}\,, \qquad \eta = \frac{\mu k}{q}\,, \tag{C.5}$$

$$q^2 = \epsilon\mu\omega^2 - p^2\,, \qquad k^2 = \omega^2 - p^2\,. \tag{C.6}$$

Clearly, the GF has poles at $\xi = \pm 1$, determining secular equation for the RS frequencies ω_n:

$$(q_n + \mu k_n)e^{-iq_n a} = (-1)^n (q_n - \mu k_n)e^{iq_n a}\,. \tag{C.7}$$

The RS wave functions, which are the solutions of Eq. (B.7), are given by

$$E_n(z) = \begin{cases} A_n e^{ik_n z} & z > a \\ B_n(e^{iq_n z} + (-1)^n e^{-iq_n z}) & |z| \leqslant a \\ (-1)^n A_n e^{-ik_n z} & z < -a \end{cases} \tag{C.8}$$

with the continuity condition $A_n = B_n(e^{iq_n a} + (-1)^n e^{-iq_n a})e^{-ik_n a}$. The eigenvalues k_n and q_n are related to the eigenfrequency ω_n via Eq. (C.6), and the normalisation constants B_n found from Eq. (B.16) have the following explicit form:

$$B_n^{-2} = 8(-1)^n \left[\epsilon a + \frac{ip^2(\epsilon\mu - 1)}{k_n(q_n^2 - \mu^2 k_n^2)}\right]\,. \tag{C.9}$$

For the cuts of the GF in the complex ω plane, the functions satisfying Eqs. (B.33)–(B.36) are given by

$$f_\pm(z) = e^{iqz} \pm e^{-iqz} \tag{C.10}$$

within the slab $|z| \leqslant a$. They possess a definitive parity ($s = \pm 1$) due to the mirror symmetry of the system, and the same form as the RS wave functions Eq. (C.8). According to Eq. (B.38), the cut density functions are given by

$$\sigma_\pm(\omega) = \frac{1}{4\pi}\frac{\mu^2 k}{(\mu^2 k^2 - q^2)\cos(2qa) \pm (\mu^2 k^2 + q^2)}\,. \tag{C.11}$$

C.1 GF in k-representation

Using the Newton-Raphson method, we have solved the secular equation Eq. (C.7) and found all the RS wave numbers in a selected frequency range (within a circle of radius $\omega_{\max}$ in the complex frequency plane). The RSs include four categories of modes: WG modes, anti-WG modes, FP modes, and a leaky mode (LM). The WG and anti-WG modes are present only if $p \neq 0$. We then use the ML expansion Eq. (B.13) in the k-representation which includes all types of modes in the summation and compare it with the analytic GF given by Eq. (C.3)

Results for a slab with $\epsilon = 6$ and $\mu = 1$ are shown in Fig. C.1 for $z = -z' = a/2$. We see that all partial contributions to the GF due to each type of modes is non-vanishing, including that of the LM which has $\mathrm{Re}\,\omega_n = 0$ and which is discussed in detail in [14,15]. Summing up all the contributions to the ML series Eq. (B.13) results in values of the GF approaching its analytic form Eq. (C.3). By increasing $\omega_{\max}$, we increase the number of RSs N included in the series Eq. (B.13), in this way making the ML representation more and more accurate (see Fig. C.1(b)). The inset demonstrate the convergence of the ML series to the exact solution, with the error scaling as $1/N^2$.

C.2 GF in ω-representation

The GF can also be represented as a function of frequency. However, the square root in Eq. (B.25) causes branch cuts at $\omega = \pm p$, which separates the frequency plane into two Riemann sheets with modes split across both sheets. Only the modes found on one of the sheets are taken into account. This is chosen to be the "physical" sheet, on which the WG and FP modes are found, while anti-WG modes and the leaky mode turn out to be on the other, unphysical sheet and are thus excluded from the ML expansion Eq. (B.39). Figure C.2 shows

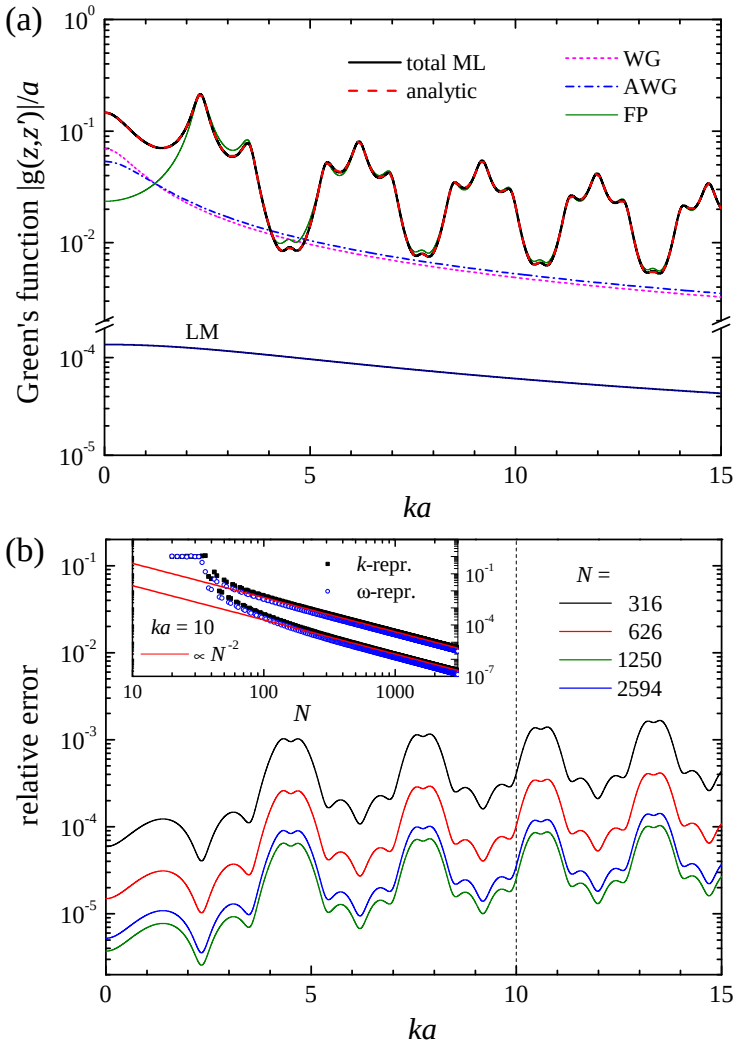

Figure C.1: (a) Green's function $g(z, z')$ of a homogeneous dielectric slab in vacuum, with $\epsilon = 6$, calculated for $pa = 5$, $z = a/2$, and $z' = -a/2$ as a function k, the normal component of the wave number in vacuum. Partial contributions of WG, anti-WG (AWG), FP modes and a leaky mode (LM) are shown along with the sum of all the contributions and the analytic values of the GF. (b) Relative error of the GF calculated via Eq. (B.13) as compared to its analytic values Eq. (C.3), for different number of modes N included in the ML series. The inset shows the relative error for $ka = 10$ (marked by vertical dashed lines in Figs. C.1(b) and C.2(b)) as a function of the basis size N.

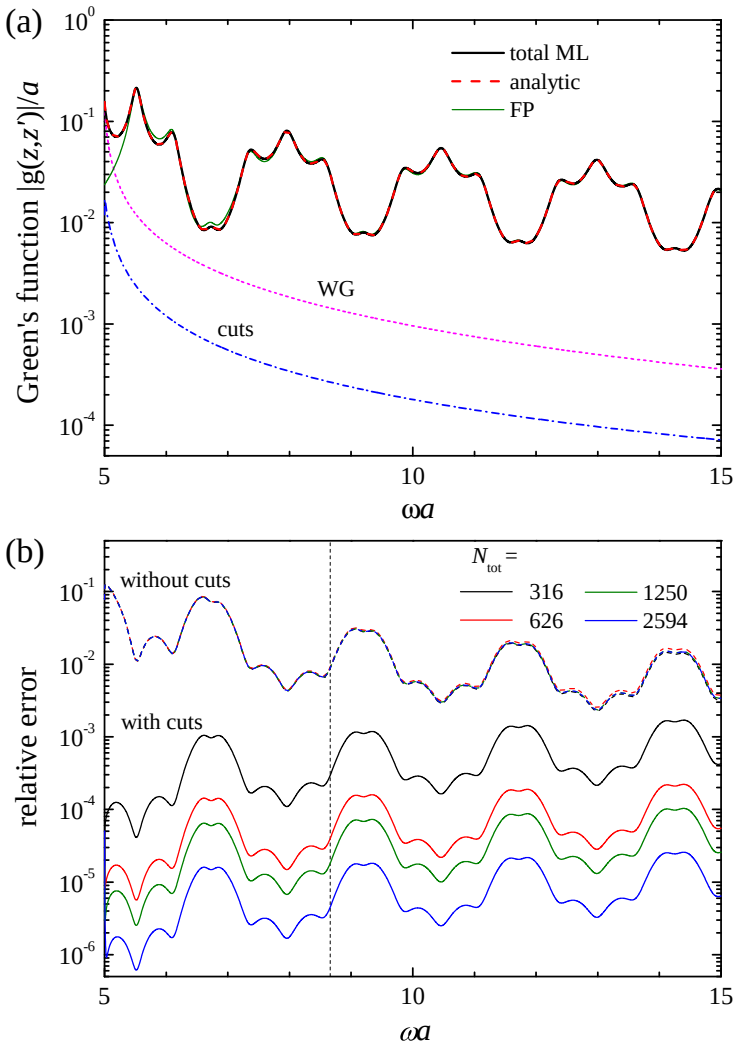

Figure C.2: (a) As Fig. C.1(a) but in the ω-representation, in which the AWG modes and the LM do not contribute to the ML expansion Eq. (B.39), but there is instead an additional component due to the cuts. (b) Relative error of the GF calculated via Eq. (B.39) as compared to its analytic values Eq. (C.3), for different number of modes N included in the ML series, with and without contribution of the cuts.

a comparison, for the same parameters as in Fig. C.1, of the ML expansion Eq. (B.39) with the analytic solution Eq. (C.3), again showing different contributions, including WG, FP modes, and the cuts. We see that the ML series in the ω-representation again converges to the exact solution, provided that the cut integrals are included. Note also that the convergence is very similar to that in the k-representation, as it is clear from the inset in Fig. C.1(b). In fact, in both cases the error alternates between two different boundaries but nevertheless decreases with the basis size as N^{-2}.

Appendix D

RSE applied to a homogeneous dielectric slab

Here, we demonstrate how the RSE in the k and ω representations is applied to a homogeneous perturbation. This is a special case of the PC-RSE which allows an exact analytic solution, but obviously lacking any periodic modulations. We use $\alpha = \Delta\epsilon$ and $\beta = 0$ in Eq. (3.12). The perturbation of the permittivity thus has the form

$$\Delta\varepsilon(z) = \Delta\epsilon\Theta(b - |z|)\,. \tag{D.1}$$

The perturbed system presents a core-shell slab consisting of three homogeneous regions. The secular equation for this system has the following analytic form:

$$(\gamma_+\lambda_- - \gamma_-\lambda_+)\,e^{iq_1 b} \pm (\gamma_+\lambda_+ - \gamma_-\lambda_-)\,e^{-iq_1 b} = 0\,, \tag{D.2}$$

where $\gamma_\pm = (q \pm k)e^{\mp iq(a-b)}$, $\lambda_\pm = q \pm q_1$, and $q_1 = \sqrt{\epsilon_1\omega^2 - p^2}$ with $\epsilon_1 = \epsilon + \Delta\epsilon$. The secular equation (C.7) for the homogeneous slab can be restored by setting $b = a$ and $q = q_1$, or simply $b = 0$.

D.1 RSE in k-representation

In the k-representation, the RSE equation for treating planar homogeneous systems is given by Eq. (22) of [14], which we write here as

$$k \sum_{n'} \left(\delta_{nn'} + \mathcal{V}_{nn'} \right) c_{n'} = \sum_{n'} \left(k_n \delta_{nn'} - \frac{p^2}{k_n} \mathcal{V}_{nn'} \right) c_{n'} \,, \tag{D.3}$$

with the matrix elements $\mathcal{V}_{nn'} = V^{00}_{nn'}$ given by Eq. (3.13) for $g = g' = 0$.

Its application to the perturbation given by Eq. (D.1) is shown in Fig. D.1, in comparison with the exact solution Eq. (D.2) and the basis RSs of the homogenous slab. The quasiperiodic pattern of the wave numbers of the perturbed RSs seen in Fig. D.1 is caused by the perturbation covering only the middle half of the slab, so that the original homogeneous slab of thickness $2a$ is now split into three subsystems of thickness $a/2$, a, and $a/2$, each acting as a resonance cavity. The distance in frequency between the modes is given by a fundamental period of $\pi/(2a\sqrt{\epsilon})$ as in the basis cavity, but the cavities between $-a$ and $-b$ and between b and a have caused additional quasiperiodicities, one of them having the period of $\pi/[(a-b)\sqrt{\epsilon}]$, which for $b = a/2$ is four times larger than the fundamental period. Other cavities present in the system also contribute to the rich spectrum of RSs seen in Fig. D.1.

Looking at the relative error shown in Figs. D.1(b) and (c), we see that the RSE in the k-representation quickly converges to the exact solution. The relative error scales as $1/N^3$, which is typical for effective 1D systems, see [10–14].

D.2 RSE in ω-representation

The RSE equation in this case is given by the general formula Eq. (2.23) of the PC-RSE, but since this is a homogeneous perturbation, there is no mixing of channels, so we use again $g = g' = 0$. Also, Eq. (2.23) includes the contribution

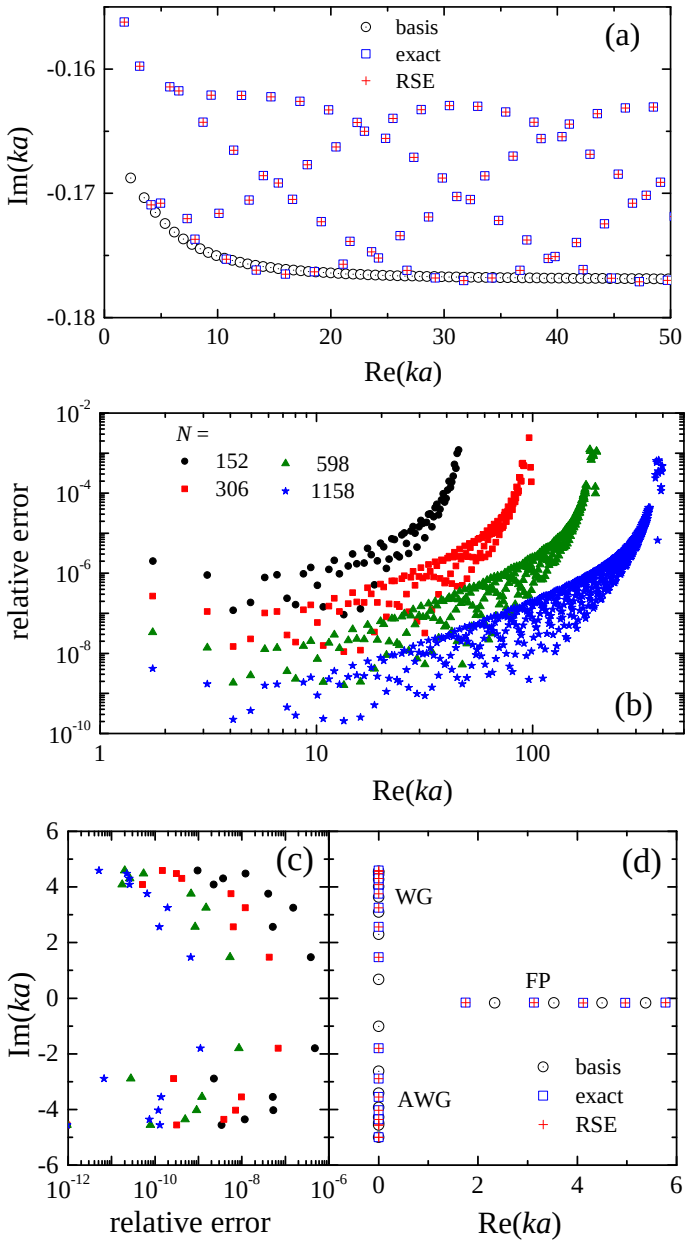

Figure D.1: (a) Wave numbers k_n of the FP modes calculated for $pa = 5$ using the RSE in the k-representation (red crosses) for the core-shell dielectric slab with $\epsilon = 6$, $\Delta\epsilon = 1$, and $b = a/2$, along with the exact solution (blue squares) and the basis RSs (black circles with dots). (b) Relative error for the wave numbers of the FP modes compared to the exact solution, for different basis sizes as given. (c) Relative errors for WG and anti-WG modes, for the same basis sizes as in (b). (d) As (a) but for all WG and anti-WG modes, and the first few FP modes.

of the cuts which need to be discretized, giving rise to cut modes to be used in the RSE on equal footing with the RSs. This procedure is described in Ch 2.3.

Like with k-representation, we can use a different form of the RSE equation due to the homogeneous perturbation which discards the index g from Eq. (2.30) and uses the diagonal matrix $\mathcal{V}_{\bar{n}\bar{n}'} = V^{00}_{\bar{n}\bar{n}'}$ (where we use $\bar{n}$ to include the cut modes):

$$\omega \sum_{\bar{n}'} \left(\delta_{\bar{n}\bar{n}'} + \mathcal{V}_{\bar{n}\bar{n}'}\right) c_{\bar{n}'} = \omega_{\bar{n}} c_{\bar{n}} \,. \tag{D.4}$$

Figure D.2(a) shows the RS frequencies calculated using the RSE equation (D.4), with and without cut modes in the basis. The unperturbed RSs and even- and odd-parity cut modes of the basis are also shown. The distribution of perturbed RSs repeats the oscillatory pattern seen in Fig. D.1(a) and discussed above. The RSE frequencies match well the analytic values given by Eq. (D.2) even if the cut modes are not taken into account. In fact, in this case the relative error is still rather low, as can be seen in Fig. D.2(b). Obviously, it is higher for the modes which are close to cut and does not improve for these modes with increasing N, the number of the RSs in the basis. Including the cut modes in the RSE results in a relative error scales as $1/N^3$, almost uniformly for all the RSs, which is essentially the same as in the RSE used in the k-representation.

The total number of modes in the basis is given by $N_{\rm tot} = N + 4N_c = (1 + F)N$, where we have introduced the factor F, the ratio of the number of cut modes to the number of RSs included. In Fig. D.2(c) we show how the error depends on F for a fixed $N_{\rm tot}$. Higher values of F imply more cut modes included in the basis at the expense of RSs. It is clear that larger values of F give generally lower errors for the RSs close to the cut. However, modes with larger frequencies away from the cut are less accurately determined in this case, as the number of basis RSs N reduces with F. We found that the value $F = 1$ is close to the optimal one, as all RSs in a wide spectral range have a similar

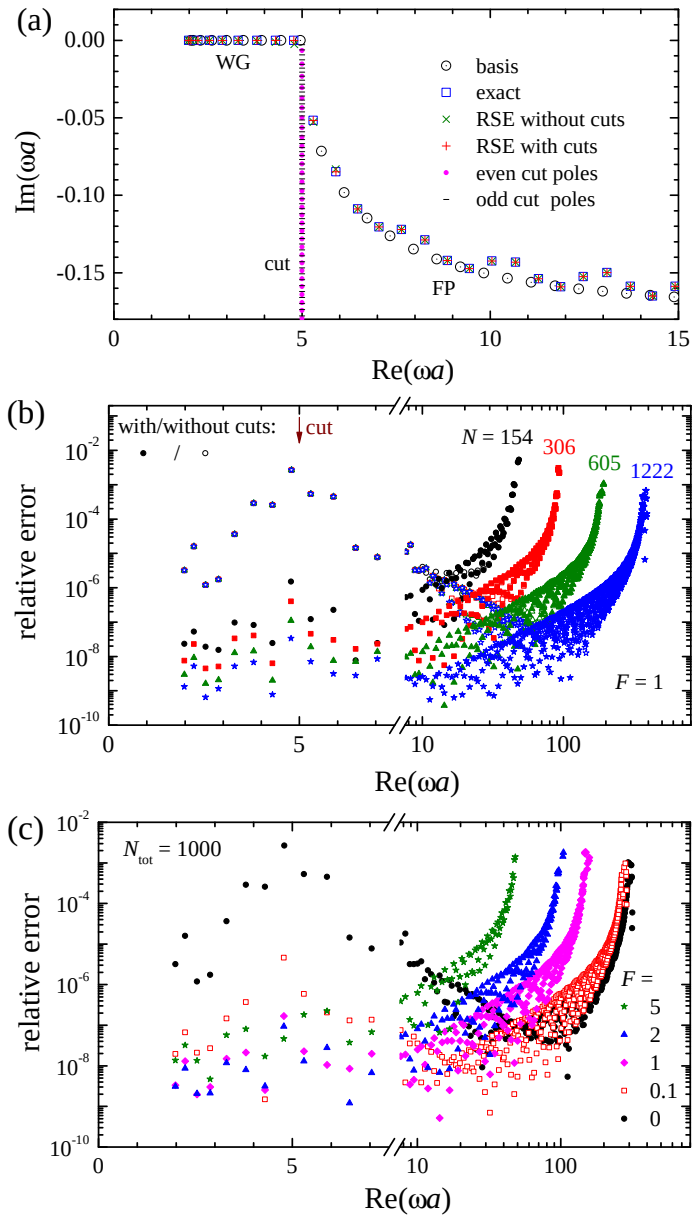

Figure D.2: (a) As Fig. D.1 but in frequency representation, also showing even and odd parity cut modes. (b) Relative errors compared to the exact solution Eq. (D.2) of the RS frequencies calculated using the RSE, with and without cut modes in the basis and for different basis sizes as given. (c) Relative error of the RSE results calculated for a fixed basis size $N_{\text{tot}} = 1000$ and different values of F, the ratio of the number of cut modes to the number of RSs in the basis.

level of errors. We have made a similar study of the relative error in the case of the PC-RSE and found the same optimal value of F. Therefore, unless stated differently, the value of $F = 1$ is used in all calculations throughout this thesis.

Appendix E

Other Mode Contributions

In addition to Fig. 4.3 of the main text, showing the expansion coefficients for a BIC-QGM pair, Figs. E.1 and E.2 show basis mode contributions for three other types of modes: FP, leaky, and cut modes. Similar to the BIC-QGM pair in Fig. 4.3, two perturbed FP RSs in Fig. E.1 originate from a pair of degenerate unperturbed FP modes, and only one of them has a nonzero contribution of $m = 0$ leaky modes. This makes the Q-factor for that mode slightly lower than for the other one, not affected by any $m = 0$ modes due to symmetry. Interestingly, both perturbed modes are almost equally strongly influenced by a pair of FP and a pair of WG basis modes matching the perturbed mode frequency.

Like in Fig. 4.3, the leaky and cut modes shown in Fig. E.2 have a dominant contribution of only one basis mode (or one pair of modes), while the contribution of any other mode in the basis does not exceed a few per thousand.

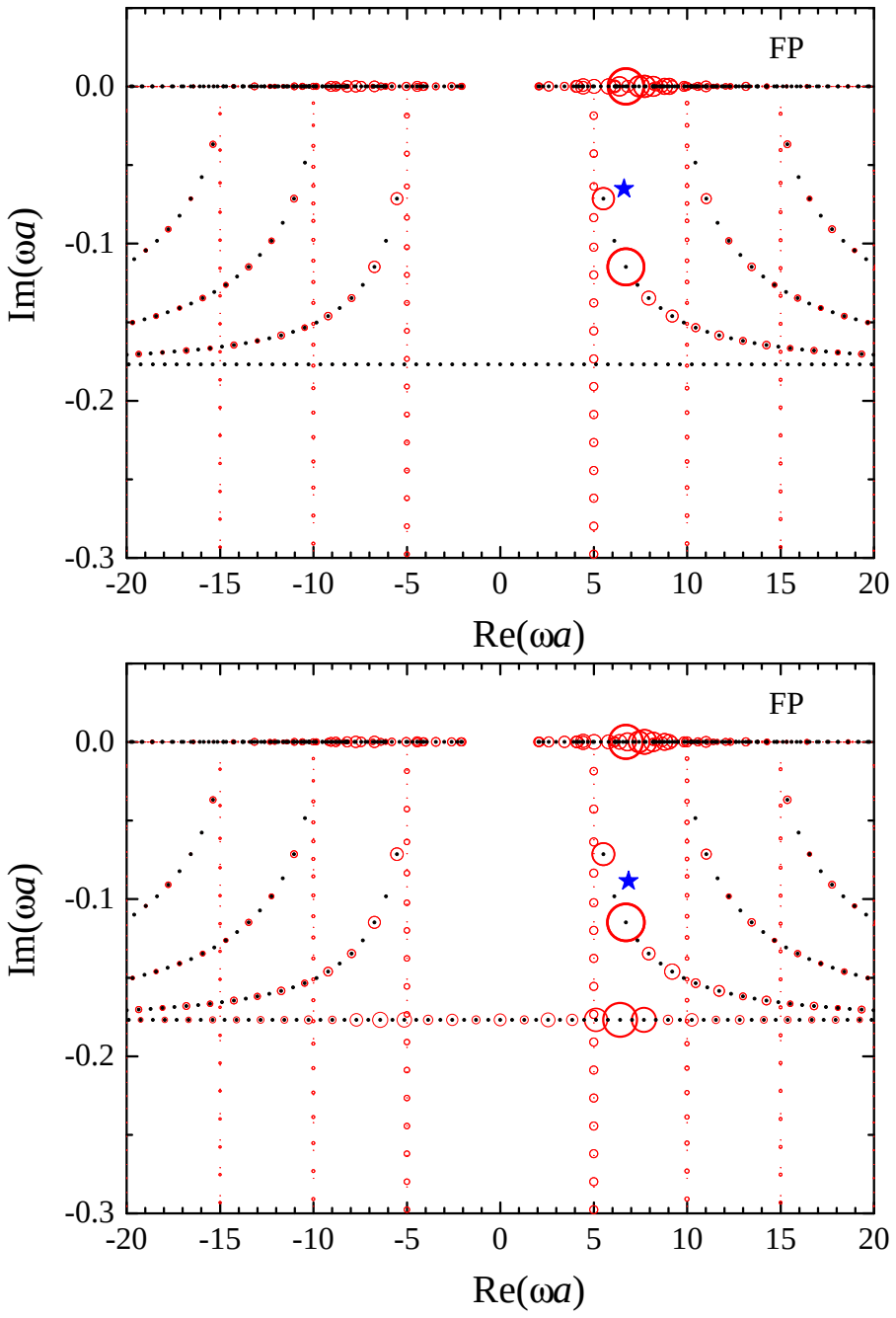

Figure E.1: As Fig. 4.3 but for two RSs originating from a degenerate pair of FP modes.

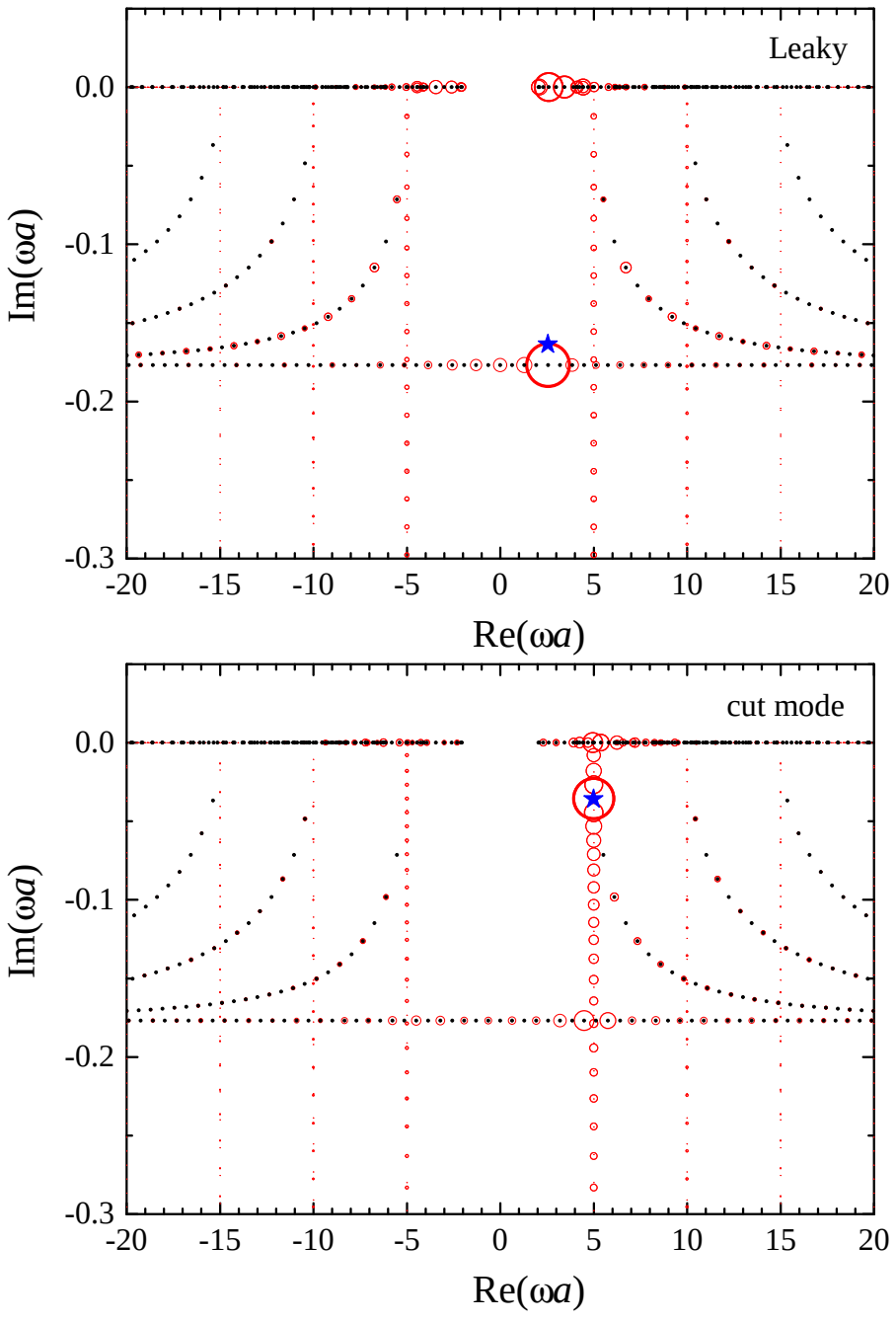

Figure E.2: As Fig. 4.3 but for a RS coming from a non-degenerate $m = 0$ leaky mode (top) and for a perturbed cut mode (bottom).

Appendix F

Scattering Matrix Method

In this thesis the scattering matrix method is used as an established method [6, 87, 88] with which we compare the RSE results. Below we describe this method, providing details of how it was applied to the studies system.

We want to find the RSs for a dielectric system in TE polarisation which has a photonic crystal core which has a periodic permittivity along the slab, in the x-direction. These RSs are poles of the scattering matrix (S-matrix). We therefore calculate the S-matrix.

Since the permittivity is periodic in the x direction within the slab, it can be represented by a Fourier series:

$$\epsilon(x) = \sum_g \epsilon_g e^{igx}, \qquad \epsilon_g = \frac{1}{d}\int_{x_0}^{x_0+d} \epsilon(x) e^{-igx} dx, \tag{F.1}$$

where g are vectors: $2\pi n/d$ where d is the period of the permittivity and $n = 0, \pm 1, \pm 2...$ The electric field within the slab can in turn be represented by a

Bloch wave:

$$E(x,z) = e^{iqz}e^{ipx}u_p(x), \qquad u_p(x) = \sum_g u_{g,p}e^{igx}, \tag{F.2}$$

where p is the x-direction wavevector which will remain fixed, q is the z-direction wavevector within the slab and $u_p(x)$ is a periodic function that has the same period as the permittivity.

Using these equations together, MWE becomes the central equation:

$$((p+g)^2 - q^2)u_{g,p} + \sum_{g'} \omega^2 \epsilon_{g-g'} u_{g',p} = 0, \tag{F.3}$$

which shows that the periodic permittivity has caused all of the g vectors to be mixed through the $\epsilon_{g-g'}$ term. This mixing is what prevents easily obtainable solutions for the RSs, necessitating the use of the scattering matrix method.

Due to this mixing, the z-direction wavevector, q does not have a simple form as in the homogeneous case but Eq. (F.3) can be represented as an eigenvalue equation for q:

$$\sum_{g'} \hat{M}_{gg'}\mathbf{u}_g = q_g^2 \mathbf{u}_g, \qquad \hat{M}_{gg'} = \omega^2\epsilon_{g-g'} - \delta_{gg'}(p+g)^2. \tag{F.4}$$

where $\mathbf{u}_g$ are the eigenvectors. For homogeneous systems, the index g disappears and the eigenvalue simplifies to the familiar $q = \sqrt{\varepsilon\omega^2 - p^2}$.

To derive the scattering matrix, we first define the transfer matrices which translate incoming and outgoing wave amplitudes on one side of a interface (e.g a vacuum) to the other side (e.g within the slab). There are five layers in this system: vacuum $\rightarrow$ homogeneous slab$\rightarrow$ photonic crystal$\rightarrow$ homogeneous slab$\rightarrow$ vacuum.

A transfer matrix, $\hat{T}$ is defined such that:

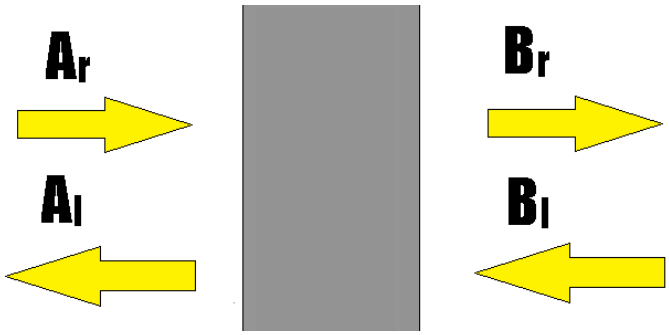

Figure F.1: Visualisation of the wave amplitudes entering and leaving a system.

$$\begin{pmatrix} B_r \\ B_l \end{pmatrix} = \hat{T}_{1\to 2} \begin{pmatrix} A_r \\ A_l, \end{pmatrix} \tag{F.5}$$

where A_r and A_l are the right and left wave amplitudes respectively in region 1 and B_r and B_l are the right and left wave amplitudes respectively in region 2. The amplitudes $A - r$, A_l, B_r and B_l are shown in Fig. F.1 to demonstrate the layout. Due to the scattering from the periodic permittivity, there are infinitely many wave amplitudes, but our calculations will clearly need to be confined to some finite number of channels so that g ranges from $-2\pi M/d$ to $2\pi M/d$ resulting in $2M + 1$ wave amplitudes (represented by letters with arrows) and a $4M + 2$ transfer matrix (represented by calligraphic letters)

$$\begin{pmatrix} \vec{B}_r \\ \vec{B}_l \end{pmatrix} = \mathcal{T}_{1\to 2} \begin{pmatrix} \vec{A}_r \\ \vec{A}_l \end{pmatrix} \tag{F.6}$$

The transfer matrices for each interface are given by:

$$\mathcal{T}_{1\to 2} = \begin{pmatrix} \hat{I} & \hat{I} \\ \hat{I}\hat{k} & -\hat{I}\hat{k} \end{pmatrix}^{-1} \begin{pmatrix} \hat{U} & \hat{U} \\ \hat{U}\hat{q} & -\hat{U}\hat{q} \end{pmatrix}, \tag{F.7}$$

$$\mathcal{T}_{2\to3} = \begin{pmatrix} \hat{U} & \hat{U} \\ \hat{U}\hat{q} & -\hat{U}\hat{q} \end{pmatrix}^{-1} \begin{pmatrix} \hat{U}_1 & \hat{U}_1 \\ \hat{U}_1\hat{q}_1 & -\hat{U}_1\hat{q}_1 \end{pmatrix}, \tag{F.8}$$

$$\mathcal{T}_{3\to4} = \begin{pmatrix} \hat{U}_1 & -\hat{U}_1 \\ \hat{U}_1\hat{q}_1 & \hat{U}_1\hat{q}_1 \end{pmatrix}^{-1} \begin{pmatrix} \hat{U} & \hat{U} \\ \hat{U}\hat{q} & -\hat{U}\hat{q} \end{pmatrix}, \tag{F.9}$$

and

$$\mathcal{T}_{4\to5} = \begin{pmatrix} \hat{U} & \hat{U} \\ \hat{U}\hat{q} & -\hat{U}\hat{q} \end{pmatrix}^{-1} \begin{pmatrix} \hat{I} & \hat{I} \\ \hat{I}\hat{k} & -\hat{I}\hat{k} \end{pmatrix}, \tag{F.10}$$

where $\hat{I}_{ij} = \delta_{ij}$ is an identity matrix, $\hat{U}_{gj} = (\mathbf{u}_g)_j$, $\hat{k}_{gg'} = \delta_{gg'}k_g$ are the z-direction wavevectors in the vacuum where $k_g = \sqrt{\omega^2 - (p+g)^2}$, $\hat{q}_{gg'} = \delta_{gg'}q_g$ are the z-direction wavevectors in the homogeneous region and $\hat{q}_{1gg'} = \delta_{gg'}q_{1g}$ are the z-direction wavevectors in the photonic crystal region.

The initial formulation of the transfer matrix in Eq. (F.5) described a 2×2 matrix. Due to the scattering of the photonic crystal slab, each of the matrix elements are themselves $2M + 1$ square matrices so that $\mathcal{T}_{ij}$ refers to the $i \times j$ block.

The transfer matrix maps wave amplitudes from one side of the system to the other (A_l, $A_r \to B_l$, B_r). By contrast, the scattering matrix maps incoming waves to outgoing waves (A_r, $B_l \to A_l$, B_r), see Fig. F.1.

We translate outgoing to incoming waves: [7]:

$$\begin{pmatrix} \hat{A}_r \\ \hat{B}_l \end{pmatrix} = \mathcal{S}_{1\to2} \begin{pmatrix} \hat{A}_l \\ \hat{B}_r \end{pmatrix} \tag{F.11}$$

The scattering matrix can be built layer by layer through propagation and interface transformations.

Suppose that we have a ray of light travelling through a material which is homogeneous in the direction of travel. The scattering matrix is initially labelled $\mathcal{S}_0 = \mathcal{I}$ where $\mathcal{I}_{ij} = \delta_{ij}$. The next stage of the iteration can be one of two cases, either the light propagates through a layer with some permittivity or it encounters a new layer with a different permittivity. For the former case the S-matrix is iterated as:

$$\mathcal{S}_{n+1} = \begin{pmatrix} \hat{Q} & \hat{O} \\ \hat{O} & \hat{I} \end{pmatrix} \mathcal{S}_n \begin{pmatrix} \hat{I} & \hat{O} \\ \hat{O} & \hat{Q} \end{pmatrix}, \tag{F.12}$$

where $\hat{Q}_{ij} = \delta_{ij} \exp(iq_j a)$, $\hat{I}_{ij} = \delta_{ij}$, $\hat{O}_{ij} = 0$.

For the latter case, the S-matrix is iterated as:

$$\mathcal{S}_{n+1} = \begin{pmatrix} \hat{J}\mathcal{S}_{11} & \hat{J}\hat{K} \\ \mathcal{S}_{21} + \mathcal{S}_{22}\mathcal{T}_{22}\hat{J}\mathcal{S}_{11} & \mathcal{S}_{22}\mathcal{T}_{21}\hat{J}\hat{K} + \mathcal{S}_{22}\mathcal{T}_{22} \end{pmatrix}, \tag{F.13}$$

where $\hat{J} = (\mathcal{T}_{11} - \mathcal{S}_{12}\mathcal{T}_{21})^{-1}$, $\hat{K} = \mathcal{S}_{12}\mathcal{T}_{22} - \mathcal{T}_{12}$ and $\mathcal{S}_{ij}$ is a $2M+1$ matrix and is the $i \times j$ block element of $\mathcal{S}_n$. This process can be repeated to add any number of layers and interfaces.

The RSs are defined with outgoing boundary conditions only i.e there are no inputs:

$$\mathcal{S}^{-1}\mathbb{A}_{\text{out}} = 0, \tag{F.14}$$

where $\mathbb{A}_{\text{out}} = (\vec{A}_l, \vec{B}_r)$ is a $4M+2$ vector containing outgoing wave amplitudes.

By ignoring the trivial solution of $\mathbb{A}_{out} = 0$, the conditions for resonant states is given by $\det \mathcal{S}(\omega)^{-1} = 0$, i.e the poles of the scattering matrix. This can be found by simply calculating the determinant for each frequency and using the Newton-Raphson method for finding roots, however, the S-matrix is very large for large M which means that the determinant can become unstable simply due

to the size of the matrix. To prevent this, the matrix can be decomposed into its singular values as described in the supplementary material of [26]. This method begins by approximating the matrix as such:

$$\mathcal{S}(\omega) = \mathcal{S}_{BG}(\omega) + \mathcal{L}(\omega I - \Omega_p)^{-1}\mathcal{R}, \tag{F.15}$$

where $\mathcal{S}_{BG}(\omega)$ is the background scattering matrix terms which is assumed to change slowly with ω, Ω_p is a diagonal matrix containing the poles ω_n and I is the unit matrix. The matrices $\mathcal{L}$ and $\mathcal{R}$ are such that $\mathcal{LR}$ forms the residue of the scattering matrix at $\omega = \omega_n$.

Taking the derivative of (F.15) produces:

$$\mathcal{S}'(\omega) \approx -\mathcal{L}(\omega I - \Omega_p)^{-2}\mathcal{R}, \tag{F.16}$$

where the background term has vanished due to the slow dependency on ω. By taking the inverse,

$$\left[\mathcal{S}'(\omega)\right]^{-1} = -\mathcal{R}^{-1}(\omega I - \Omega_p)^2\mathcal{L}^{-1}, \tag{F.17}$$

and multiplying with (F.15), we obtain:

$$\left[\mathcal{S}'(\omega)\right]^{-1}\mathcal{S}(\omega) \approx \mathcal{R}^{-1}(\omega I - \Omega_p)\mathcal{R}. \tag{F.18}$$

Where ω has been taken to be close to the poles so that the background term becomes negligible. This has produced an eignvalue equation for $(\omega I - \Omega_p)$ with $\mathcal{R}^{-1}$ as the eigenvector. However, the scattering matrix is arbitrary in size since it is a square matrix of size $(2M+1)(2M+1)$ for any positive integer M. For large M, the eigenvalues can become unstable since the determinant of the matrix is approaching infinity. To avoid this, the matrix can instead

be decomposed into singular values: $\mathcal{S}' = \mathcal{U}\Sigma\mathcal{V}^\dagger$ where $\mathcal{U}$ and $\mathcal{V}$ are unitary matrices and Σ is a diagonal matrix of the singular values of $\mathcal{S}'$. Inserting this into (F.18) results in:

$$\Sigma^{-1}\mathcal{U}^\dagger\mathcal{S}\mathcal{V}\mathbf{v} = (\omega I - \Omega_p)\mathbf{v}. \tag{F.19}$$

We now have an eigenvalue equation which is more stable for larger matrices where the eigenvalues are a diagonal matrix made up of $\omega - \omega_n$ which gives the distance from the input frequency, ω, to all the poles in the system contained in Ω_p. However, we cannot use this to simply find Ω_p since we have made the assumption in Eq. (F.15) that the scattering matrix is made up of it's poles on top of a slow moving background term which may not be the case over long distances. We also made the assumption in Eq. (F.18) that the frequency ω is close to a pole which allowed us to neglect the background term. Instead, we use Eq. (F.19) as an iterative method starting with some guess value for a pole, ω_0. The eigenvalues will then be the distances to all nearby poles. We choose the smallest value of $|(\omega_0 - \omega_n)|$ i.e the distance to the nearest pole and use that as the next guess value, ω_1 and repeat the process until one of the values in Ω_p is sufficiently close to zero.

Bibliography

[1] J. M. Liu, Liu and Pu, Minhao and Yvind, Kresten and Hvam, "*High-efficiency, large-bandwidth silicon-oninsulator grating coupler based on a fullyetched photonic crystal structure*," Appl. Phys. Lett., **96**, 051126 (2010).

[2] S. J. Mcnab, N. Moll, and Y. A. Vlasov, "*Ultra-low loss photonic integrated circuit with membrane-type photonic crystal waveguides*," Opt. Soc., **299**, 358–362 (2003).

[3] A. R. Mcgurn, "*Photonic crystal circuits: A theory for two- and three-dimensional networks*," Phys. Rev. B, **61**, 13235 (2000).

[4] E. Bayindir, Mehmet and Temelkuran, B. and Ozbay, "*Photonic-crystal-based beam splitters*," Appl. Phys. Lett., **77**, 3902 (2000).

[5] E. Yablonovitch, T. J. Gmitter, and K. M. Leung, "*Photonic band structure: The face-centered-cubic case employing nonspherical atoms*," Phys. Rev. Lett., **67**, 2295 (1991).

[6] D. M. Whittaker and I. S. Culshaw, "*Scattering-matrix treatment of patterned*," Phys. Rev. B, **60** 2610 (1999).

[7] S. G. Tikhodeev, A. L. Yablonskii, E. A. Muljarov, N. A. Gippius, and T. Ishihara, "*Quasiguided modes and optical properties of photonic crystal slabs*," Phys. Rev. B, **66** 045102 (2002).

[8] S. Fan and J. D. Joannopoulos, "*Analysis of guided resonances in photonic crystal slabs*," Phys. Rev. B, **65**, 235112 (2002).

[9] W. Zhou, D. Zhao, Y.-C. Shuai, H. Yang, S. Chuwongin, A. Chadha, J.-H. Seo, K. X. Wang, V. Liu, Z. Ma, and S. Fan, "*Progress in 2d photonic crystal fano resonance photonics*," Prog. Quant. Elec., **38** 1–74 (2014).

[10] M. B. Doost, W. Langbein, and E. A. Muljarov, "*Resonant-state expansion applied to planar open optical systems*," Phys. Rev. A, **85**, 023835 (2012).

[11] M. B. Doost, W. Langbein, and E. A. Muljarov, "*Resonant state expansion applied to two-dimensional open optical systems*," Phys. Rev. A, **87**, 043827 (2013).

[12] M. B. Doost, W. Langbein, and E. A. Muljarov, "*Resonant-state expansion applied to three-dimensional open optical systems*," Phys. Rev. A, **90**, 013834 (2014).

[13] E. A. Muljarov, W. Langbein, and R. Zimmermann, "*Brillouin-wigner perturbation theory in open electromagnetic systems*," Europhys. Lett., **92**, 50010 (2010).

[14] L. J. Armitage, M. B. Doost, W. Langbein, and E. A. Muljarov, "*Resonant-state expansion applied to planar waveguides*," Phys. Rev. A, **89**, 053832 (2014).

[15] L. J. Armitage, M. B. Doost, W. Langbein, and E. A. Muljarov, "*Erratum: Resonant-state expansion applied to planar waveguides*," Phys. Rev. A, **97**, 049901 (2018).

[16] S. V. Lobanov, G. Zoriniants, W. Langbein, and E. A. Muljarov, "*Resonant-state expansion of light propagation in nonuniform waveguides*," Phys. Rev. A, **95**, 053848 (2017).

[17] P. Lalanne and E. Silberstein, "*Fourier-modal methods applied to waveguide computational problems*," Opt. Lett., **25**, 1092–1094, (2000).

[18] E. Silberstein, P. Lalanne, J.-P. Hugonin, and Q. Cao, "*Use of grating theories in integrated optics*," J. Opt. Soc. Am. A, **18**, 2865–2875 (2001).

[19] L. Li, "*Fourier modal method for crossed anisotropic gratings with arbitrary permittivity and permeability tensors*," J. Opt. A, **5**, 345–355 (2003).

[20] T. Weiss, N. A. Gippius, S. G. Tikhodeev, G. Granet, and H. Giessen, "*Efficient calculation of the optical properties of stacked metamaterials with a Fourier modal method*," J. Opt. A, **11** 114019 (2009).

[21] L. A. Weinsteinm, *Open Resonators and Open Waveguides*, Golem Press (1969).

[22] G. Gamow, "*Quantum Theory of the Atomic Nucleus*," Zeit. Phys., **51**, 204 (1928).

[23] A. J. F. Siegert, "*On the derivation of the dispersion formula for nuclear reactions*," Phys. Rev., **56**, 750–752 (1939).

[24] P. Lalanne, W. Yan, K. Vynck, C. Sauvan, and J.-P. Hugonin, "*Light interaction with photonic and plasmonic resonances*," Laser & Phot. Rev., **12**, 1700113 (2018).

[25] A. O. Govorov, Z. Fan, P. Hernandez, J. M. Slocik, and R. R. Naik, "*Theory of circular dichroism of nanomaterials comprising chiral molecules and nanocrystals: Plasmon enhancement, dipole interactions, and dielectric effects*," Nano Lett., **10**, 1374–1382 (2010).

[26] T. Weiss, M. Mesch, M. Schäferling, H. Giessen, W. Langbein, and E. A. Muljarov, "*From Dark to Bright: First-Order Perturbation Theory with Analytical Mode Normalization for Plasmonic Nanoantenna Arrays Applied to Refractive Index Sensing*," Phys. Rev. Lett., **116** 237401 (2016).

[27] T. Weiss, M. Schäferling, and H. Giessen, "*Analytical normalization of resonant states in photonic crystal slabs and periodic arrays of nanoantennas at oblique incidence*," Phys. Rev. B, **96**, 045129 (2017).

[28] F. Vollmer and S. Arnold, "*Whispering-gallery-mode biosensing: label-free detection down to single molecules*," Nat. Meth., **5**, 591 (2008).

[29] F. Vollmer, D. Braun and A. Libchaber, "*Protein detection by optical shift of a resonant microcavity*," Appl. Phys. Lett., **80**, 4057 (2002).

[30] M. Rosenblit, P. Horak, S. Helsby, and R. Folman, "*Single-atom detection using whispering-gallery modes of microdisk resonators*," Phys. Rev. A, **70**, 053808 (2004).

[31] N. C. Frateschi and A. F. J. Levi, "*Resonant modes and laser spectrum of microdisk lasers*," Appl. Phys. Lett., **66**, 2932–2934 (1995).

[32] S. Neale and E. A. Muljarov, "*Resonant-state expansion for planar photonic crystal structures*," Phys. Rev. B, **101** 155128 (2020).

[33] R. Wood, "*On a Remarkable Case of Uneven Distribution of Light in a Diffraction Grating Spectrum*," Phys. Soc. Lon., **18**, 269 (1902).

[34] J. W. S. Rayleigh, "*Note on the remarkable case of diffraction spectra described by prof. wood*," Phil. Mag., **14**, 60 (1907).

[35] J. von Neumann and E. Wigner, "*Uber merkwürdige diskrete Eigenwerte. Uber das Verhalten von Eigenwerten bei adiabatischen Prozessen*," Phys. Zeit., **30**, 467 (1929).

[36] Y. Plotnik, O. Peleg, F. Dreisow, M. Heinrich, S. Nolte, A. Szameit, and M. Segev, "*Experimental Observation of Optical Bound States in the Continuum*," Phys. Rev. Lett., **107**, 28 (2011).

[37] A. Kodigala, T. Lepetit, Q. Gu, B. Bahari, Y. Fainman, and B. Kanté, "*Lasing action from photonic bound states in continuum*," Nature, **541**, 196 (2017).

[38] B. Zhen, S. L. Chua, J. Lee, A. W. Rodriguez, X. Liang, S. G. Johnson, J. D. Joannopoulos, M. Soljačić, and O. Shapira, "*Enabling enhanced emission and low-threshold lasing of organic molecules using special Fano resonances of macroscopic photonic crystals*," PNAS, **110**, 13711 (2013).

[39] A. A. Yanik, A. E. Cetin, M. Huang, A. Artar, S. H. Mousavi, A. Khanikaev, J. H. Connor, G. Shvets, and H. Altug, "*Seeing protein monolayers with naked eye through plasmonic Fano resonances*," PNAS, **108**, 11784 (2011).

[40] J. M. Foley, S. M. Young, and J. D. Phillips, "*Symmetry-protected mode coupling near normal incidence for narrow-band transmission filtering in a dielectric grating*," Phys. Rev. B, **89**, 165111 (2014).

[41] E. N. Bulgakov, D. N. Maksimov, P. N. Semina, and S. A. Skorobogatov, "*Propagating bound states in the continuum in dielectric gratings*," J. Opt. Soc. Am. B, **35**, 1218 (2018).

[42] E. N. Bulgakov and A. F. Sadreev, "*Bound states in the continuum with high orbital angular momentum in a dielectric rod with periodically modulated permittivity*," Phys. Rev. A, **96**, 013841 (2017).

[43] E. N. Bulgakov and A. F. Sadreev, "*Bloch bound states in the radiation continuum in a periodic array of dielectric rods*," Phys. Rev. A **90**, 053801 (2014).

[44] E. N. Bulgakov and A. F. Sadreev, "*Bound states in the continuum in photonic waveguides inspired by defects*," Phys. Rev. B, **78**, 075105 (2008).

[45] D. C. Marinica and A. G. Borisov, "*Bound States in the Continuum in Photonics*," Phys. Rev. Lett., **100**, 183902 (2008).

[46] O. Panella and P. Roy, "*Bound state in continuum-like solutions in one-dimensional heterostructures*," Phys. Lett. A, **376**, 2580 (2012).

[47] Y. Yang, C. Peng, Y. Liang, Z. Li, and S. Noda, "*Analytical Perspective for Bound States in the Continuum in Photonic Crystal Slabs*," Phys. Rev. Lett., **113**, 037401 (2014)

[48] B. Zhen, C. W. Hsu, L. Lu, and A. D. Stone, "*Topological Nature of Optical Bound States in the Continuum*," Phys. Rev. B, **113**, 257401 (2014).

[49] Z. F. Sadrieva, I. S. Sinev, K. L. Koshelev, A. Samusev, I. V. Iorsh, O. Takayama, R. Malureanu, A. A. Bogdanov, and A. V. Lavrinenko, "*Transition from Optical Bound States in the Continuum to Leaky Resonances: Role of Substrate and Roughness*," ACS Photonics, **4**, 723 (2017).

[50] D. A. Bykov, E. A. Bezus, and L. L. Doskolovich, "*Coupled-wave formalism for bound states in the continuum in guided-mode resonant gratings*," Phys. Rev. A, **99**, 063805 (2019).

[51] C. Sauvan, J. P. Hugonin, I. S. Maksymov, and P. Lalanne, "*Theory of the spontaneous optical emission of nanosize photonic and plasmon resonators*," Phys. Rev. Lett., **110**, 237401 (2013).

[52] D. Floess, M. Hentschel, T. Weiss, H.-U. Habermeier, J. Jiao, S. G. Tikhodeev, and H. Giessen, "*Plasmonic analog of electromagnetically induced absorption leads to giant thin film faraday rotation of 14°*," Phys. Rev. X, **7**, 021048 (2017).

[53] K. Yee "*Numerical solution of initial boundary value problems involving maxwell's equations in isotropic media*," IEEE, **14**, 302–307 (1966).

[54] L. C. Andreani "*Photonic bands and radiation losses in photonic crystal waveguides*," Physica Status Solidi B, **234**, 139–146 (2002)

[55] E. A. Muljarov and T. Weiss, "*Resonant-state expansion for open optical systems: generalization to magnetic, chiral, and bi-anisotropic materials*," Opt. Lett., **43**, 1978 (2018).

[56] E. A. Muljarov and W. Langbein "*Resonant-state expansion of dispersive open optical systems: Creating gold from sand*", Phys. Rev. B, **93**, 075417 (2016)

[57] G. B. Arfken and H. J. Weber, *Mathematical methods for physics, 6th Edition* Academic Press (2005).

[58] M. R. Spiegel, S. Lipschutz, J. J. Schiller, and D. Spellman, *Complex variables with an introduction to conformal mapping and its applications, 2nd edition*, McGraw Hill (2009).

[59] T. Weiss, M. Schäferling, H. Giessen, N. A. Gippius, S. G. Tikhodeev, W. Langbein, and E. A. Muljarov, "*Analytical normalization of resonant states in photonic crystal slabs and periodic arrays of nanoantennas at oblique incidence*," Phys. Rev. B, **96**, 045129 (2017).

[60] T. Weiss, M. Mesch, M. Schäferling, H. Giessen, W. Langbein, and E. A. Muljarov, "*From dark to bright: First-order perturbation theory with an-*

alytical mode normalization for plasmonic nanoantenna arrays applied to refractive index sensing," Phys. Rev. Lett., **116**, 237401 (2016).

[61] D. A. Bykov and L. L. Doskolovich, "*Numerical methods for calculating poles of the scattering matrix with applications in grating theory*," J. Light. Tech., **31**, 793 (2013).

[62] A. Taghizadeh and I.-S. Chung, "*Quasi bound states in the continuum with few unit cells of photonic crystal slab*," Appl. Phys. Lett., **111**, 03114 (2017).

[63] E. N. Bulgakov and A. F. Sadreev, "*Bound states in the continuum with high orbital angular momentum in a dielectric rod with periodically modulated permittivity*," Phys. Rev. A, **96**, 013841 (2017).

[64] C. W. Hsu, B. Zhen, A. D. Stone, J. D. Joannopoulos, and M. Soljac, "*Bound states in the continuum*," Nat. Rev. Mat., **1** 16048 (2016).

[65] D. A. Bykov, E. A. Bezus, and L. L. Doskolovich, "*Coupled-wave formalism for bound states in the continuum in guided-mode resonant gratings*," Phys. Rev. A, **99**, 063805 (2019).

[66] M. Inoue, K. Ohtaka, and S. Yanagawa, "*Light scattering from macroscopic spherical bodies. II. Reflectivity of light and electromagnetic localized state in a periodic monolayer of dielectric spheres*," Phys. Rev. B, **25**, 689 (1982).

[67] P. Paddon and J. F. Young, "*Two-dimensional vector-coupled-mode theory for textured planar waveguides*," Phys. Rev. B, **61**, 2090 (2000).

[68] V. Pacradouni, W. Mandeville, A. Cowan, P. Paddon, J. F. Young, and S. Johnson, "*Photonic band structure of dielectric membranes periodically textured in two dimensions*," Phys. Rev. B, **62**, 4204 (2000).

[69] E. N. Bulgakov and A. F. Sadreev, "*Bound states in the continuum in photonic waveguides inspired by defects*," Phys. Rev. B, **78**, 075105 (2008).

[70] C. W. Hsu, B. Zhen, J. Lee, S. L. Chua, S. G. Johnson, J. D. Joannopoulos, and M. Soljačić, "*Observation of trapped light within the radiation continuum*," Nature, **499**, 188 (2013).

[71] R. F. Ndangali and S. V. Shabanov, "*Electromagnetic bound states in the radiation continuum for periodic double arrays of subwavelength dielectric cylinders*," J. Math. Phys., **51**, 102901 (2010).

[72] L. Li and H. Yin, "*Bound states in the continuum in double layer structures*," Sci. Rep., **6**, 26988 (2016).

[73] E. N. Bulgakov and D. N. Maksimov, "*Topological bound states in the continuum in arrays of dielectric spheres*," Phys. Rev. Lett., **118**, 267401 (2017).

[74] E. N. Bulgakov and D. N. Maksimov, "*Bound states in the continuum and polarization singularities in periodic arrays of dielectric rods*," Phys. Rev. A, **96**, 063833 (2017).

[75] S. I. Azzam, V. M. Shalaev, A. Boltasseva, and A. V. Kildishev, "*Formation of bound states in the continuum in hybrid plasmonic-photonic systems*," Phys. Rev. Lett., **121**, 253901 (2018).

[76] C. Blanchard, P. Viktorovitch, and X. Letartre, "*Perturbation approach for the control of the quality factor in photonic crystal membranes: Application to selective absorbers*," Phys. Rev. A, **90**, 033824 (2014).

[77] J. W. Yoon, S. H. Song, and R. Magnusson, "*Critical field enhancement of asymptotic optical bound states in the continuum*," Sci. Rep., **5**, 18301 (2015).

[78] C. Blanchard, J.-P. Hugonin, and C. Sauvan, "*Fano resonances in photonic crystal slabs near optical bound states in the continuum*," Phys. Rev. B, **94**, 155303 (2016).

[79] L. Ni, Z. Wang, C. Peng, and Z. Li, "*Tunable optical bound states in the continuum beyond in-plane symmetry protection*," Phys. Rev. B, **94**, 245148 (2016).

[80] L. Yuan and Y. Y. Lu, "*Bound states in the continuum on periodic structures: perturbation theory and robustness*," Opt. Lett., **42**, 4490 (2017).

[81] E. N. Bulgakov and D. N. Maksimov, "*Avoided crossings and bound states in the continuum in low-contrast dielectric gratings*," Phys. Rev. A, **98**, 053840 (2018).

[82] A. I. Ovcharenko, C. Blanchard, J.-P. Hugonin, and C. Sauvan, "*Bound states in the continuum in symmetric and asymmetric photonic crystal slabs*," Phys. Rev. B, **101**, 155303 (2020).

[83] X. Gao, C. W. Hsu, B. Zhen, X. Lin, J. D. Joannopoulos, M. Soljaĉić, and H. Chen, "*Formation mechanism of guided resonances and bound states in the continuum in photonic crystal slabs*," Sci. Rep., **6**, 31908 (2016).

[84] A. F. Sadreev "*Interference traps waves in open system: Bound states in the continuum*", arXiv:2011.01221 (2020)

[85] A. S. Pilipchuk and A. F. Sadreev, "*Accidental bound states in the continuum in an open Sinai billiard*," Phys. Lett. A, **381**, 720 (2017).

[86] E. A. Muljarov and W. Langbein, "*Exact mode volume and Purcell factor of open optical systems*," Phys. Rev. B, **94**, 235438 (2016).

[87] D. A. Bykov and L. L. Doskolovich, "*Numerical methods for calculating poles of the scattering matrix with applications in grating theory*", J. of Light. Tech., **31**, 793 (2012).

[88] N. A. Gippius and S. G. Tikhodeev "*Application of the scattering matrix method for calculating the optical properties of metamaterials*", Physics-Uspekhi, **52**, 967 (2009).